DTIC FILE COPY

AD-A202 449

AFOSR-TR- 88-1217

TURBULENCE MODULATION AND DENSE-SPRAY STRUCTURE

by

R. N. Parthasarathy, G. A. Ruff and G. M. Faeth
Gas Dynamics Laboratories
Department of Aerospace Engineering
The University of Michigan
Ann Arbor, Michigan 48109-2140

AIR FORCE OFFICE OF SCIENTIFIC RESEARCH (AFSC)
NOTICE OF TRANSMITTAL TO DTIC
This technical report has been reviewed and is approved for public release IAW AFR 190-12.
Distribution Division

Annual Report
15 July 1987 - 14 July 1988

Approved for public release;
distribution unlimited.

Grant No. AFOSR-85-0244
Air Force office of Scientific Research
Bolling AFB, DC 20332-6448
J. M. Tishkoff, Technical Manager

The views and conclusions contained in this document are those of the authors and should not be interpreted as representing the official policies, or endorsements, either expressed or implied, of the Air Force Office of Scientific Research or the U.S. Government.

DTIC
ELECTE
DEC 0 8 1988
S D
E

August 1988

88 12

Unclassified
SECURITY CLASSIFICATION OF THIS PAGE

UNCLASSIFIED

REPORT DOCUMENTATION PAGE

Form Approved OMB No. 0704-0188

1a. REPORT SECURITY CLASSIFICATION: Unclassified	1b. RESTRICTIVE MARKINGS
2a. SECURITY CLASSIFICATION AUTHORITY	3. DISTRIBUTION/AVAILABILITY OF REPORT: Approved for public release; distribution is unlimited.
2b. DECLASSIFICATION/DOWNGRADING SCHEDULE	
4. PERFORMING ORGANIZATION REPORT NUMBER(S)	5. MONITORING ORGANIZATION REPORT NUMBER(S): AFOSR-TR- 88-1217
6a. NAME OF PERFORMING ORGANIZATION: Dept. of Aerospace Engineering, The University of Michigan; 6b. OFFICE SYMBOL (If applicable)	7a. NAME OF MONITORING ORGANIZATION: AFOSR/NA
6c. ADDRESS (City, State, and ZIP Code): 217 Aerospace Engineering Building, Ann Arbor, MI 48109-2140	7b. ADDRESS (City, State, and ZIP Code): Building 410, Bolling AFB DC 20332-6448
8a. NAME OF FUNDING/SPONSORING ORGANIZATION: AFOSR/NA; 8b. OFFICE SYMBOL (If applicable): NA	9. PROCUREMENT INSTRUMENT IDENTIFICATION NUMBER: AFOSR-85-0244
8c. ADDRESS (City, State, and ZIP Code): Building 410, Bolling AFB DC 20332-6448	10. SOURCE OF FUNDING NUMBERS: PROGRAM ELEMENT NO. 61102F; PROJECT NO. 2308; TASK NO A2; WORK UNIT ACCESSION NO.

11. TITLE (Include Security Classification)

(U) Turbulence Modulation and Dense-Spray Structure

12. PERSONAL AUTHOR(S)

R.N. Parthasarathy, G.A. Ruff and G.M. Faeth

13a. TYPE OF REPORT	13b. TIME COVERED	14. DATE OF REPORT (Year, Month, Day)	15. PAGE COUNT
Annual	FROM 7/15/87 TO 7/15/88	15 August 1988	

16. SUPPLEMENTARY NOTATION

17. COSATI CODES			18. SUBJECT TERMS (Continue on reverse if necessary and identify by block number)
FIELD	GROUP	SUB-GROUP	Multiphase flow, Sprays, Particle-laden flow

19. ABSTRACT (Continue on reverse if necessary and identify by block number)

A theoretical and experimental study of phenomena related to dense sprays is described. Two aspects of dense sprays are being considered: effects of turbulence modulation, which is the direct effect of particle (drop) motion on the turbulence properties of multiphase flows; and the structure and mixing properties of the dense-spray region of pressure atomized sprays.

Turbulence modulation is being studied by considering spherical monodisperse glass particles falling in a stagnant water bath, where effects of turbulence modulation are responsible for the entire turbulence field. Measurements involve phase velocities and temporal and spatial correlations and spectra of the continuous phase velocities using a two-point phase-discriminating laser Doppler anemometer. Flow properties are being analyzed using stochastic methods, assuming linear superposition of randomly arriving particle wakes (Poisson statistics) for liquid phase properties; and random-walk calculations based on statistical time-series methods for particle properties. Measurements show that particles increasingly exhibit turbulent dispersion in their self-generated turbulence field as particle number fluxes are increased.

20. DISTRIBUTION/AVAILABILITY OF ABSTRACT	21. ABSTRACT SECURITY CLASSIFICATION
☒ UNCLASSIFIED/UNLIMITED ☐ SAME AS RPT ☐ DTIC USERS	Unclassified
22a. NAME OF RESPONSIBLE INDIVIDUAL: Julian M Tishkoff	22b. TELEPHONE (Include Area Code): (202) 767-[redacted]0463; 22c. OFFICE SYMBOL: AFOSR/NA

DD Form 1473, JUN 86 — Previous editions are obsolete. — SECURITY CLASSIFICATION OF THIS PAGE

Unclassified

Since random arrival of particle wakes controls the turbulence field, both mean and fluctuating wake velocities contribute to the field yielding a large range of length and time scales even though particle Reynolds numbers are low (less than 1,000). Initial comparisons between predicted and measured continuous phase properties are promising and work is in progress to extend both measurements and analysis.

The dense region of pressure atomized sprays is being studied using large scale (9.5 and 19 mm jet exit diameters) water sprays in still air. Measurements include flow visualization, using flash photography; liquid volume fractions, using gamma-ray absorption; liquid-phase properties, using double-flash holography; and mean and fluctuating gas phase velocities, using phase-discriminating laser Doppler anemometry. Predictions based on the locally homogeneous flow approximation of multiphase flow theory are being evaluated using the measurements. Measurements show the presence of a contiguous liquid core surrounded by a drop-containing mixing layer in the dense-spray region. The inner portion of the mixing layer contains drops and large irregularly shaped liquid elements with the proportion of drops increasing and drop sizes decreasing at larger radial distances. Large liquid elements and the contiguous liquid core cause mean liquid volume fractions to be high near the axis, however, the gas-containing region is relatively dilute at each instant. Throughout the mixing layer, there are large differences in drop velocities providing strong evidence of significant separated flow ffects. Nevertheless, use of the locally homogeneous flow approximation (which implies negligible velocity differences between the phases) yields reasonably good predictions of mean liquid volume fraction distributions when mean liquid volume fractions are greater than 0.2 - largely because the gas and small drops contribute little to the dynamics of the flow due to their small mass fractions. As the spray becomes dilute, however, use of the locally homogeneous flow approximation becomes progressively less satisfactory, consistent with earlier work in this laboratory. Current work seeks to document the properties of the dense spray region more thoroughly and is considering effects of increased gas densities.

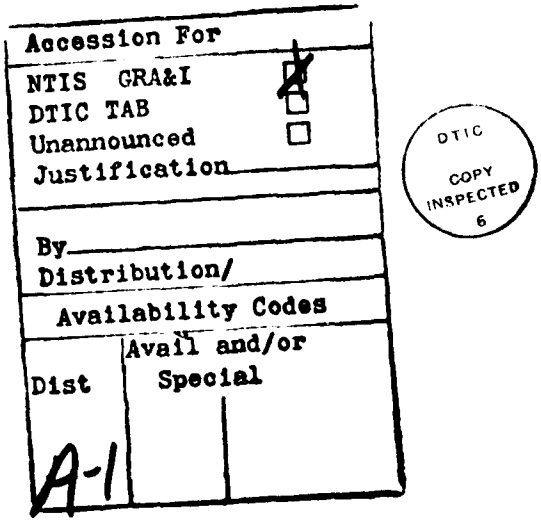

Table of Contents

	Page
Abstract	iii
List of Tables	v
List of Figures	vi
Nomenclature	viii
Acknowledgements	xi
1. Introduction	1
2. Turbulence Modulation	1
2.1 Introduction	1
2.2 Experimental Methods	4
2.2.1 Apparatus	4
2.2.2 Instrumentation	6
2.2.3 Test Conditions	11
2.3 Theoretical Methods	15
2.3.1 Continuous Phase	15
2.3.2 Particle Dynamics	19
2.4 Results and Dicsussion	22
2.4.1 General Observations	22
2.4.2 Phase Velocities	28
2.4.3 Correlations	35
2.5 Summary	44
3. Dense-Spray Structure	45
3.1 Introduction	45
3.2 Experimental Methods	53
3.2.1 Apparatus	53
3.2.2 Instrumentation	56
3.2.3 Test Conditions	60
3.3 Theoretical Methods	60
3.4 Results and Discussion	62
3.4.1 Flow Observations	62
3.4.2 Flow Structure	69
3.5 Summary	74
4. Summary of Investigation	75
4.1 Articles and Papers	75
4.2 Participants	76
4.3 Oral Presentations	76
References	77

List of Tables

Table	Title	Page
1	Summary of Homogeneous Particle Flow Test Conditions.....	12
2	Summary of Evaluation of the Homogeneous Particle Flow Apparatus.....	26
3	Round Liquid Jet Breakup Regimes	46
4	Summary of Liquid Jet Test Conditions at Atmospheric Presure.....	61

List of Figures

Figure	Caption	Page
1	Turbulence modulation in a particle-laden jet	2
2	Sketch of homogeneous particle flow apparatus	5
3	Sketch of two-point phase-discriminating LDA	7
4	Sketch of LDA measuring volume	8
5	Sketch of Mie scattering system	10
6	Particle size distribution (d_p = 0.5 mm)	13
7	Particle size distribution (d_p = 1.0 mm)	14
8	Particle number flux distributions (d_p = 1.0 mm)	23
9	Streamwise velocity fluctuation distributions (d_p = 1.0 mm)	25
10	Typical particle tracks (d_p = 1.0 mm)	27
11	Mean and fluctuating phase velocities (d_p = 0.5 and 1.0 mm)	29
12	Probability density functions of streamwise velocity fluctuations (d_p = 1.0 mm)	31
13	Probability density functions of crosstream velocity fluctuations (d_p = 1.0 mm)	32
14	Probability density functions of streamwise velocity fluctuations (d_p = 0.5 mm)	33
15	Probability density functions of crosstream velocity fluctuations (d_p = 0.5 mm)	34
16	Temporal correlations of streamwise velocity fluctuations (d_p = 0.5 and 1.0 mm)	36
17	Temporal correlations of crosstream velocity fluctuations (d_p = 0.5 and 1.0 mm)	38
18	Power spectral densities of streamwise velocity fluctuations (d_p = 0.5 and 1.0 mm)	40
19	Power spectral densities of crosstream velocity fluctuations (d_p = 0.5 and 1.0 mm)	41
20	Spatial correlations of streamwise velocity fluctuations in the streamwise direction. (d_p = 0.5 and 1.0 mm)	42

21	Spatial correlations of streamwise velocity fluctuations in the lateral direction. (d_p = 0.5 and 1.0 mm).	43
22	Sketch of the near-injector region of pressure atomized sprays.	47
23	Time-averaged liquid volume fractions along axis for fully-developed and slug flow.	49
24	Time-averaged liquid volume fractions for atomization breakup and fully-developed flow.	51
25	Entrainment rates along axis for fully-developed and slug flow.	52
26	Sketch of the atmospheric-pressure test apparatus.	54
27	Sketch of the pressurized test apparatus.	55
28	Sketch of the double-pulse holocamera system.	58
29	Sketch of the hologram reconstruction system.	59
30	Typical hologram reconstruction in the dense-spray region (x/d = 12.5, r/x = 0.075).	63
31	Typical hologram reconstruction in the dense-spray region (x/d = 12.5, r/x = 0.10).	64
32	Typical hologram reconstruction in the dense-spray region (x/d = 12.5, r/x = 0.15).	65
33	Typical hologram reconstructions in the dense-spray region (x/d = 25, r/x = 0.05).	66
34	Typical hologram reconstructions in the dense-spray region (x/d = 25, r/x = 0.10).	67
35	Typical hologram reconstructions in the dense-spray region (x/d = 25, r/x = 0.15).	68
36	Radial variation of ellipticity ratio (x/d = 25).	71
37	Radial variation of Sauter mean diameter (x/d = 25).	72
38	Radial variation of mean streamwise drop velocities (x/d = 25).	73

Nomenclature

Symbol	Description
a	acceleration of gravity
a_k	random shock in stochastic simulation
C_D	particle drag coefficient
d	injector diameter
d_p	particle diameter
$F(r,\phi,t)$	individual particle wake effect function
i	square root of -1
$I(t)$	total wake effect
k	turbulence kinetic energy
ℓ	characteristic wake diameter
ℓ_k	Kolmogorov length scale
ℓ_p	*mean particle spacing*
M_A	acceleration modulus
$\dot{n}''$	particle number flux
Oh	Ohnesorge number
r	radial distance
Re	Reynolds number
Re_ℓ	local wake Reynolds number
$R_i(t)$	Lagrangian velocity correlation
$R_{ij}(r)$	spatial correlation tensor
$R_{ij}(\tau)$	temporal correlation tensor
SMD	Sauter mean diameter
t	time
t_k	Kolmogorov time scale

u,v,w	streamwise, radial and tangential velocities
u_i	velocity component
u_k	Kolmogorov velocity scale
u_{ri}	relative velocity component
We	Weber number
x	streamwise distance
x_i	component of distance
α	volume fraction
δ_{ij}	Dirac delta function
Δ_A	correction of virtual mass force
Δ_H	correction of Basset history force
ε	rate of dissipation of turbulence kinetic energy
θ	momentum diameter of wake
κ	wave number
μ	viscosity
ν	kinematic viscosity
ρ	density
σ	standard deviation of particle diameter, surface tension
τ	time delay
ϕ	azimuthal angle
ϕ_i	weighting parameter in stochastic simulation
$\phi_{ij}(\kappa)$	spatial spectrum tensor
$\phi_{ij}(\omega)$	temporal spectrum tensor
ω	angular frequency

Subscripts

a	air property
c	centerline value
f	liquid property
g	gas property
p	particle or drop property
o	initial condition
∞	ambient condition
(_)	vector quantity

Superscripts

(¯) (⁻')	time-averaged mean and root-mean-squared fluctuating quantity
(~) (~'')	Favre-averaged mean and root-mean-squared fluctuating quantity

Acknowledgements

The authors wish to acknowledge helpful discussions with L. P. Bernal, W.J.A. Dahm, D. R. Glass and W. W. Willmarth of the University of Michigan. We also wish to acknowledge the contributions of the staff of the Gas Dynamics Laboratories at the University of Michigan: C. J. Iott, W. C. Eaton, T. L. Griffin and G. L. Gould for assisting apparatus development; and S. C. Bauerle for helping to prepare this report.

This research was sponsored by the Air Force Office of Scientific Research, Air Force Systems Command, under grant No. AFOSR-85-0244. The U.S. Government is authorized to reproduce and distribute copies of this report for Governmental Purposes notwithstanding any copyright notation thereon.

1. INTRODUCTION

The potential value of rational design procedures for liquid-fueled combustors has motivated numerous efforts to develop methods for analyzing spray evaporation and combustion processes. The goal is to reduce the time and cost of cut-and-try combustor development. This investigation seeks to contribute to the development of this methodology, by studying several fundamental phenomena associated with sprays — particularly the dense-spray region near the exit of the fuel injector passage. The research has application to airbreathing propulsion systems, e.g., liquid-fueled primary combustors and afterburners; liquid-fueled rocket engines; fuel-injected internal-combustion engines; diesel engines; furnaces; etc. Finally, the research involves examination of turbulence/dispersed-phase interactions which are present for a wider class of dispersed turbulent flows, including processes relevant to solid rocket motors, particle-laden exhaust plumes, sedimentation, and atmospheric turbulence associated with precipitation.

The investigation is divided into two main tasks concerning the near-injector dense region of sprays: (1) turbulence modulation (the modification of turbulence properties of the continuous phase by direct action of the dispersed phase), which is being studied using particle-laden liquid flows that are related to dense-spray processes but provide a much simpler system for fundamental study; and (2) direct consideration of the structure of the near-injector dense-spray region of pressure-atomized sprays. Progress on both phases of the study during the present report period is considered in the following. Other descriptions of the research can be found in Parthasarathy et al. (1986), Parthasarathy & Faeth (1987, 1987a, 1987b, 1988), Ruff & Faeth (1987) and Ruff et al. (1987, 1988).

The report begins with consideration of the turbulence modulation study, followed by discussion of the dense-spray structure study. The report concludes with a summary of articles, participants and oral presentations associated with the investigation.

2. TURBULENCE MODULATION

2.1 Introduction

The objective of this portion of the investigation is to gain a better understanding of turbulence modulation, i.e., the direct modification of continuous-phase turbulence properties by transport from the dispersed phase. Turbulence modulation is most important in dense sprays, however, the process is difficult to study in these circumstances due to the complexity of the flow and limitations of instrumentation. To circumvent these problems a much simpler flow is being considered; namely, a homogeneous, dilute, monodisperse particle-laden flow. This provides the multiphase counterpart of homogeneous turbulent flows that have proved to be very helpful for gaining a better understanding of single-phase turbulence.

Results illustrating the effect of turbulence modulation, drawn from earlier work during this investigation (Parthasarathy & Faeth, 1987, 1987a,b), appear in Fig. 1. This involves measurements of turbulence kinetic energies in particle-laden water jets in still water for various particle loadings. Near the injector exit, x/d = 16, the relative velocity between the particles and liquid is small in comparison to the bulk flow velocity; therefore, turbulence properties are dominated by conventional processes in the liquid phase and there is little effect of particle loading on the distribution of turbulence kinetic energy. Farther from the jet exit at x/d = 40, however, relative and bulk liquid velocities are comparable and the turbulence kinetic energy increases significantly with particle loading, particularly near

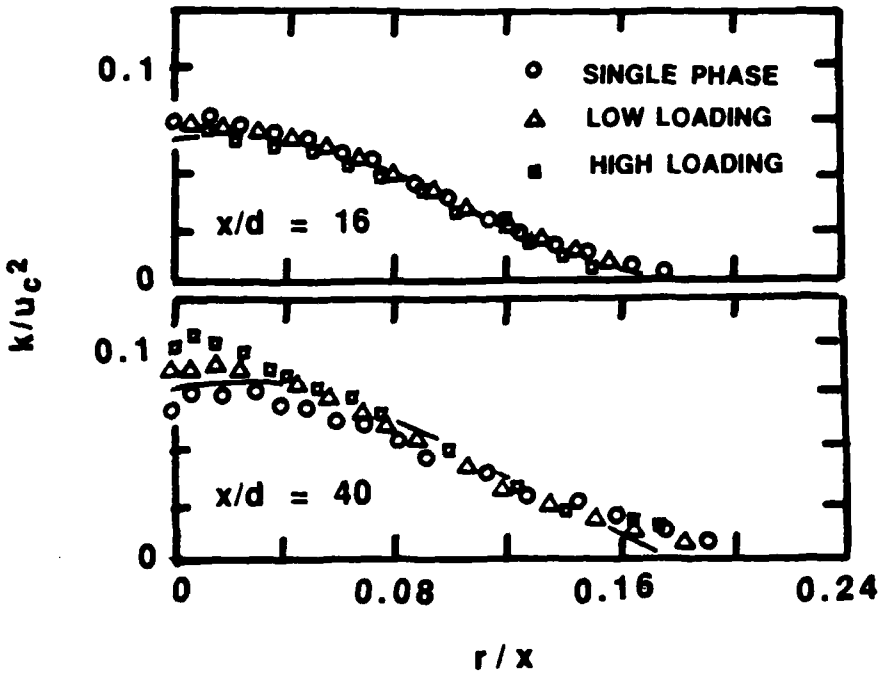

Figure 1 Turbulence modulation in a particle-laden jet.

the axis where conventional production of turbulence becomes small. This is a manifestation of turbulence modulation, involving direct contributions to the turbulent energy budget by the wakes of moving particles. Other observations of this phenomena in multiphase dispersed jets and sprays have been reported by Faeth (1983, 1987), Shuen et al. (1985), Solomon et al. (1985, 1985a), Sun & Faeth (1986, 1986a) and Sun et al. (1986), although none of this work involved direct study of turbulence modulation phenomena.

Early work treating turbulence modulation is reviewed by Batchelor (1972) and Hinze (1972). Batchelor's (1972) study was actually more narrowly focussed, being concerned with sedimentation of a dispersion of spheres with the spheres having sufficiently low Reynolds numbers to be in the Stokes regime. It was shown that the fundamental randomness of particle-laden flows yields properties different from those considering fixed arrays, thus, realistic consideration of turbulence modulation must allow for randomness at the outset. Hinze (1972) reviews early work relating to turbulence modulation in some detail. He also describes several modulation mechanisms: turbulence generation by particles, where the turbulent wakes of particles supplement turbulence generation by conventional single-phase mechanisms like turbulence production by shear forces; turbulence modification, where the instantaneous velocity fields of particle wakes influences local turbulence production; and turbulence dissipation by particles, where acceleration of particles by turbulent fluctuations extracts turbulence energy from the flow. Subsequently, Al Taweel & Landau (1977) considered the turbulence dissipation mechanism for two-phase jets — coining the terminology "turbulence modulation" for processes of this type. Their attempt to describe turbulence dissipation by particles theoretically was not very successful, however, largely due to difficulties with the data base that they used to develop their approach (Faeth, 1977; 1983). Subsequently, there were numerous attempts to treat turbulence dissipation phenomena through models based on higher-order turbulence closures, see Faeth (1987) for a review of this work.

One of the most complete studies of turbulence modulation phenomena has been reported by Lance & Bataille (1982) and Lance et al. (1980, 1985). This involved bubbly air/water flows in a vertical duct downstream of a turbulence generating grid. Similar to the results of Fig. 1, high void fractions and low mean velocities, comparable to the relative velocities of the bubbles, caused substantial increases in turbulence intensities. Other properties of the turbulence were modified as well, e.g., temporal power spectral densities and correlations, skewness and flatness factors of the probability density functions of velocity fluctuations, dissipation rates, and length scales. Some success was also achieved in modifying a second-order closure to treat effects of turbulence modulation on the streamwise variation of the Reynolds stress tensor for a bubbly shear flow (Lance et al., 1985).

In a sense, the present investigation is an extension of the bubbly flow study of Lance and coworkers (1980, 1982, 1985). However, rather than contend with grid-generated turbulence in a flowing continuous phase, the simpler case of a uniform flux of particles moving through a stagnant liquid has been considered. This provides a fully homogeneous flow where all turbulence properties are due to the relative motion of the particles, i.e., the entire flow is a result of turbulence modulation phenomena. The experiment consists of round (nearly monodisperse) glass particles settling in a stagnant water bath. Measurements were made of phase velocities and temporal and spatial correlations of the continuous phase velocities, using a two-point phase-discriminating laser Doppler anemometer (LDA); and of particle fluxes, using Mie scattering. Analysis was also undertaken using stochastic methods to describe processes in both the dispersed and continuous phases.

Progress of this phase of the investigation is discussed in the following. This part of the report begins with a description of experimental and theoretical methods. Initial findings are then discussed. This part of the report then concludes with a summary of the current status of the work.

2.2 Experimental Methods

2.2.1 Apparatus

Figure 2 is a sketch of the homogeneous particle-flow apparatus. The test configuration involves nearly monodisperse round glass particles (nominal diameters of 0.5, 1.0 and 2.0 mm) settling with a uniform flux in a nearly stagnant water bath. Measurements include phase velocities, using a phase-discriminating LDA; and particle number fluxes, using Mie scattering.

The particle flow is initiated by a particle feeder (AccuRate, Model 310, with a 19 mm diameter helix with center rod for 1 and 2 mm particles and with a 25 mm diameter helix with center rod for 0.5 mm particles). The particles are dispersed by falling through an array of 9 screens (stainless steel wire mesh cloth: 0.58 mm diameter wire spaced 2.1 mm apart, 52.4 percent open area for 0.5 and 1.0 mm diameter particles; 0.89 mm diameter wire spaced 4.2 mm apart, 62.4 percent open arrea for 2.0 mm diameter particles), each spaced 190 mm apart. The particles then fall into a windowed tank ($410 \times 535 \times 910$ mm high) which is filled with water to a depth of 800 mm. After a deceleration distance of 100-200 mm, the particles reach a steady (in the mean) terminal velocity. Although the particles enter the bath dry, little difficulty was encountered with particles becoming trapped in bubbles (less than 1 percent). Observations are made near the center of the tank (roughly at a depth of 400 mm). The particles then collect naturally at the bottom of the tank, with little rebound upon impact, and are removed from time-to-time using a suction system.

The test arrangement is conceptually simple, and yields a homogeneous dilute dispersed flow where all turbulence in the system is produced directly by the particles. The particle feed system was evaluated for dry operation, showing essentially uniform particle fluxes across the exit, within experimental uncertainties. Results to be discussed later show that uniform particle fluxes are preserved in the liquid phase; and that flow properties are relatively insensitive to disturbances of the uniformity of particle fluxes and changes in the volume of the windowed tank.

Mean liquid motion in the test tank results from water displaced by particles as they collect at the bottom of the tank: this contribution is very small, ca. 0.01 mm/s. LDA measurements of continuous-phase velocities exhibit somewhat higher mean velocities, ca. 1 mm/s; however, these are still small in comparison to velocity fluctuations, ca. 5 mm/s, and are essentially zero within the uncertainties of velocity measurements. Based on these findings, the test arrangement appears to be satisfactory with flow properties largely resulting from effects of turbulence modulation.

The mean liquid motion that is observed is largely caused by effects of buoyancy forces, due to thermal nonuniformities, rather than nonuniformities in the particle fluxes. Buoyancy intrudes since the liquid bath has an appreciable thermal capacity while the laboratory has relatively poor temperature control. As a result, the bath is invariably either heating up or cooling down. These thermal motions are best seen when there is no particle flow: mean velocity levels at this condition are on the order of 1 to 2 mm/s. However, once the flow of particles is initiated, the thermal motions are nearly destroyed with particle effects dominating the flow in the bath. The effects of buoyant circulation, however,

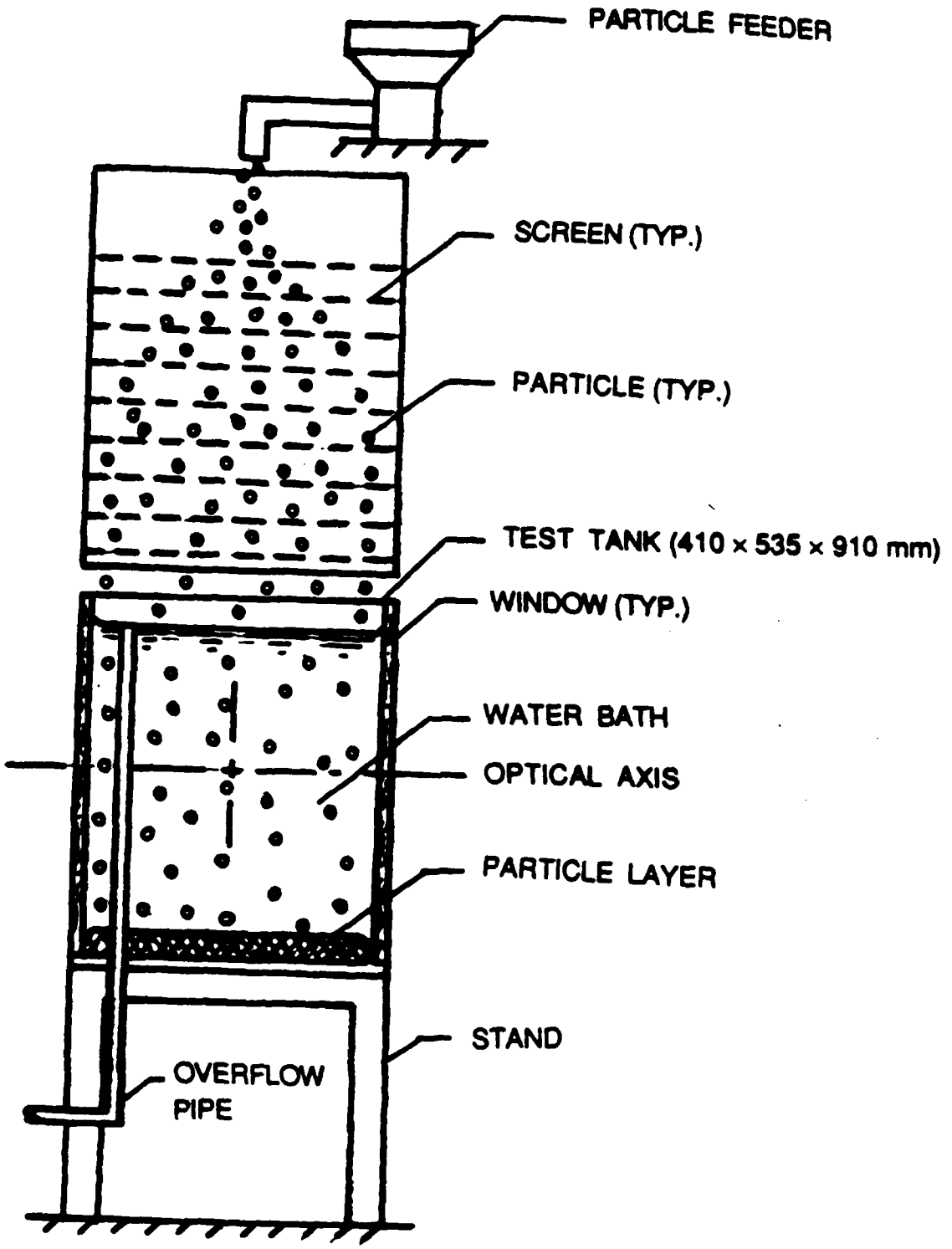

Figure 2. Sketch of homogeneous particle flow apparatus.

prevent useful operation at very low particle loadings. This is not a very significant limitation, since turbulence modulation phenomena are not very strong at these conditions.

2.2.2 Instrumentation

Phase Velocities. Measurements consisted of phase-discriminating LDA for phase velocities and Mie scattering for particle number fluxes. Figure 3 is a sketch of the phase discriminating LDA used to measure liquid velocities. This system is unique, since it exploits the properties of the present homogeneous flow while circumventing difficulties due to the fact that the flow has negligible mean velocities. Desired quantities include liquid velocity fluctuations, and one- and two-point velocity correlations of the continuous phase. Two-point correlations are particularly sought, since turbulence scales produced by the particles are a major issue, and scales cannot be found, even in the streamwise direction, since Taylor's hypothesis is not applicable when there is no mean motion. Streamwise and cross-stream properties are not necessarily the same since the flow is not isotropic; therefore, provision must be made for two-point measurements in both directions — although azimuthal variations in a horizontal plane are irrelevant.

The LDA arrangement to execute these measurements involves one fixed channel and one channel that can be traversed in both the streamwise and cross-stream directions. The two channels are based on the green (514.5 nm) and blue (488 nm) lines of a 2W argon-ion laser (Spectra Physics Model 164-06) operating in the all-lines mode. The green and blue lines of the laser are separated using a dichroic (green) mirror. The blue line, for the traversable channel, is then transmitted to the sending optics using a fiber-optic cable. Both channels are based on a dual-beam forward scatter arrangement. Directional bias and ambiguity were eliminated by use of a 40 MHz Bragg-cell frequency shifter with output signals downshifted to convenient frequency ranges (0.1 - 0.2 MHz) for filtering and signal processing. Titanium dioxide particles in rutile form (nominal size 2.8 μm) were used as LDA seeding particles. One-half gram of the seeding particles was mixed with 500 ml of water and added to the bath. It took about fifteen minutes for the seeding particles to be well distributed throughout the bath and 12 hours for them to settle to the bottom. Since the longest measurement was three hours long, particles settling did not alter data rates significantly.

Light scattered by LDA seeding particles in the water yields lower-amplitude signals than light scattered by the glass beads; therefore, simple amplitude discrimination can help to distinguish between liquid-phase and particle velocity signals. As Modarress et al. (1984) point out, however, particles grazing the LDA measuring volume also yield low-amplitude signals, which can be interpreted as coming from the liquid phase, biasing the liquid velocity measurements. Thus, a phase-driscrimination system was used on both channels to avoid biasing from particles making grazing collisions with the LDA measuring volume. The arrangement is sketched in Fig. 3. The phase discriminator involved a third beam, from a 5 mW HeNe laser (18° from the LDA axis) which was focussed at the LDA measuring volume and observed by off-axis (32°) detection through a laser-line filter. The discriminator optics were adjusted so that all grazing collisions were observed. The region viewed (0.6 mm diameter and 1.2 mm long) by the discriminator surrounds the LDA measuring volume (0.1 mm diameter and 1.3 mm long) as illustrated in Fig. 4. Thus particles that graze the measuring volume yield a scattering signal on the discriminator detector. The discriminator signal was recorded simultaneously with the LDA velocity signal. The data processing system was programmed to eliminate all velocity records where a pulse on the discriminator signal indicated the presence of a particle near the measuring volume.

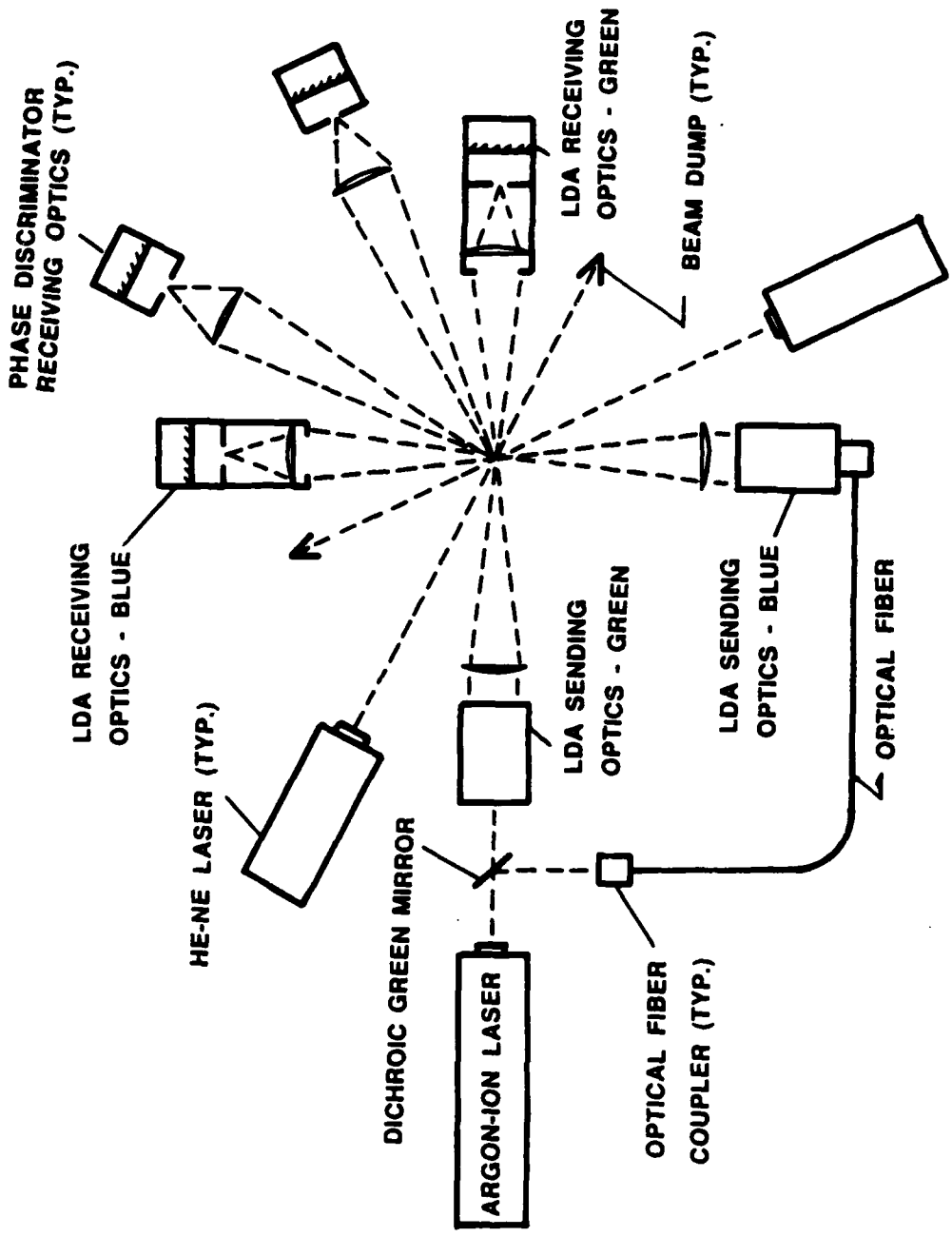

Figure 3 Sketch of two-point phase-discriminating LDA.

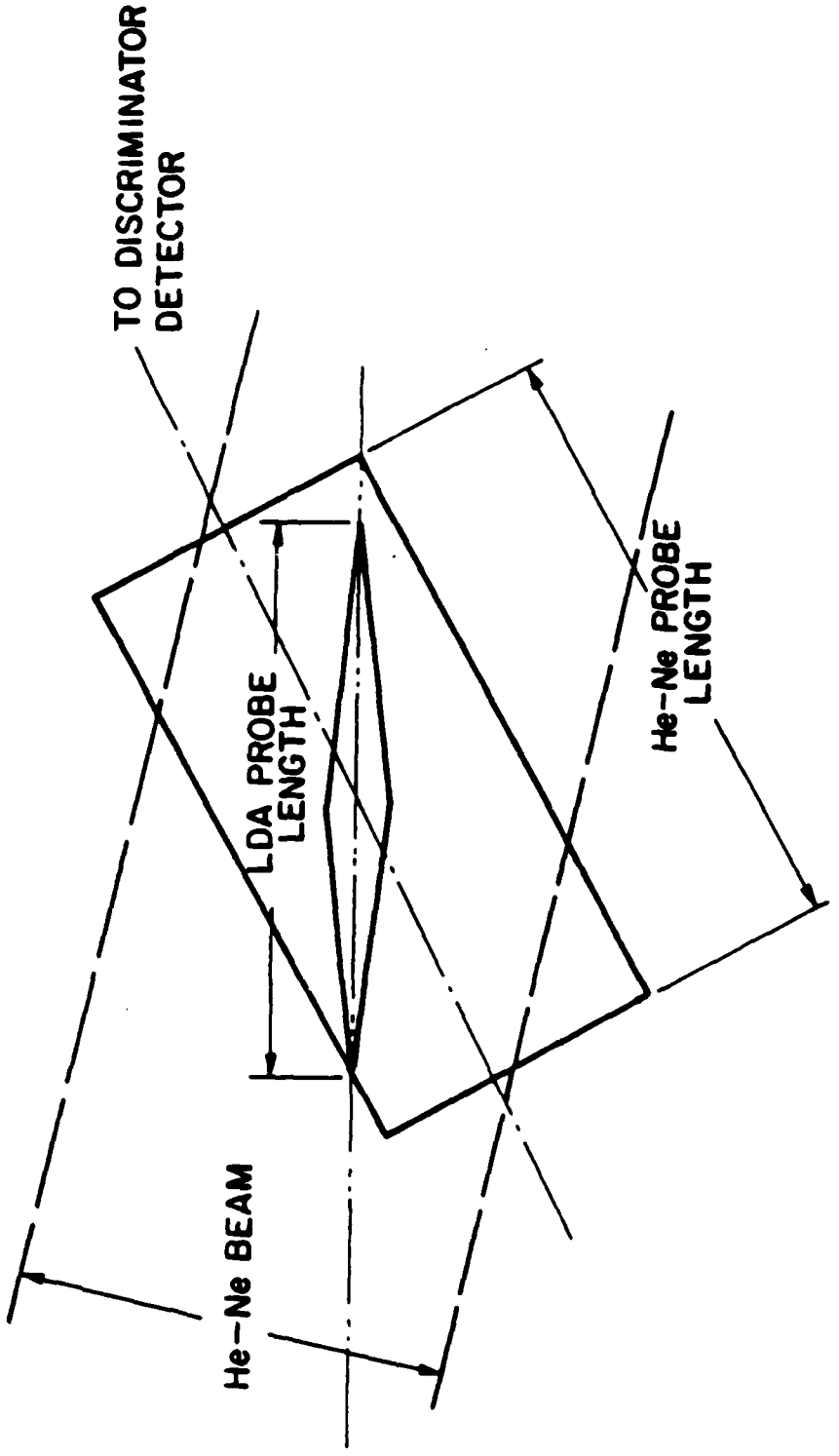

Figure 4 Sketch of LDA measuring volume.

The sending and receiving optics of the traversing channel, including the phase-discriminator for this channel, are all mounted on a single traversing optical breadboard, to maintain alignment. Streamwise and crosstream velocities were measured by rotating the optics appropriately. Velocity signals were found using a burst-counter signal processor (TSI Model 1990C). The output of the burst counter was stored and subsequently processed with a microcomputer (IBM 9002). The time between valid liquid velocity measurements was small in comparison to integral time scales of the flow; therefore, the velocity signal was time-averaged, ignoring periods when particles were present, to obtain unbiased time-averaged mean and fluctuating liquid velocities. The seeding particles provided data rates of 2 - 4 kHz.

Particle velocities were measured using the fixed channel of the phase-discriminating LDA but the arrangement was modified from Fig. 3. In this case a beam spacer was used to elongate the measuring volume and off-axis (45°) forward-scatter light detection was used to reduce signal amplitudes and improve signal-to-noise ratios. The discriminator channel was used to validate signals from the particles as measured by the burst processor. The sending optics included a frequency shifter, as before. The LDA measuring volume for particle velocities was relatively large (basically having dimensions equal to the sum of the diameter actually viewed by the LDA detector and the diameter of a particle, since grazing collisions were recorded), however, this is of little consequence since the flow is homogeneous. As before, the optical plane was rotated to measure streamwise and crosstream velocities.

A detailed analysis of experimental uncertainties for the present LDA measurements has not been completed. However, based on past experience and repeatability from day-to-day we estimate that streamwise and crosstream velocity fluctuations have experimental uncertainties less than 10 percent.

Particle number fluxes. Mie scattering was used to measure particle number fluxes in the streamwise direction. A sketch of this system appears in Fig. 5. A small light sheet, having nearly uniform intensity, was produced at the measuring volume by passing the beam from a 5 mW HeNe laser through an aperture. The measuring volume was observed in the the horizontal plane, normal to the laser beam. Particles passing through the measuring volume generated pulses in the detector output. The pulses were shaped and recorded by a pulse counter which had an adjustable threshold to control spurious background signals. Grazing collisions of particles with the optical measuring volume were recorded; therefore, the radius of the region observed was roughly the sum of the optical radius and the particle radius. The actual area of observation, however, was calibrated by collecting particles. In general, more than 1000 particles were counted in order to find the mean particle number flux.

Experimental uncertainties for the particle number flux measurements were due to variable particle diameters, which influences the area actually observed, and finite sampling times. The latter dominated the measurements, yielding uncertainties (95% confidence) of less than 10 percent.

Particle fluxes were checked for uniformity by placing trays (75 mm × 60 mm) in the bottom of the test tank and weighing the particles (after drying) collected for timed intervals. Experimental uncertainties of these measurements were largely governed by limitations of finite sampling times yielding uncertainties (95 percent confidence) of 10 percent. These measurements confirmed the Mie scattering measurements within the experimental uncertainties of each.

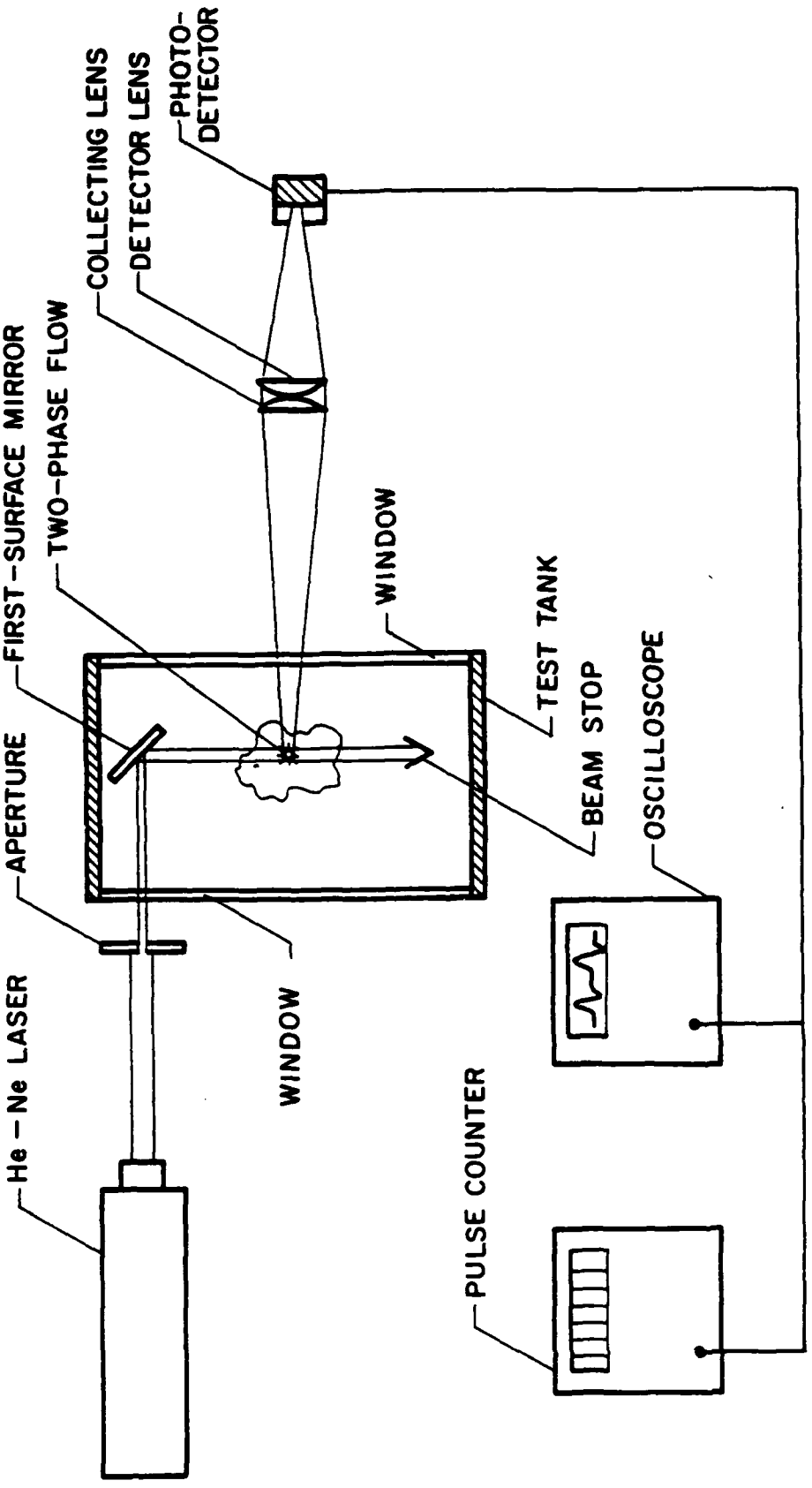

Figure 5 Sketch of Mie scattering system.

2.2.3 Test Conditions

Test conditions are summarized in Table 1. Three particle sizes are being considered having nominal particle diameters of 0.5, 1.0 and 2.0 mm. Particle size distributions for the 0.5 and 1.0 mm particles are illustrated in Figs. 6 and 7. While the particles are not truly monodisperse, they have rather narrow size distributions with standard deviations of the diameter less than 10 percent of the nominal particle diameter. Particle densities are 2450 kg/m^3 which is comparable to the density of water, 1000 kg/m^3. This implies that virtual mass and Bassett history forces are a significant aspect of particle dynamics (Clift et al., 1978). Around 60% of the particles were true spheres. Terminal velocities of the particles, falling alone in still water, are 74, 149 and 266 mm/s. This yields particle Reynolds numbers of 38, 156 and 545 which are higher than the Stokes regime but are well below the transition Reynolds number to supercritical flow, ca. 10^5, where the flow on the upstream side of the sphere becomes turbulent (Clift et al., 1978). As will be discussed subsequently, these Reynolds numbers yield turbulent wakes for the range of wake velocities that can be measured (Tennekes & Lumley, 1972).

Particle fluxes are roughly doubled between operating conditions, with two conditions considered for the 0.5 and 2.0 mm diameter particles and three conditions considered for the 1.0 mm diameter particles. Particle volume fractions can be computed from the following expression:

$$\alpha_p = \pi \dot{n}'' d_p^3 / (6 \bar{u}_p) \qquad (1)$$

noting that $\bar{u}_p$ is very close to the terminal velocity of a freely-falling single particle in an infinite environment for present conditions. Particle volume fractions computed from equation (1) are summarized in Table 1; they indicate that the test flows are very dilute, e.g., particle volume fractions are less than 0.01 percent. Assuming that particles are falling randomly with a uniform mean particle number flux, the mean particle spacing is given by the following expression:

$$\ell_p = (\bar{u}_p / \dot{n}'')^{1/3} \qquad (2)$$

The resulting spacings are in the range 8 - 43 mm or 16 - 33 particle diameters; therefore particle spacings are large in comparison to the size of the LDA measuring volume and effects of direct particle-to-particle interactions are small (see Clift et al., 1978).

Within the region where measurements are made, the mean velocities of particles are constant. If effects of turbulent fluctuations are small, then the rate of dissipation of turbulence kinetic energy is simply equal to the rate of production of turbulence by particles. The rate of production of turbulence is equal to the rate of loss of the potential energy of the particles as they fall in the bath, per unit volume, yielding the following expression for the dissipation rate of turbulence kinetic energy:

$$\varepsilon = \pi \dot{n}'' a \, d_p^3 (\rho_p - \rho) / (6 \rho) \qquad (3)$$

Since dissipation is one of the most difficult properties to measure in a turbulent flow, even a homogeneous flow, it is very helpful that it can be found so easily for the present flows.

Table 1. Summary of Homogeneous Particle Flow Test Conditions[a]

Particle Diameter, d_p(mm)[b]	0.5 (0.045)	1.0 (0.085)	2.0 (TBD)[c]
Particle Properties:			
Terminal Velocity (mm/s)	74	149	266
Reynolds Number (-)	38	156	545
Number Flux (kpart/m^2s)	55.4, 110.8	3.67, 9.16, 20.9	1.13, 3.25
Volume Fraction (m %)	5,10	1.5, 3.7, 8.5	1.8, 5.1
Mean Spacing, ℓ_p(mm),	10.5, 8.2	32.7, 24.1, 18.3	61.8, 43.2
ℓ_p/d_p	21, 16.4	32.7, 24.1, 18.3	30.9, 21.6
Liquid-Phase Properties:			
Rate of Dissipation (mm^2/s^3)	53.2, 106.3	27.3, 68.2, 155.8	67.1, 193.5
Kolmogorov Length Scale (μm)	370, 310	420, 340, 270	350, 260
Kolmogorov Time Scale (ms)	138, 97	178, 113, 75	123, 71
Kolmogorov Velocity Scale (mm/s)	2.68, 3.18	2.37, 2.98, 3.66	2.84, 3.71
Displacement Velocity (μm/s)	4, 7	2, 5, 11	5, 14

[a]Round glass beads with a density of 2450 kg/m^3 falling in a stagnant water bath at 298 ± 2K.
[b]Standard deviations in parenthesis.
[c]TBD denotes to be determined.

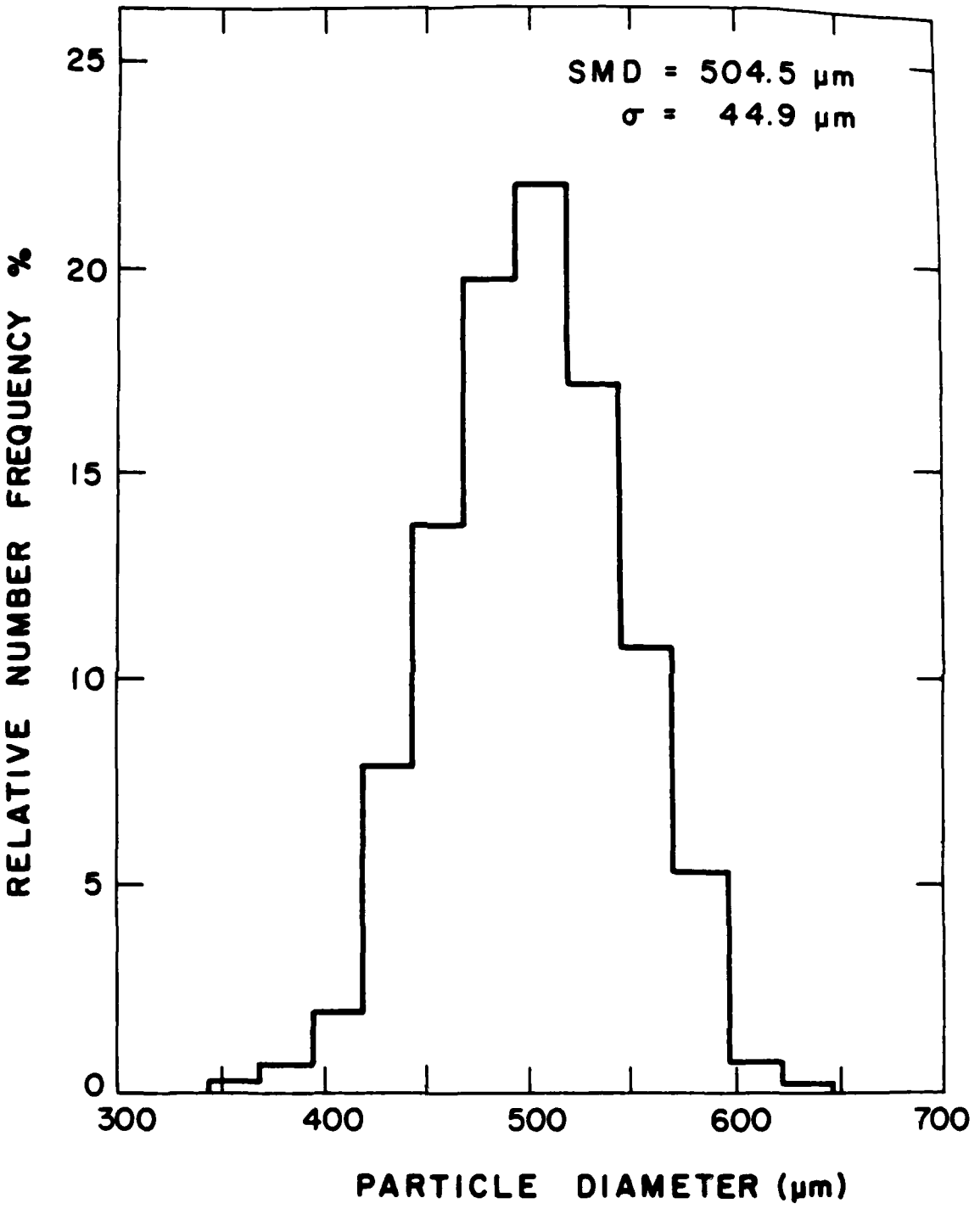

Figure 6 Particle size distribution (d_p = 0.5 mm).

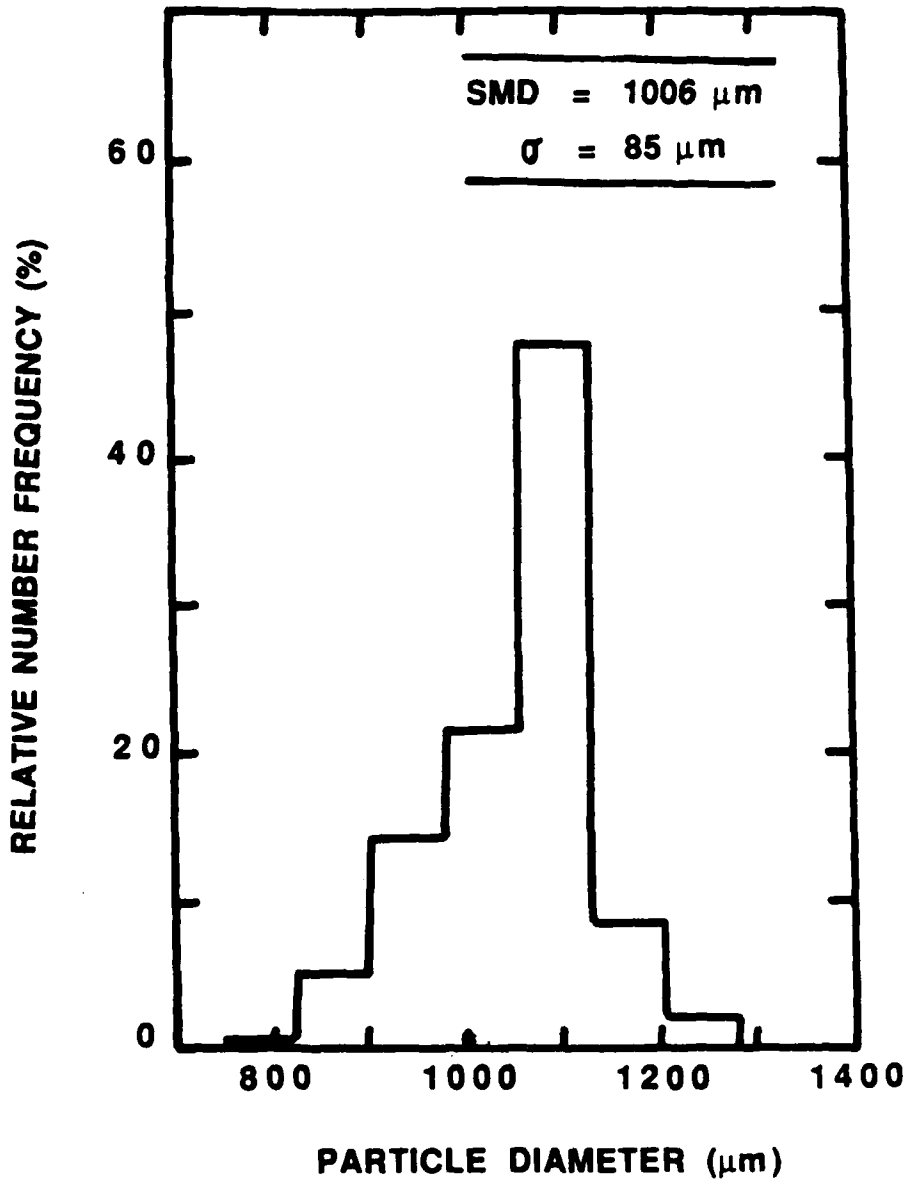

Figure 7 Particle size distribution (d_p = 1.0 mm).

Dissipation will be used to characterize the measurements in the following since it provides a basis to compare different particle sizes and number fluxes with a single measure. Given ε, the Kolmogorov microscales can be computed immediately, as follows:

$$\ell_k = (\nu^3/\varepsilon)^{1/4}, \quad t_k = (\nu/\varepsilon)^{1/2}, \quad u_k = (\varepsilon\nu)^{1/4} \tag{4}$$

The values of ε and the Kolmogorov microscales found from equations (3) and (4) are also summarized in Table 1. Minimum Kolmogorov length scales are on the order of 250 μm, which is somewhat larger than the bulk of the LDA measuring volume (100 μm diameter $\times$ 1.3 mm long). The Kolmogorov time scale is in the range 70 - 200 ms, which is significantly longer than the present velocity sampling rate of ca. 1 ms. Kolmogorov velocity scales are roughly 2 - 4 mm/s while the upflow velocity resulting from the displacement of liquid by particles collecting at the bottom of the tank is generally less than 0.02 mm/s; therefore, bulk liquid velocities in the test tank are negligible in comparison to other velocity scales of the flow.

Although it was not really intended, present test conditions roughly correspond to conditions in rainstorms — except for effects of virtual mass and Basset history forces which are important for glass particles in water but are small for raindrops in air, and somewhat smaller particle spacings. In particular, particle Reynolds numbers at terminal velocity conditions are nearly the same in water and air while present particle diameters correspond to "light rain" (d_p = 0.5 mm, ℓ_p/d_p = 150), "moderate rain" (d_p = 1.0 mm, ℓ_p/d_p = 120), and "excessive rain" (d_p = 2.0 mm, ℓ_p/d_p = 70); see Humphreys (1964). Since little is known about the turbulence properties within rainstorms, this provides a useful byproduct of the present investigation.

2.3 Theoretical Methods

2.3.1 Continuous Phase

General Description. Under fully-stationary conditions the present flows involve an infinitely large range of length and time scales, ranging from the small scales associated with the flow near a particle to the infinitely-large scales eventually associated with particle wakes. Thus, exact numerical simulation of these flows will never be possible and some degree of modeling must be accepted at the outset. The present analysis has sought to do this in a relatively fundamental way rather than adopt an approach involving a higher-order turbulence closure. Batchelor's (1972) study also demonstrates that it is important to treat the essential randomness of flows of this type rather than prescribe some sort of fixed array, i.e., the process is essentially a singular perturbation problem with respect to the presence or absence of randomness. Thus, effects of randomness are considered at the outset.

The flow to be considered is caused by monodisperse spherical particles moving with finite relative velocities with respect to a stagnant liquid which is assumed to be infinite in extent. In the present case, the particle motion is maintained by the force of gravity which causes the particles to settle. However, the analysis is also pertinent to any flow where particles are moving with a relative velocity with respect to the fluid: this may be caused either by their inertia or by some other type of force field. While instantaneous phase velocities vary with time, the flow is assumed to be fully developed so that time-averaged quantities are constant, i.e., the flow is taken to be statistically stationary. The time-averaged particle flux across a plane normal to the streamwise direction is assumed to

be uniform while the physical properties of the fluid are constant, therefore, the flow is homogeneous. Finally, particle arrival times at a point are assumed to be random, i.e., the probability that a particle will arrive at a point within a particular increment of time is independent of earlier or subsequent particle arrivals. In this circumstance, particle arrival times satisfy Poisson statistics (Rice, 1954).

In the following, the properties of the continuous phase are emphasized, imposing the assumption of a dilute particle-laden flow. This may seem restrictive with respect to eventual applications involving dense sprays; however, results to be discussed concerning the structure of dense pressure-atomized sprays suggest that drop-containing regions in these flows are actually quite dilute at each instant even when the time-averaged liquid volume fraction is large. For dilute dispersed flows, the volume fraction of the dispersed phase is small so that the probability of a particular test point being within a particle or the immediate flow field surrounding a particle is quite small as well — we assume that it is negligibly small. Particle wakes, however, ultimately become infinitely large in extent; thus, continuous-phase properties observed in the present flows are largely controlled by the properties of interacting particle wakes — for convenience, we assume that these properties are related to the asymptotic properties of wakes. Finally, at the asymptotic limit, the equations of motion of laminar and turbulent wakes are linear; therefore, we can also assume that the flow properties are the result of a linear superposition of the properties of the wakes of all particles that have passed through a plane normal to the streamwise direction which contains the point of observation. Thus, the main issues of the analysis involve the method of summing and characterizing particle wake properties.

Under present assumptions, the method of summing wake properties inolves a trivial extension of methods used to analyze random noise in cases where effects of noise can be added linearly (Rice, 1954). Take the point of observation to be the origin of a cylindrical coordinate system with x denoting the streamwise direction (positive in the direction of mean particle motion), and r and ϕ denoting radial and azimuthal coordinates in a plane normal to the direction of particle motion. Suppose that the arrival of a particle at x=0, r, ϕ and t = 0 produces an effect $F(r,\phi,t)$ at the point of observation. Then if the effect of each particle can be added linearly, the total effect at time t due to all particles is

$$I(t) = \sum_{j=0}^{\infty} \sum_{k=-\infty}^{\infty} F(r_j,\phi_j, t - t_{jk}) \qquad (5)$$

where the position vectors (r_j,ϕ_j) are chosen to collect all particles, the k^{th} particle at position r_j, ϕ_j arrives at x = 0 at t_{jk}, and the series is assumed to converge.

Under these circumstances, Campbell's theorem (Rice, 1954) can be extended to treat random arrivals of particles over a plane to yield the time-averaged value of I(t) as follows:

$$\overline{I(t)} = \dot{n}'' \int_{-\infty}^{\infty} dt \int_{0}^{2\pi} d\phi \int_{0}^{\infty} F(r,\phi,t) r dr \qquad (6)$$

while the mean-square value of the fluctuation about the average is

$$\overline{I'(t)^2} = \dot{n}'' \int_{-\infty}^{\infty} dt \int_0^{2\pi} d\phi \int_0^{\infty} F^2(r,\phi,t) r \, dr \qquad (7)$$

where $\dot{n}''$ is the average number of particles arriving at $x = 0$ per unit area and time.

Wake Properties. In order to solve equations (6) and (7) for continuous-phase prperties like mean and fluctuating velocities, correlations, etc., the proper effect of an individual particle wake, $F(r,\phi,t)$, must be prescribed. Since we are only interested in kinematic quantities related to velocities, the velocity distribution of the wakes is the main parameter of interest. Work thus far has been limited to streamwise velocities.

Specifying a canonical particle wake is complicated by the fact that the particles undergo turbulent dispersion as they settle, with increasing effects of turbulent dispersion as the particle number flux is increased (Parthasarathy & Faeth, 1987). The random deflection of the particles causes the wakes to be disturbed in both the streamwise and crosstream direction. However, pending analysis of random particle motion as a result of turbulent dispersion and its effect on wake properties, canonical wake properties were obtained at the limit of the particle volume fraction approaching zero. In this case, turbulent dispersion is negligible and the particles follow a straight vertical path, allowing use of existing solutions for wake properties.

The Reynolds numbers of axisymmetric wakes are initially comparable to particle Reynolds numbers but progressively decrease with increasing distance from the particle; in addition, wakes become laminar for wake Reynolds numbers on the order of unity (Tennekes & Lumley, 1972). All particle Reynolds numbers for present tests are greater than unity; therefore, the properties of both laminar and turbulent wakes are needed to specify $F(r,\phi,t)$. For present initial calculations, only the mean velocities of turbulent wakes were considered, ignoring direct effects of wake turbulence on the flow field. This is questionable since velocity fluctuations in asymptotic wakes have the same order of magnitude as the maximum mean velocity defect of the wake, at least when wake Reynolds numbers are high, ca. 10^4 (Tennekes & Lumley, 1972; Uberoi & Freymuth, 1970); therefore, this assumption will be re-examined during subsequent development of the theory.

Expressions for the velocity distribution in a turbulent wake can readily be derived from results given in Tennekes & Lumley (1972), yielding:

$$u/u_p = 2.23(u_p t/\theta)^{-2/3} \exp\{-r^2/(2\ell^2)\} \qquad (8)$$

where

$$\theta = (C_D d_p^2 / 8)^{1/2} \qquad (9)$$

and

$$\ell/\theta = 0.33 (u_p t/\theta)^{1/3} \qquad (10)$$

In equations (8) - (10), θ is the initial momentum diameter of the flow, ℓ is the characteristic diameter at downstream positions, and u_p is the terminal velocity of the

particle. The time, t, is measured from the point where the virtual origin of the asymptotic wake crosses the plane of the observation point. The streamwise displacement of the particle, relative to the virtual origin, is given by

$$x_p = u_p t \tag{11}$$

Finally, the local wake Reynolds number at time t becmes:

$$Re_{\ell} = u_c \ell/\nu = 0.73(u_p t\, \theta/\nu)\, (x/\theta)^{-1/3} \tag{12}$$

The value of u given by equation (8) becomes unbounded at small t since the formula only represents asymptotic wake properties. Thus, as a practical matter, computations were only made for conditions where $u_c \leq u_p$. This involves ignoring the near-wake region which is consistent with the other approximations relating to dilute particle flow.

The equation streamwise for velocities in laminar wakes is as follows (Schlichting, 1979):

$$u/u_p = (u_p\theta/(4\nu))(u_p t/\theta)^{-1} \exp\{-r^2/(4\nu t)\} \tag{13}$$

where the expressions for θ and x_p are the same as before, e.g., equations (9) and (11). Similar to the turbulent wake, equation (13) was only used for times such that $u_c \leq u_p$, ignoring the near-wake region. Equation (13) must be transformed to extend wake properties at the point where the wake becomes laminar, which is straight-forward.

Correlations and Spectra. Computation of mean and fluctuating velocities involves direct application of equations (6) and (7), combining equations (8) and (13) to specify the wake velocity. Spatial and temporal correlations were also computed. Present definitions of these quantities are summarized in the following.

To simplify notation a Cartesian coordinate system will be adopted to define correlations and power spectral densities. The spatial correlation tensor is defined as follows:

$$R_{ij}(\underline{r}) \equiv \overline{u_i(\underline{x},t)u_j(\underline{x} + \underline{r}, t)} \tag{14}$$

where $\underline{x}$ and $\underline{r}$ denote position vectors. Since the present turbulence is homogeneous, the spatial correlation tensor is only a function of $\underline{r}$. The spatial spectrum tensor is the Fourier transform of $R_{ij}(\underline{r})$ (Tennekes & Lumley, 1972).

$$\phi_{ij}(\underline{\kappa}) = \frac{1}{(2\pi)^3} \int \int_{-\infty}^{\infty} \int (\exp(-\, i\, \underline{\kappa}\cdot\underline{r}) R_{ij}(\underline{r}) dr \tag{15}$$

thus

$$R_{ij}(\underline{r}) = \int \int_{-\infty}^{\infty} \int \exp(i\, \underline{\kappa}\cdot\underline{r})\phi_{ij}(\underline{\kappa}) d\underline{\kappa} \tag{16}$$

where $\underline{\kappa}$ is the wave number vector.

The corresponding relationships for temporal correlation and spectrum tensors are as follows (Tennekes & Lumley, 1972):

$$R_{ij}(\tau) = \overline{u_i(\underline{x},t)u_j(\underline{x},t+\tau)} \tag{17}$$

$$\phi_{ij}(\omega) = \frac{1}{2\pi} \int_{-\infty}^{\infty} \exp(-i\omega\tau)\, R_{ij}(\tau)d\tau \tag{18}$$

$$R_{ij}(\tau) = \int_{-\infty}^{\infty} \exp(i\omega\tau)\, \phi_{ij}(\omega)d\omega \tag{19}$$

These quantities were computed by setting $F(r,\phi,t) = u_i(\underline{x},t)u_j(\underline{x}+\underline{r},t)$ or $F(r,\phi,t) = u_i(\underline{x},t)u_j(\underline{x},t+\tau)$ in equation (6). Spatial and temporal correlation tensor coefficients were then found by normalizing with the appropriate root mean squared velocity fluctuations obtained from equation (7). Finally, power spectral densities were found by computing the Fourier transform of the velocity, u(t), using a fast Fourier transform (FFT) subroutine. These steps are a direct extension of Campbell's Theorem for Poisson statistics discussed by Rice (1954).

2.3.2 Particle Dynamics

The properties of the particle phase involve computations of particle motion in the innately random velocity field of the continuous phase and are analogous to random-walk computations. Computations were completed for a sufficient number of particle trajectories, or a sufficiently-long trajectory of a single particle, in order to obtain statistically-significant results.

Consistent with the continuous-phase analysis, particle volume fractions are assumed to be infinitely small; therefore, particle collisions and effects of adjacent particles on particle transport properties are negligible. Particles are also assumed to be small in comparison to the smallest scales of the turbulence field. This is not true since Kolmogorov length scales are on the order of 250 μm while particle diameters are 500 - 2000 μm. Measurements of continuous-phase velocity spectra, however, suggest that the flow does not contain much energy at these small scales although potential for the smallest scales to modify particle drag properties should be re-examined in the future. The particles are assumed to be monodisperse and spherical which are generally conditions of the experiments. Finally, Magnus and Saffman-lift forces and static pressure gradients can be ignored with little error (Faeth, 1977, 1983, 1988).

Under these assumptions, particle motion can be found using the formulation of Odar & Hamilton (1964), reviewed by Clift et al. (1978), as follows:

$$d\,x_{pi} / dt = u_{pi} \tag{20}$$

$$(\rho_p / \rho + \Delta_A / 2) d\,u_{ri} / dt = a(\rho_p / \rho - 1)\delta_{1i} - 3C_D |u_r| u_{ri} / (4d_p)$$

$$- \Delta_H (81\nu / \pi d_p^2)^{1/2} \int_{t_o}^{t} (t - \xi)^{-1/2} (d\,u_{ri} / d\xi) d\xi \tag{21}$$

where a Cartesian reference frame has been used with i=1 denoting the vertical direction. The terms of the left-hand side of equation (21) represent acceleration due to particle and virtual mass, while the terms on the right-hand side represent buoyancy, drag and Basset-history forces.

The parameters Δ_A account for particle acceleration; they were empirically correlated by Odar & Hamilton (1964), as follows:

$$\Delta_A = 2.1 - 0.123\, M_A^2 / (1 + 0.12\, M_A^2) \tag{22}$$

$$\Delta_H = 0.48 + 0.52\, M_A^3 / (1 + M_A)^3 \tag{23}$$

where M_A is the particle acceleration modulus

$$M_A = (d\,u_r / dt) d_p / u_r^2 \tag{24}$$

The values of Δ_A and Δ_H vary in the ranges 1.0-2.1 and 1.00-0.48, the former values being the correct limit for the Basset-Boussinesq-Oseen (B-B-O) formulation of equation (21) (Clift et al. 1978). Particle Reynolds numbers, based on the relative velocity of the particle and fluid, did not reach the supercritical flow regime; therefore, the standard drag coefficient for solid spheres was approximated as follows (Faeth, 1983):

$$C_D = 24(1 + Re^{2/3} / 6) / Re, \qquad Re \le 1000; \qquad C_D = 0.44; \qquad Re > 1000 \tag{25}$$

where Re denotes the particle Reynolds number. For present test conditions, liquid velocity fluctuations are small in comparison to the relative velocity of the particles; therefore, the high relative turbulence intensity drag expressions used by Parthasarathy & Faeth (1987, 1987a, 1987b) are not needed.

Statistical simulation of particle trajectories is based on methods used to find turbulence/radiation interactions developed by Kounalakis et al. (1988, 1988a) using formal statistical time series simulation techniques adapted from Box & Jenkins (1976). The statistical simulation of the velocity field of the continuous phase can be carried out to satisfy any number of the statistical properties of the continuous phase: mean velocities, velocity fluctuations, Lagrangian time correlations, instantaneous conservation of mass, higher-order correlations, etc. To the extent that the analysis of Section 2.3.1 is correct, these properties are theoretically accessible as well. Nevertheless, computational requirements increase as the number of properties of the flow to be simulated increase and priorities must be set. Based on findings using earlier methods of statistical simulation

(Faeth, 1983, 1987), mean and fluctuating velocities and Lagrangian time correlations appear to be sufficient to treat turbulent particle dispersion; therefore, initial simulations are designed to reproduce these properties.

The present flows are homogeneous and mean velocities and cross-correlations like $\overline{u'v'}$ are small; therefore, only velocity fluctuations must be simulated and velocity components may be assumed to be statistically independent. However, velocity fluctuations are not isotropic: streamwise velocity fluctuations are larger than crosstream velocity fluctuations (naturally, both components of the latter are equal). Finally, measurements have shown that the velocity fluctuations have Gaussian probability density functions.

To illustrate the approach, consider a simulation using equal time steps that has proceeded at least $k > p > 0$ time steps. The value of any component of the velocity fluctuation at the end of the next time step, u'_k, is found from the following regression relationship (Box & Jenkins, 1976):

$$u'_k = \phi_1 u'_{k-1} + \phi_2 u'_{k-2} + \ldots + \phi_p u'_{k-p} + a_k \tag{26}$$

where the ϕ_i are weighting parameters of past values of velocity fluctuations and a_k is an appropriate random selection of a velocity fluctuation perturbation. The ϕ_i are selected to satisfy the Lagrangian time correlation for this component of velocity, defining

$$R_i = \overline{u'(t)u'(t-i\Delta t)} \,/\, \overline{u'(t)^2} \tag{27}$$

This requirement yields a system of linear algebraic equations for the ϕ_i, called the Yule-Walker equations, as follows:

$$\begin{aligned}
R_1 &= \phi_1 + \phi_2 R_1 + \ldots + \phi_p R_{p-1} \\
R_2 &= \phi_1 R_1 + \phi_2 + \ldots + \phi_p R_{p-2} \\
&\vdots \\
R_p &= \phi_1 R_{p-1} + \phi_2 R_{p-2} + \ldots + \phi_p
\end{aligned} \tag{28}$$

The requirement that the variance of the velocity fluctuations be satisfied yields the following expression for the required variance of a_k:

$$\overline{a_k^2} = (1 - R_1\phi_1 - R_2\phi_2 - \ldots - R_p\phi_p)\overline{u'^2} \tag{29}$$

where u' and thus, a_k, are assumed to have Gaussian probability density functions (PDF's) as noted earlier.

The analysis begins with a proper random selection of the components of the velocity fluctuations, u'_0, allowing for the variances and anisotropy. Using a first-order

regression (p=1), ϕ_1 and $\overline{a_1^2}$ are found from equations (28) and (29). A random selection for a_1 is then made from its PDF so that u'_1 can be computed from equation (26). The motion of the particle in this velocity field is then computed to find conditions at Δt (adjusting u'_1 to close the process iteratively if R_1 and $\overline{u}_1^2$ change significantly with the final position of the particle, although this is unlikely for typical Δt needed for accurate integration of particle motion). The process is then repeated with k=2,3,...,p, after which only the p previous sets of properties are kept in the solution. This entire process is either completed for n particles, where n is large enough to provide statistically-significant results, or for one particle, with the computation proceeding long enough to provide statistically-significant results, as noted earlier.

The key to simulating particle trajectories is knowledge of the Lagrangian correlations, R_i. Fortunately, although Taylor's hypothesis is not appropriate to relate temporal and spatial variations of turbulence properties at a fixed point since the mean liquid velocity is small, relative velocities of particles are large in comparison to velocity fluctuations; therefore, Taylor's hypothesis can be applied to obtain correlations along a particle path. Thus knowledge of spatial and temporal correlations in the streamwise and crosstream directions allow the R_i to be estimated.

The output of the stochastic simulation consists of particle properties like $\overline{u_p}$, $\overline{v_p}$, $\overline{u'_p}$ and $\overline{v'_p}$ — the latter being direct measures of particle dispersion. The computations also provide information on the sinuousness of the particle wakes which is needed to advance the simulation of continuous-phase properties from the dilute limit where the particle trajectories are vertical. Another potential advance of the analysis involves instantaneously satisfying local conservation of mass. This appears to be possible by extending an approach derived by Kraichnan (1970). In fact, this is a rather interesting line of theoretical investigation since the simulation would then provide p'(t), which could have significant implications for particle trajectories, since there is a pressure interaction term which is usually ignored because local pressure fluctuations are generally unknown.

2.4 Results and Discussion

2.4.1 General Observations

Initial experiments dealt with the operation of the test apparatus. This involved consideration of the degree to which homogeneous flow had been achieved and the dependence of test results on the size of the liquid bath and disturbances to the operation of the system.

Uniformity of particle number fluxes across the bath was a primary consideration. Measurements of particle number fluxes as a function of position for the 1.0 mm diameter particles, at all three loadings used, are illustrated in Fig. 8. These measurements only extend to the near-wall region on one side, due to limitations in traversing the Mie scattering probe volume, however, it is evident that particle number fluxes are uniform (with ± 10 percent) for the middle 300 mm of the bath cross-section. The variation within this central region is within experimental uncertainties. Reduced particle fluxes in the near-wall region are attributed to the fact that the duct for the particle feed system was actually 25

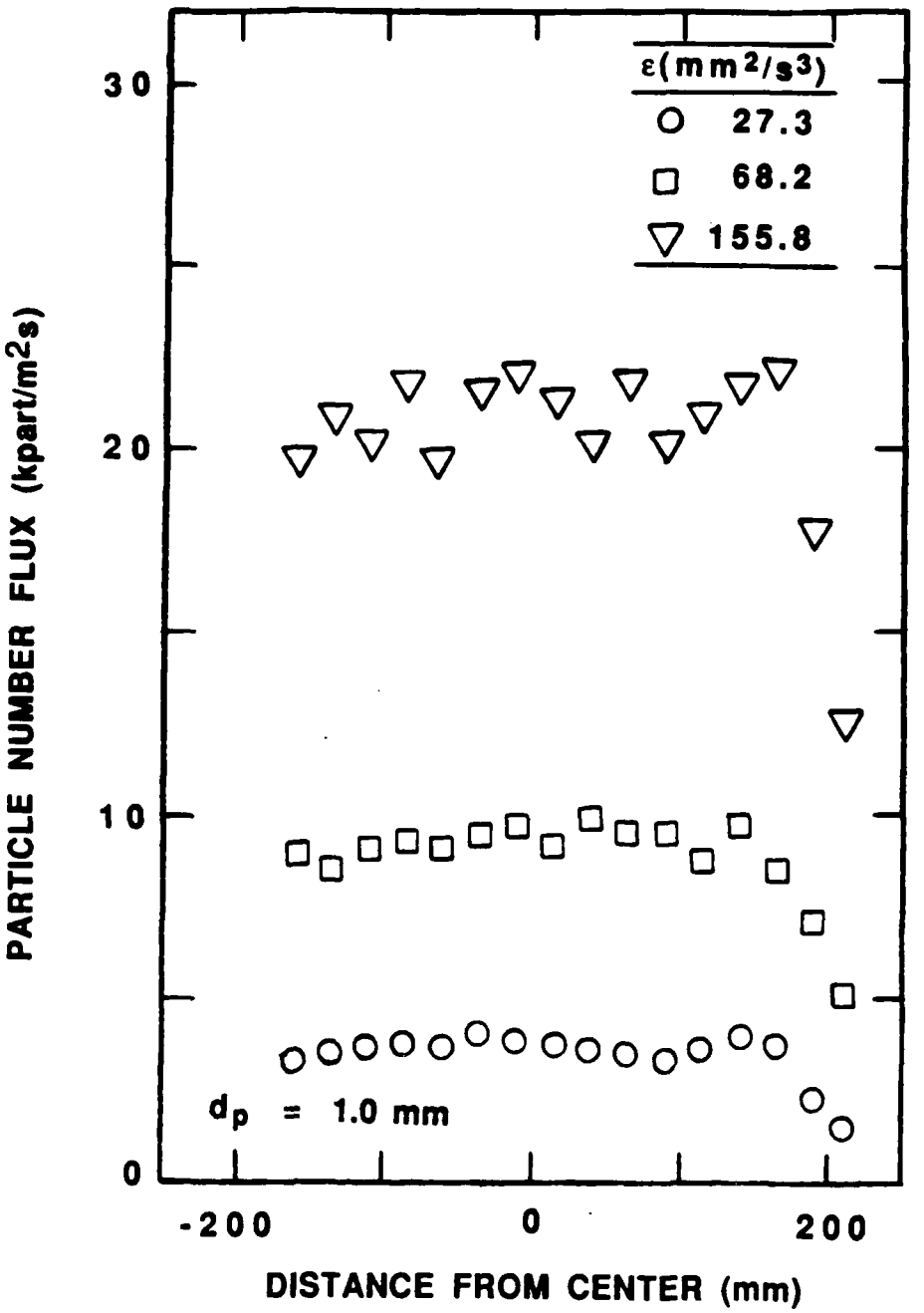

Figure 8 Particle number flux distributions (d_p = 1.0 mm).

mm smaller (in each direction) than the dimensions of the liquid bath. Collection of particles at the bottom of bath revealed that particle fluxes were also uniform, except within 50 mm of the walls, in the other direction as well. The variation of particle feed rate from the screw feeder was within 4 percent. Thus, the particle feed system was judged to be satisfactory for present purposes.

The variation of streamwise velocity fluctuations across the bath, for the operating conditions used with the 1.0 mm diameter particles, is illustrated in Fig. 9. Open and darkened symbols represent results of tests conducted 100 mm above and 100 mm below the optical plane of the fixed LDA channel. Similar to particle number fluxes, streamwise velocity fluctuations are uniform within experimental uncertainties across the central 300 mm cross-section of the liquid bath. Repeatability of these results was satisfactory as well.

A series of tests was also conducted to examine effects of wave action at the surface of the bath, disturbances of the particle flux distribution, and effects of the volume of the test tank. The results are summarized in Table 2. Effects of surface waves were examined by installing a honeycomb at the liquid surface (10 mm cell size, 50 mm thick with the mean liquid level at the midpoint of the honeycomb). The particles passed through the honeycomb with no difficulty. There was virtually no change in the measured values of streamwise velocity fluctuations and temporal spectra of streamwise velocity fluctuations due to the presence of the honeycomb, which was then removed during subsequent tests.

Effects of disturbances of the particle flux distributions were more significant. These disturbances involved placing 50 mm wide strips across the bath at the top of the tank at distances from the walls noted in Table 2. The effect of particle flux disturbances was greatest when two strips were used, blocking the long side of the tank: this caused a 15 percent increase of streamwise velocity fluctuations. Massive nonuniformities of this type, however, are not likely in view of the measurements illustrated in Fig. 8. Thus potential effects of particle number flux nonuniformities appear to be well within experimental uncertainties of the velocity measurements.

The final series of apparatus evaluation tests considered effects of the volume of the liquid bath. Results summarized in Table 2 show that reducing the volume of the bath by a factor of 32 caused only a slight increase in the measured streamwise velocity fluctuations. Thus, it is not likely that present results are influenced to a significant extent by the presence of bath surfaces. Nevertheless, final tests were carried out in the full-size bath.

Two types of flow visualization were used to characterize the tests: particle tracks and particle-wake tracks. The particle tracks were obtained by taking motion picture shadowgraphs of the particles as they fall through the central region of the test tank. Typical projections of the particle tracks for the three test conditions with 1.0 mm diameter particles are illustrated in Fig. 10. The number of tracks shown for each test condition has been varied proportional to the particle spacing, to suggest particle concentrations. The properties of the tracks shown, however, are representative of the behavior of the flow as a whole for each test condition.

For the low particle loading condition, illustrated in Fig. 10, the particles generally fall straight down, similar to isolated particles falling in a still liquid. As the particle loading increases, however, the particle paths become more erratic, with larger random deflections in the lateral direction. Such behavior is expected for particles moving in a turbulent continuous phase, and is a manifestation of turbulent particle dispersion. The remarkable feature of the results illustrated in Fig. 10, however, is that the turbulence field causing turbulent dispersion is entirely due to turbulence generated by the particles themselves (or turbulence modulation). More often than not, particles are displaced

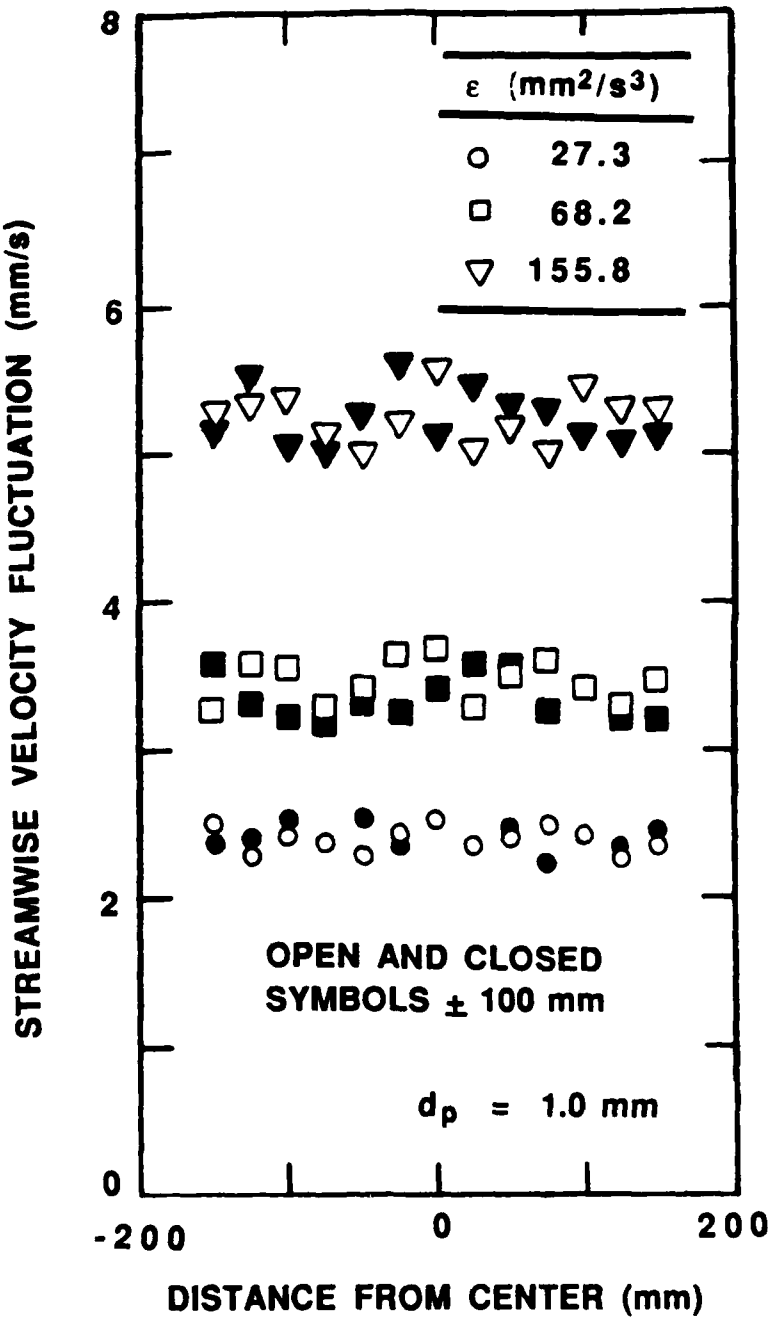

Figure 9 Streamwise velocity fluctuation distributions (d_p = 1.0 mm).

Table 2 Summary of Evaluation of the Homogeneous Particle Flow Apparatus[a]

Test	Percent Charge of $\overline{u'}$
Honeycomb at Surface	~ 0
Particle Flux Disturbances:	
50 mm width blocked (center of strip 60 mm from wall)	9
two 50 mm widths blocked symmetrically (centers of strips 50 mm from each wall)	15
50 mm width blocked in other direction (center of strip 70 mm from wall)	2
two 50 mm widths blocked in other direction (centers of strips 50 mm from each wall)	-6
Volume of Liquid Bath:	
full-depth 200 × 200 mm bath	~ 0
full-depth 100 × 100 mm bath	-4
half-depth 100 × 100 mm bath	3

[a] d_p = 1.0 mm at the lowest particle loading, e.g., $\dot{n}''$ = 3.67 kpart. $1m^2s$, ε = 27.3 m^2/s^3.

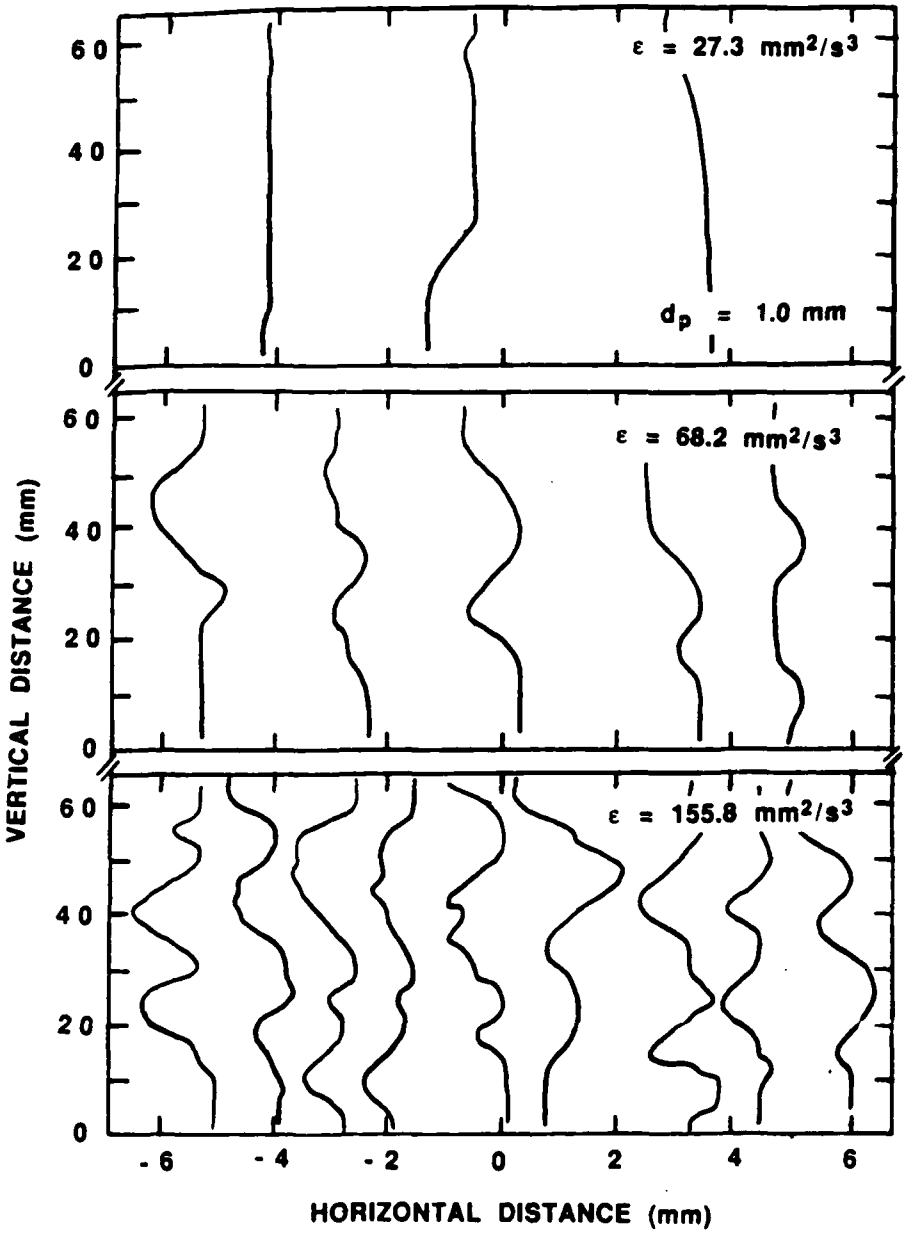

Figure 10 Typical particle tracks (d_p = 1.0 mm).

randomly back and forth across the mean vertical position of their projected trajectory. Occasionally, however, a particle undertakes a rather continuous deflection in a single lateral direction. We have not analyzed the flow as yet; therefore, whether this effect is systematic cannot be quantitatively determined. Such behavior, however, is relatively rare and is thought to be due to the finite probability of this type of deflection during any random-walk trajectory.

The second type of flow visualization involved coating the particles with a fluorescein dye and observing laser-induced fluorescence (LIF) from the dye track left by the particle. This was done by dissolving the powdered dye in water, wetting the particles with this solution and then allowing the solution to dry on the particle surface. This left a coating of the dye solution on the particle, which would redissolve as the particle passed through the water bath, leaving a dye track. A few dyed beads mixed with normal beads were allowed to fall through the bath. In general, the dye tracks exhibited greater degrees of lateral deflection than the particle tracks. This suggests greater degrees of turbulent dispersion for the liquid than the particles, which is generally the case for particle-laden flows having large relative velocities between the phases. Since the liquid is nearly stagnant, in the mean, the dye tracks remain within the field of view and continue to disperse within the turbulent field.

2.4.2 Phase Velocities

Thus far, predictions have only been completed for continuous-phase properties involving streamwise velocity fluctuations for 0.5 and 1.0 mm diameter particles. The domain of integration of equations (6) and (7) is infinite, therefore, it was necessary to truncate the calculations at some point. For present results, the calculations were truncated when velocities at the wake centerline reached 0.1 mm/s, since it was felt that contributions to the flow at lower centerline velocities could not be observed due to limitations of the LDA measurements. For present test conditions, this implied that calculations were truncated before the wakes became laminar; therefore, only equations (8) - (12), which are for turbulent conditions, were used to prescribe wake properties.

The general behavior of homogeneous particle-laden flows with respect to variations in particle number flux can be estimated immediately from equations (1) and (7), and then related to the dissipation of the flow through equation (3). The results can be summarized as follows: mean velocities are identically zero due to the configuration of the experiment; root mean square velocity fluctuations are proportional to $\dot{n}''^{1/2}$ or $\varepsilon^{1/2}$; correlation and spectrum tensors are proportional to $\dot{n}''$ or ε; and correlation and spectrum tensor coefficients are proportional to $\dot{n}''^{0}$ or ε^{0}.

Figure 11 is an illustration of predicted and measured phase velocities for 0.5 and 1.0 mm particles. Phase velocities are plotted as a function of dissipation, computed from equation (3). Mean and fluctuating particle velocities are denoted as Favre averages since these properties are particle averaged while continuous-phase velocities are time averages. The only prediction available at this time is streamwise continuous-phase velocity fluctuations.

Continuous-phase velocity fluctuations illustrated in Fig. 11 tend to increase according to the square root of the rate of dissipation which is consistent with the behavior estimated by equation (7). In fact, the quantitative comparison between predicted and measured streamwise velocity fluctuations is well within experimental uncertainties. Since

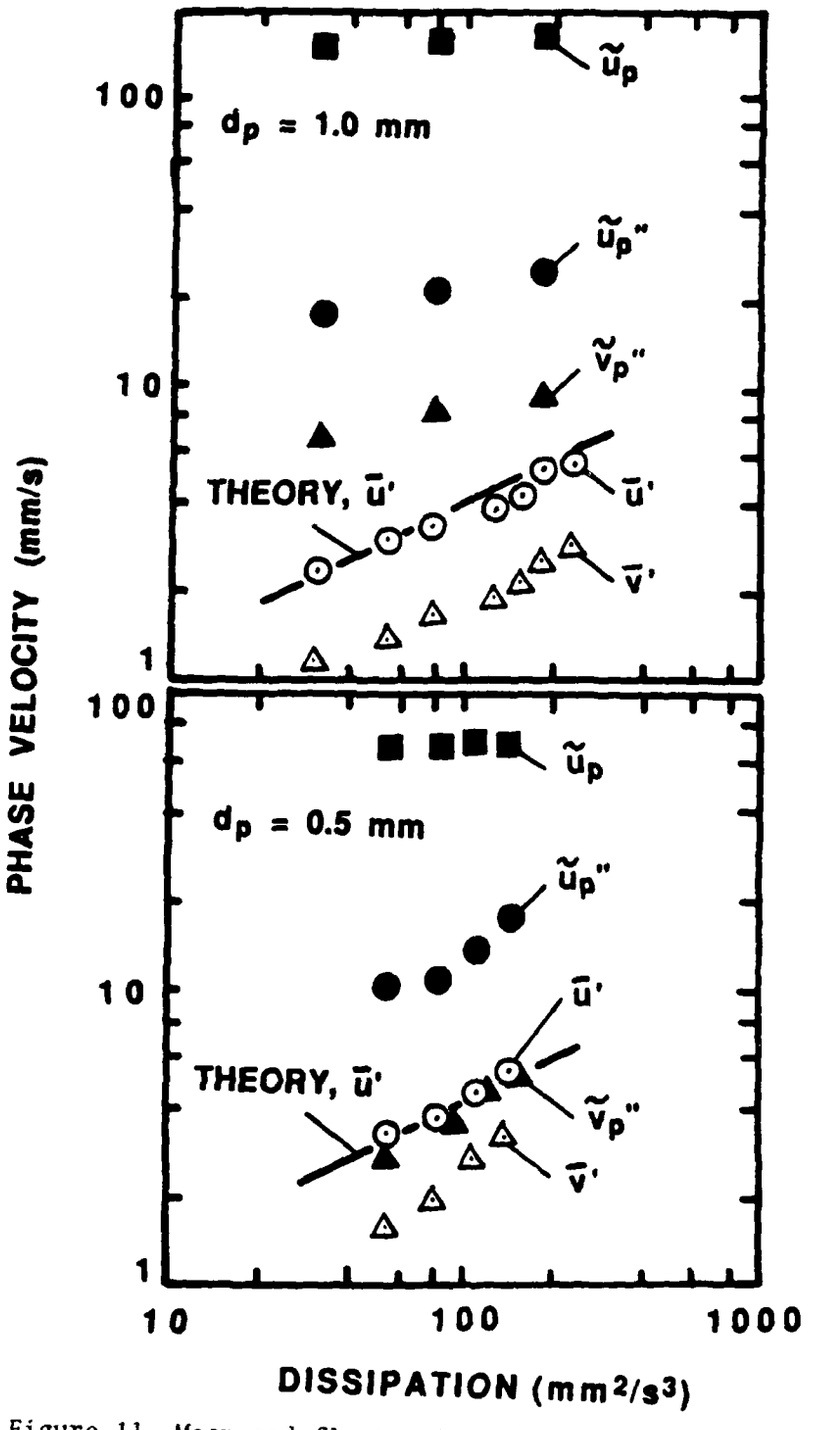

Figure 11 Mean and fluctuating phase velocities (d_p = 0.5 and 1.0 mm).

results for d_p = 0.5 and 1.0 mm are plotted separately they cannot be compared very easily, however, values of $\overline{u'}$ are nearly the same at a given value of ε for the two sizes. Thus, the rate of dissipation is the main factor which determines velocity fluctuations, at least for the relatively narrow range of Reynolds numbers considered thus far. Velocity fluctuations are strongly nonisotropic, with streamwise velocity fluctuations being roughly twice the magnitude of crosstream velocity fluctuations. This behavior is generally more characteristic of shear flows than homogeneous flows in conventional single-phase turbulence processes. However, such behavior is not unexpected when turbulence generation is primarily induced by a source moving in the streamwise direction.

Mean particle velocities illustrated in Fig. 11 increase slowly with increasing particle flux (or dissipation). This behavior is opposite to the variation of mean velocity during sedimentation processes where mean settling velocities tend to decrease as the particle volume fraction, and thus the particle number flux, increases (Batchelor, 1972). This difference in behavior follows from the fact that sedimentation is a random laminar process with low particle Reynolds numbers (Re << 1) while the present process is turbulent since particle Reynolds numbers are higher (Re > 10). In the case of sedimentation, the interaction between particles is primarily caused by the flow field immediately around the particle, not the wake (Batchelor, 1972). Thus, downflow in the particle flow field is counteracted by a mean bulk liquid upflow which tends to slow the particle settling rate as the particle concentration increases. In contrast, upflow rates are small when the wakes are turbulent while particles tend to be drawn into regions where downward wake velocities are largest due to entrainment flows. This increases mean particle velocities with increasing particle fluxes, see Hinze (1972). This contrasting behavior highlights the difficulties of generalizing the results of particle laden flows from a single set of experiments: a good theoretical understanding is needed in order to sort out seemingly whimsical differences in behavior as flow conditions are changed.

Another surprising feature of the results illustrated in Fig. 11 is that particle velocity fluctuations are larger than corresponding liquid velocity fluctuations — particularly streamwise velocity fluctuations. The main reason for this behavior is that the particles used during present tests are not completely monodisperse. Thus, larger particles have larger settling velocities which results in an apparent variation of streamwise velocity fluctuations. It is estimated that this effect accounts for roughly half the magnitude of the streamwise particle velocity fluctuations seen in Fig. 11. During subsequent development of the theory, by extending the integrations in equations (6) and (7) over particle size groups, it should be possible to quantify the effect similar to the particle-laden jet results of Parthasarathy & Faeth (1987).

Even correcting for the effect of particle size, particle velocity fluctuations are still comparable to continuous-phase velocity fluctuations. This is not unusual in instances where effects of turbulent dispersion are strong, since the inertia of the particles allows them to overshoot liquid-phase motion while the root mean square velocity fluctuations are only one measure (moment) of an entire spectrum of velocities. Thus, particles can pick out an optimal range of liquid velocity fluctuations where their response is optimized and this velocity range can be larger or smaller than the root mean square velocity fluctuations. Subsequent results will show that particles develop a wide range of turbulence scales, thus, an optimal range of optimal liquid velocity fluctuations is invariably present making self-generated turbulence fields particularly effective for turbulent dispersion of particles.

Probability density functions of streamwise and crosstream liquid velocity fluctuations are illustrated in Figs. 12-15. Predictions and measurements are shown for all loadings considered for the 0.5 and 1.0 mm diameter particles, although predictions are

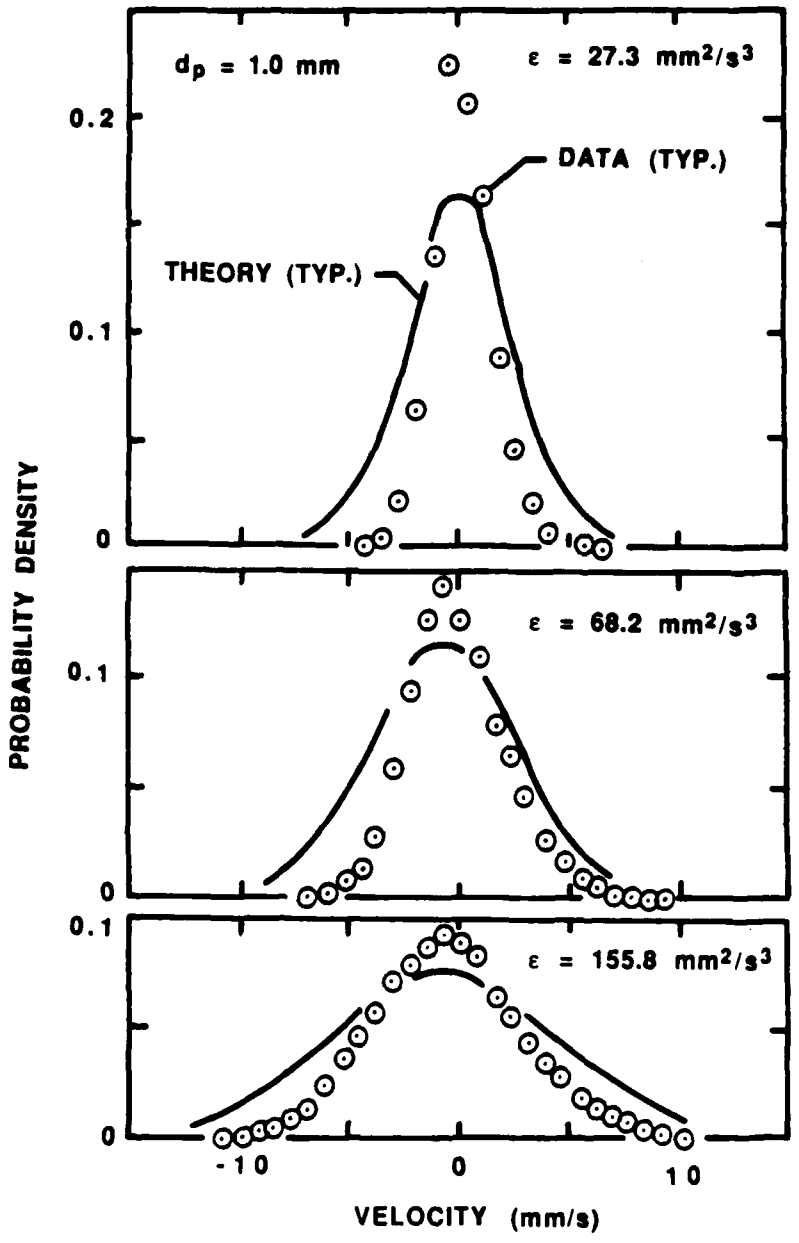

Figure 12 Probability density functions of streamwise velocity fluctuations (d_p = 1.0 mm).

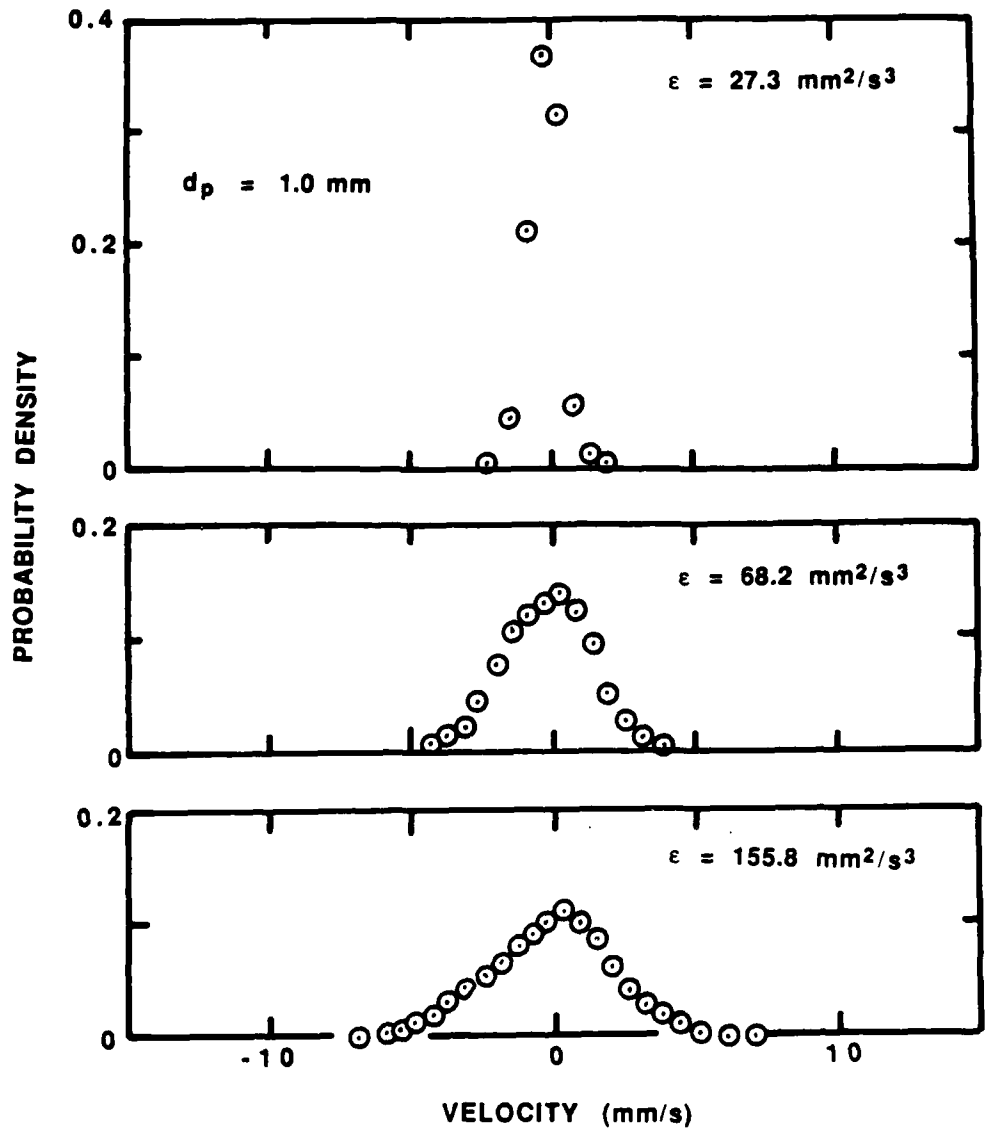

Figure 13 Probability density functions of crosstream velocity fluctuations (d_p = 1.0 mm).

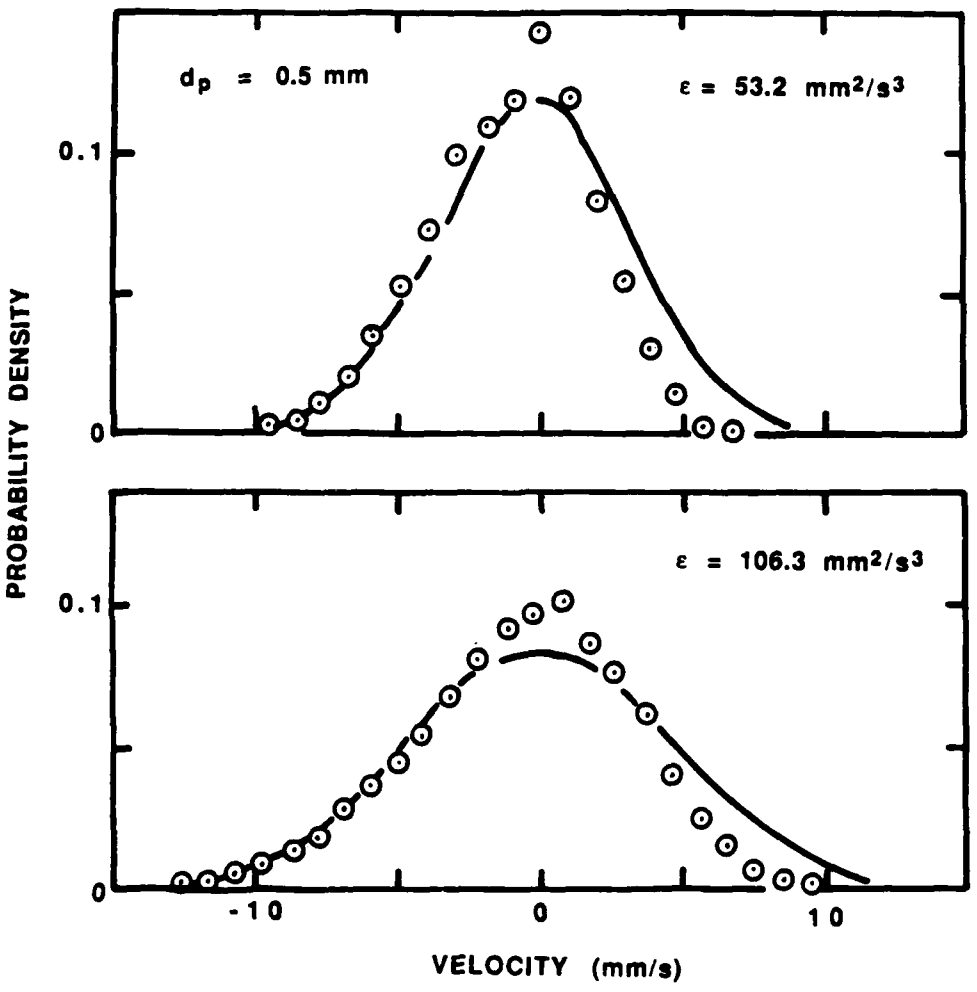

Figure 14 Probability density functions of streamwise velocity fluctuations (d_p = 0.5 mm).

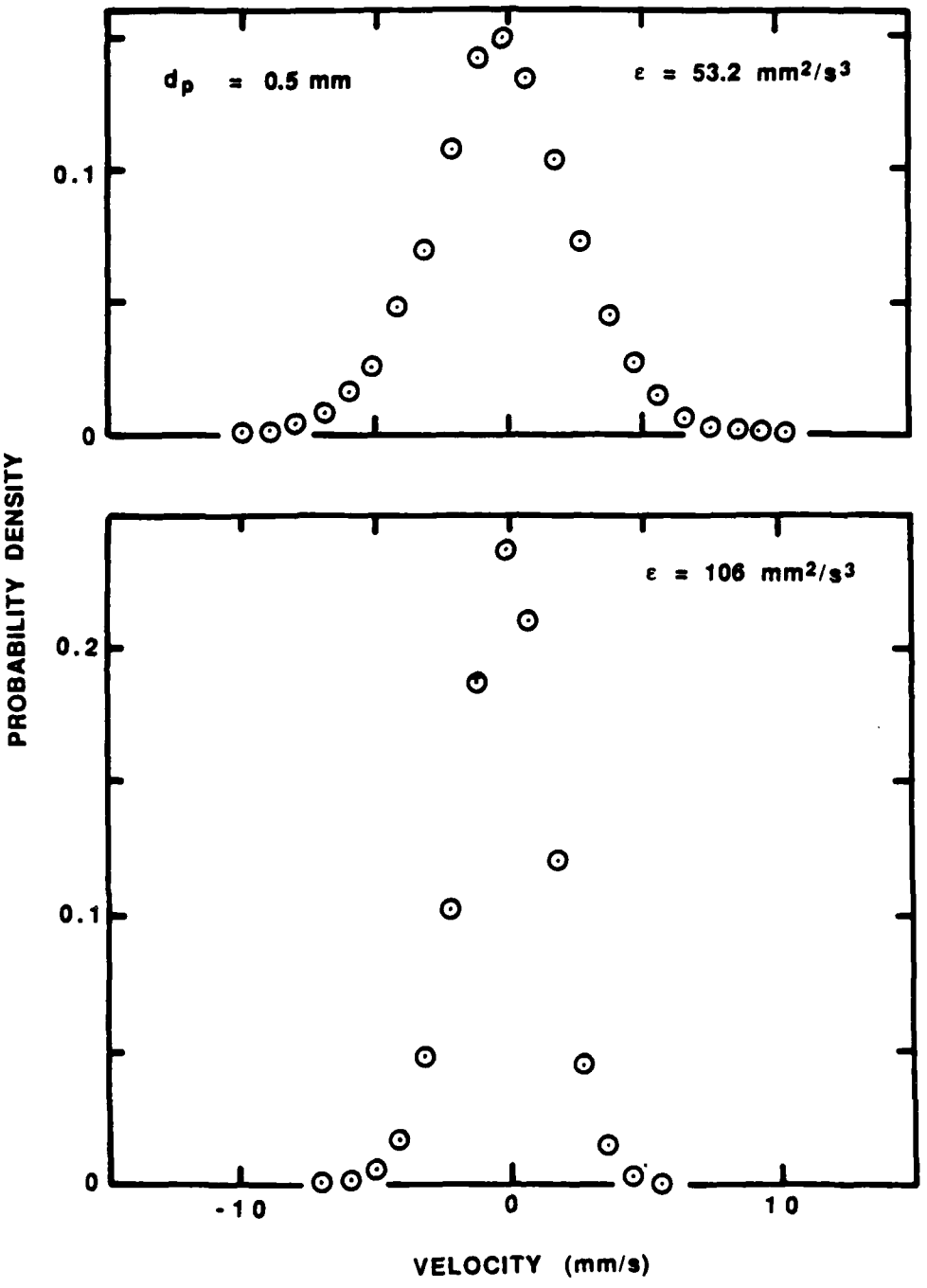

Figure 15 Probability density functions of crosstream velocity fluctuations (d_p = 0.5 mm).

limited to streamwise velocity fluctuations for the present. The stochastic theory implies that probability density functions of velocity fluctuations should be Gaussian (Rice, 1954). Where comparisons can be made, this is seen to be nearly the case with predictions providing reasonably good estimates of the measurements. The probability density functions of crosstream velocity fluctuations are narrower than the streamwise velocity fluctuations: this is a direct result of the larger velocity fluctuations in the streamwise than the crosstream directions seen in Fig. 11. Similarly, the broadening of the probability density functions with increased particle loading dissipation is also a manifestation of increases in velocity fluctuations with increasing rate of dissipation as noted earlier.

2.4.3 Correlations

Spatial and temporal correlation coefficients and spectra of velocity functions provide useful information concerning turbulence scales that is needed to interpret the properties of multiphase flows. Furthermore, this information must be known in order to compute turbulent particle dispersion as discussed in Section 2.3.2.

Predicted and measured temporal correlation coefficients of streamwise velocity fluctuations are illustrated in Fig. 16 for d_p = 0.5 and 1.0 mm. The region shown corresponds to delay times up to 15 s, which is the region of greatest interest for analysis of turbulent particle dispersion. Measurements were actually carried out for delay times up to 130 s, however, which showed that the correlations actually become negative for times greater than 40 s (reaching a maximum negative value of 0.1 for delay times of 40-60 s and then gradually approaching zero) yielding a functional form similar to a Frenkiel function. These lengthy periods of finite correlation are characteristic of wake properties in a stagnant environment since the wake persists with significant disturbances of the local velocity field long after the particle has passed. For example, if the particle motion had continued unimpeded by the finite depth of the present liquid bath, the particles would be 7-15 m below the observation position for delay times of 100 s for present test conditions. The fact that particles stop much sooner at the bottom of the present liquid bath is irrelevant for the development of the flow due to the parabolic nature of wake properties. Evidence for this is provided by the measurements of streamwise velocity flujctuations which showed little affect of the volume of the liquid bath.

As noted earlier, present theory indicates that temporal correlation coefficients should not depend on particle number fluxes. Results illustrated in Fig. 16 show that this is not the case for present measurements: correlation coefficients consistently decrease more rapidly as particle loading increases. This is not thought to be a deficiency of the general stochastic theory based on Poisson statistics. Deficiencies of the canonical wake used in the theory are a more likely source of the discrepancy. There are several potential difficulties, as follows: effects of turbulent particle dispersion, effects of turbulent dispersion of the wakes themselves, effects of the upflow velocity of the bulk liquid, and direct effects of wake turbulence. As noted in connection with the results illustrated in Fig. 10, particle motion becomes increasingly sinuous as the particle loading is increased due to turbulent dispersion. This causes the particle wakes to become sinuous as well, rather than the straight wake path appropriate for an infinitely-dilute particle flow which is assumed during current analysis. A sinuous wake would naturally show a more rapid decrease in correlation coefficients than a straight wake, with any tendency for periodicity being indicated by periods of negative correlation: trends that clearly correspond to current measurements. Fortunately, this is not a truly nonlinear phenomena and can be handled by correcting the canonical particle wake by allowing for turbulent particle dispersion. Thus, once particle trajectories have been simulated it should be possible to construct more realistic canonical wakes.

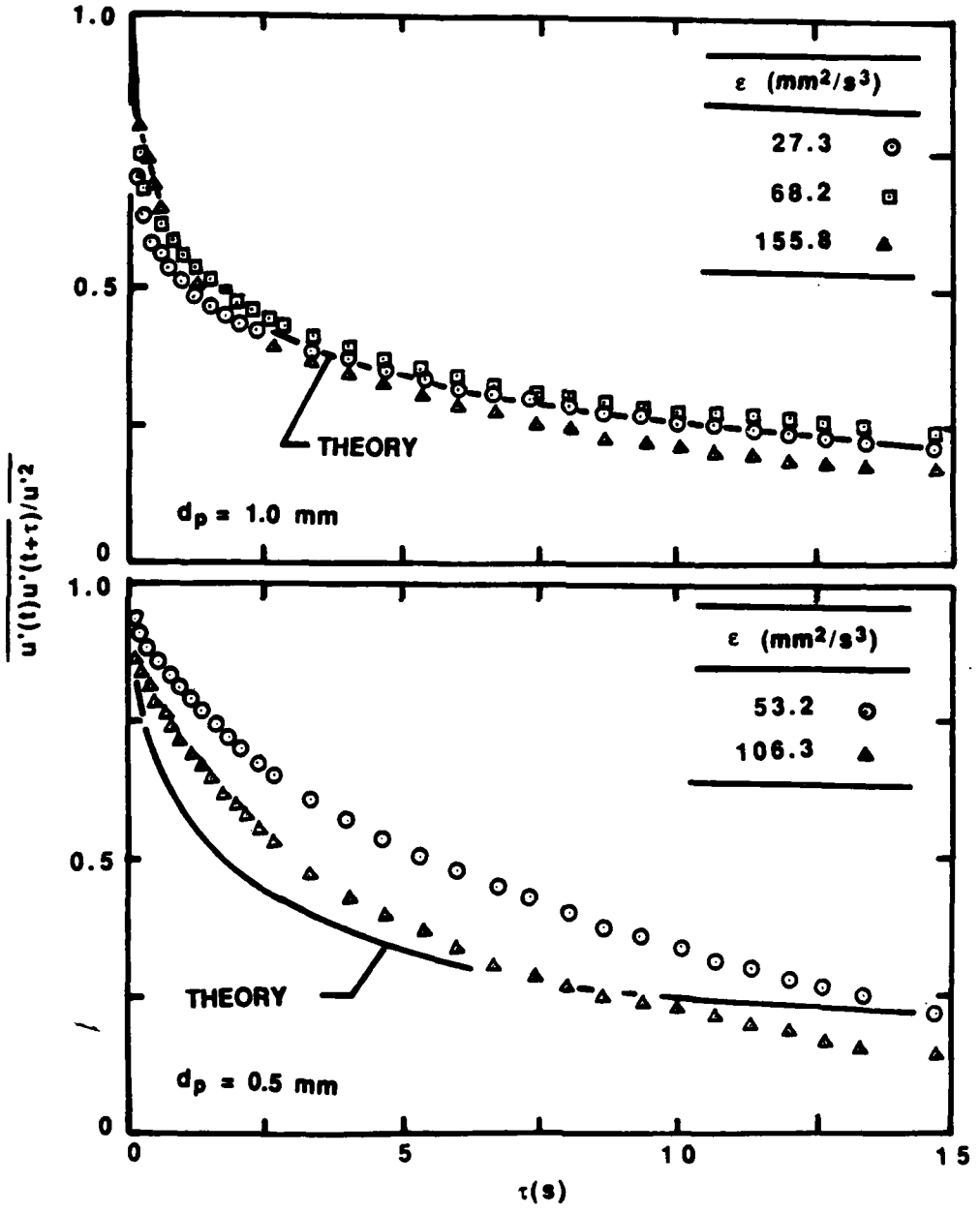

Figure 16 Temporal correlations of streamwise velocity fluctuations (d_p = 0.5 and 1.0 mm).

The second effect, turbulent dispersion of the wakes themselves, was quite evident from the fluorescein dye wake visualization measurements discussed earlier. Even at short times, the wakes were deflected to a greater extent than the particles which would tend to reduce resulting temporal correlations at a fixed point of observation. The degree of wake deflection, and its rapidity, also increased with increasing particle loading. This behavior is also consistent with the observations illustrated in Fig. 16. Potentially, the problem could be handled by considering the dispersion of fluid points along the axis of the wake.

The third effect relates to liquid upflow and is analogous to the mechanism considered by Batchelor (1972) for reduced sedimentation velocities at high particle loadings. Each wake has a downward velocity defect which must be compensated by upflow in the surroundings in order to maintain an overall mean bulk velocity of zero (neglecting the small displacement velocity). This upflow velocity increases with increasing particle loading and causes wake velocities to approach zero more rapidly and then become negative for a time. This would tend to reduce temporal correlations more rapidly with time when particle loadings are increased as observed during the present experiments. This effect is probably also partly responsible for negative portions of the temporal correlations observed during present measurements for delay times somewhat longer than those illustrated in Fig. 16.

Finally, direct effects of wake turbulence cannot be excluded as a potential reason for temporal correlations to decrease more rapidly with increased particle loading. This phenomena, however, seems less likely than other mechanisms since it should be present at all particle loadings and should scale directly with increased particle loading.

The comparison between predictions and measurements in Fig. 16 is encouraging but areas of difficulty can still be seen. Results for d_p = 1.0 mm are quite good. Theory and experiment are in close agreement for low particle loadings while correlations decrease more rapidly than predicted for higher particle loadings for the reasons just discussed. This agreement does not persist at longer delay times, however, since the theory never yields a region of negative correlation as observed during the measurements. Effects of upflow are suspected to be the cause of this difficulty and this mechanism will be considered during subsequent calculations.

Discrepancies between predictions and measurements are greater for d_p = 0.5 mm than for d_p = 1.0 mm in Fig. 16. The specific reasons for this behavior are not known but could be due to difficulties with the measurements. In particular, particle spacings are smallest for d_p = 0.5 mm which increases the difficulty of the measurements, see Table 1. Measurements for the 2.0 mm particles should help resolve whether this is the problem. Upflow effects may also be more significant due to higher particle loading, similar to conditions considered by Batchelor (1972); thus, difficulties with the theory may be responsible as well. Finally, it should be recalled that present theory does not account for direct contributions of wake turbulence. Due to the low wake Reynolds numbers of present tests, however, this phenomenon does not advance itself as a major source of discrepancies between predictions and measurements. Furthermore, errors are greater for the smaller particles, which have the lower Reynbolds numbers and thus lower levels of wake turbulence. Nevertheless, potential effects of wake turbulence will be considered during subsequent analysis.

Measured temporal correlation coefficients for crosstream velocities are illustrated in Fig. 17 for d_p = 0.5 and 1.0 mm. Predictions have not been completed as yet for the properties of crosstream velocities. In this case, the correlation coefficients are illustrated out to a delay time of 130 s so that the negative portion of the correlation can be seen. The

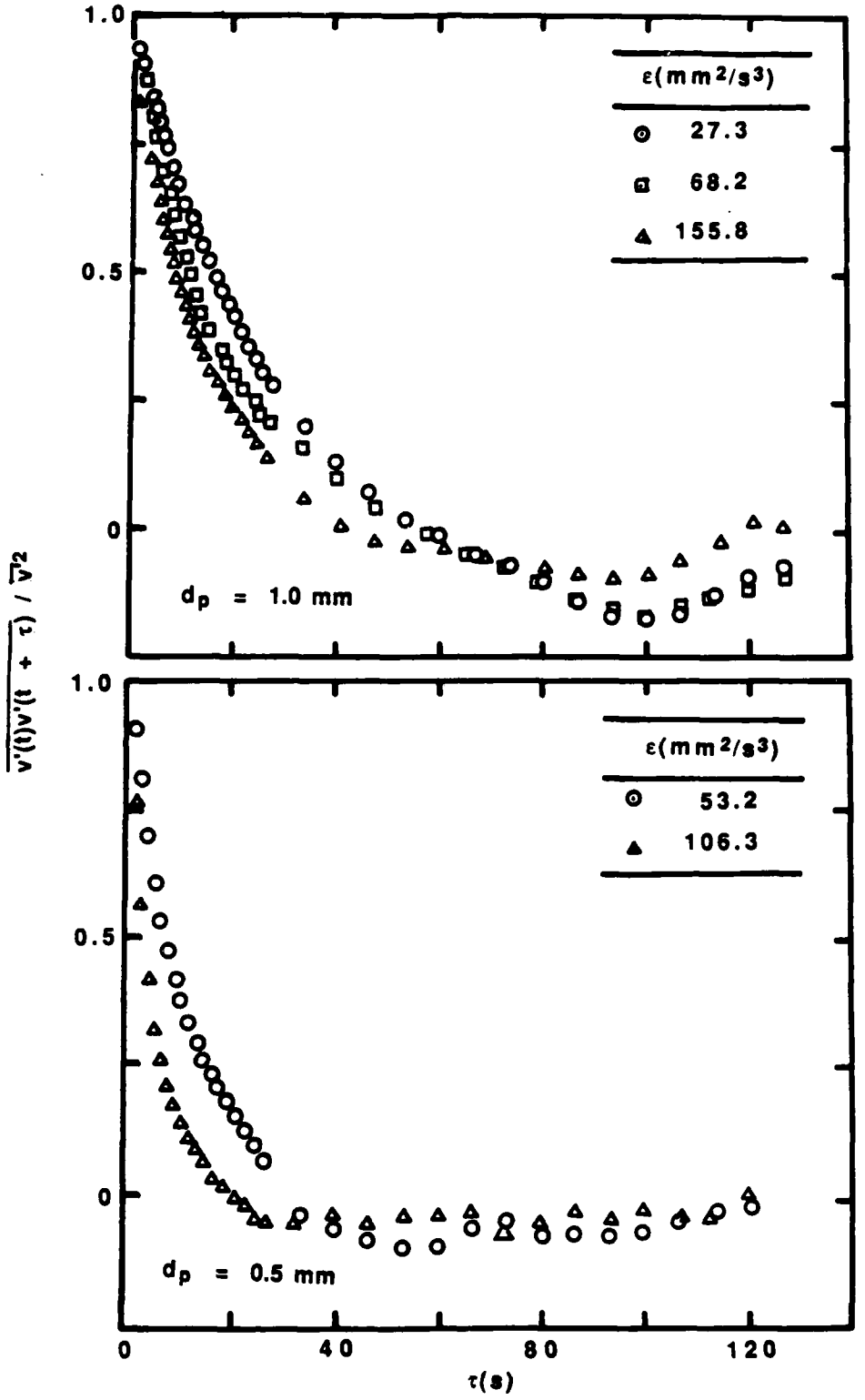

Figure 17 Temporal correlations of crosstream velocity fluctuations (d_p = 0.5 and 1.0 mm).

behavior at long times is somewhat similar to correlation coefficients for streamwise velocity fluctuations, although crosstream correlation coefficients reach somewhat higher negative values. Similar to the streamwise correlations, there is a consistent tendency for crosstream correlations to decrease more rapidly with increased particle loading, probably for the same reasons.

Predicted and measured power spectral densities of streamwise and crosstream velocity fluctuations are illustrated in Figs. 18 and 19. A remarkable feature of these results is the large frequency range of the spectra even though initial wake Reynolds numbers are relatively low. This behavior is caused by the fact that mean velocity distributions in the particle wakes contribute to the turbulent field since particle arrival times are random. Thus, the mechanism of present flows is very different from single-phase turbulent flows and conventional turbulence scaling rules are not really appropriate. Since spectra are plotted logarithmically, and tend to emphasize the high-frequency properties of the flow, effects of particle loading are relatively small which is consistent with the stochastic analysis.

The spectra illustrated in Figs. 18 and 19 have a plateau region at low frequencies, a region of decay, a second plateau region, and a final region of decay. The second plateau and final region of decay, however, are probably due to experimental difficulties. Present sampling rates are greater than 10^3 Hz, allowing resolution of frequencies up to 10^3 Hz while still satisfying the Nyquist sampling requirements. The spectra were computed after digitizing the analog output from the burst-processor; the analog output consisted of step variations in velocity, a new step for each new velocity determination by the burst counter. Nevertheless, the step waves cannot provide information at the smallest frequencies of the flow and introduce step noise due to jumps in the velocity signal. Typical of square wave jumps, this introduces higher frequency components into the measurements which are called step-noise while the loss of information acts like a low-pass filter. Adrian and Yao (1987) have shown that the main effect of step noise in such spectra is to act as a low-pass filter at a frequency corresponding to the mean data rate. Significant distortion of the actual spectrum starts occurring at frequencies one-twentieth of the mean data rate. This is usually seen as a plateau in the spectrum where the slope changes to a second-order decay at higher frequencies. This behavior is consistent with the second plateau and the second-order fall off of the power spectra seen at the highest frequencies illustrated in Figs. 18 and 19. Step noise effects are more significant for crosstream spectra in Fig. 19 due to the lower intensity of crosstream velocity fluctuations, see Fig. 11.

The agreement between predicted and measured streamwise power spectral densities, seen in Fig. 18, is quite encouraging once effects of step noise at high frequencies are recognized. The location of the break frequency, and its shift with particle size, is predicted quite well. The rate of decay of the spectra, up to the second plateau due to step noise, is also predicted reasonably well. However, the fact that this agreement was achieved without considering direct contributions of wake turbulence is still a matter of concern. The low Reynolds numbers of the present wakes offer an explanation since turbulence intensities of wakes tend to be reduced at low wake Reynolds numbers (Uberoi & Freymuth, 1970). Unfortunately, there is virtually no information available concerning the turbulence properties of wakes at conditions approaching those of present tests. This issue deserves further consideration in the future.

Measured spatial correlation coefficients of streamwise velocity fluctuations for d_p = 0.5 and 1.0 mm are illustrated in Figs. 20 and 21. Figure 20 is an illustration of the variation of the correlation for two points separated in the streamwise direction while Fig. 21 provides the variation of the correlation for two points separated in the crosstream

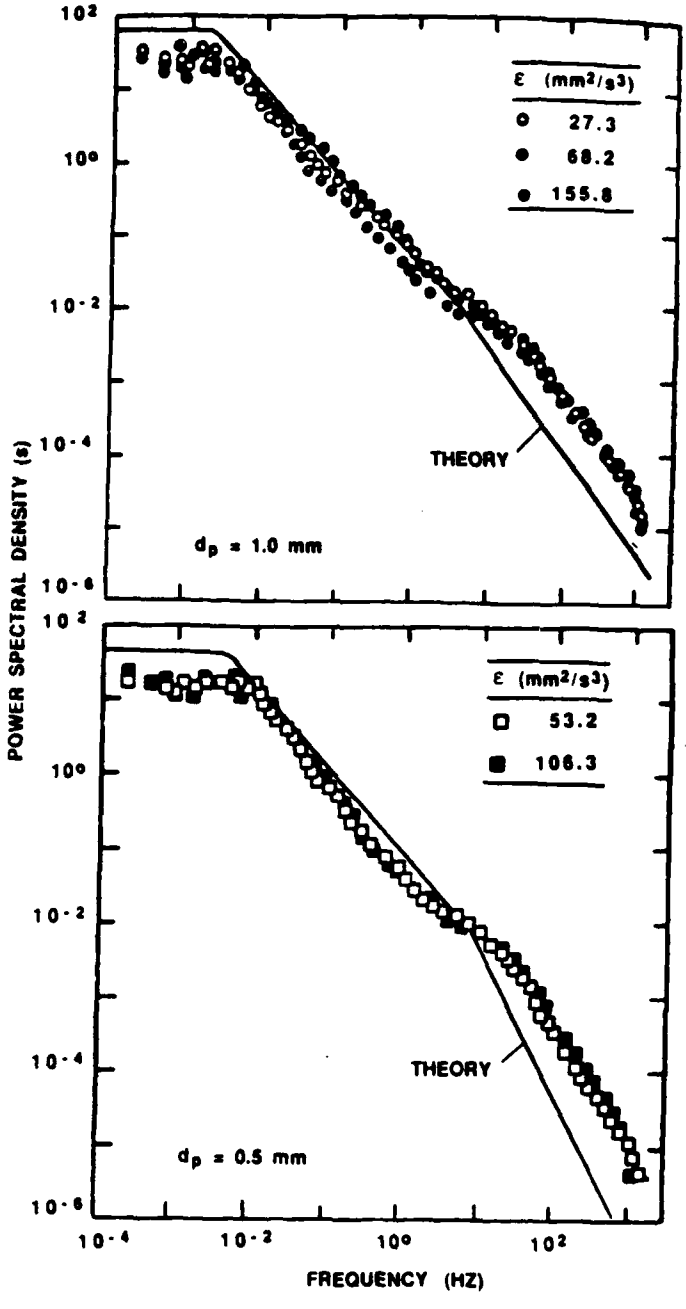

Figure 18 Power spectral densities of streamwise velocity fluctuations (d_p = 0.5 and 1.0 mm).

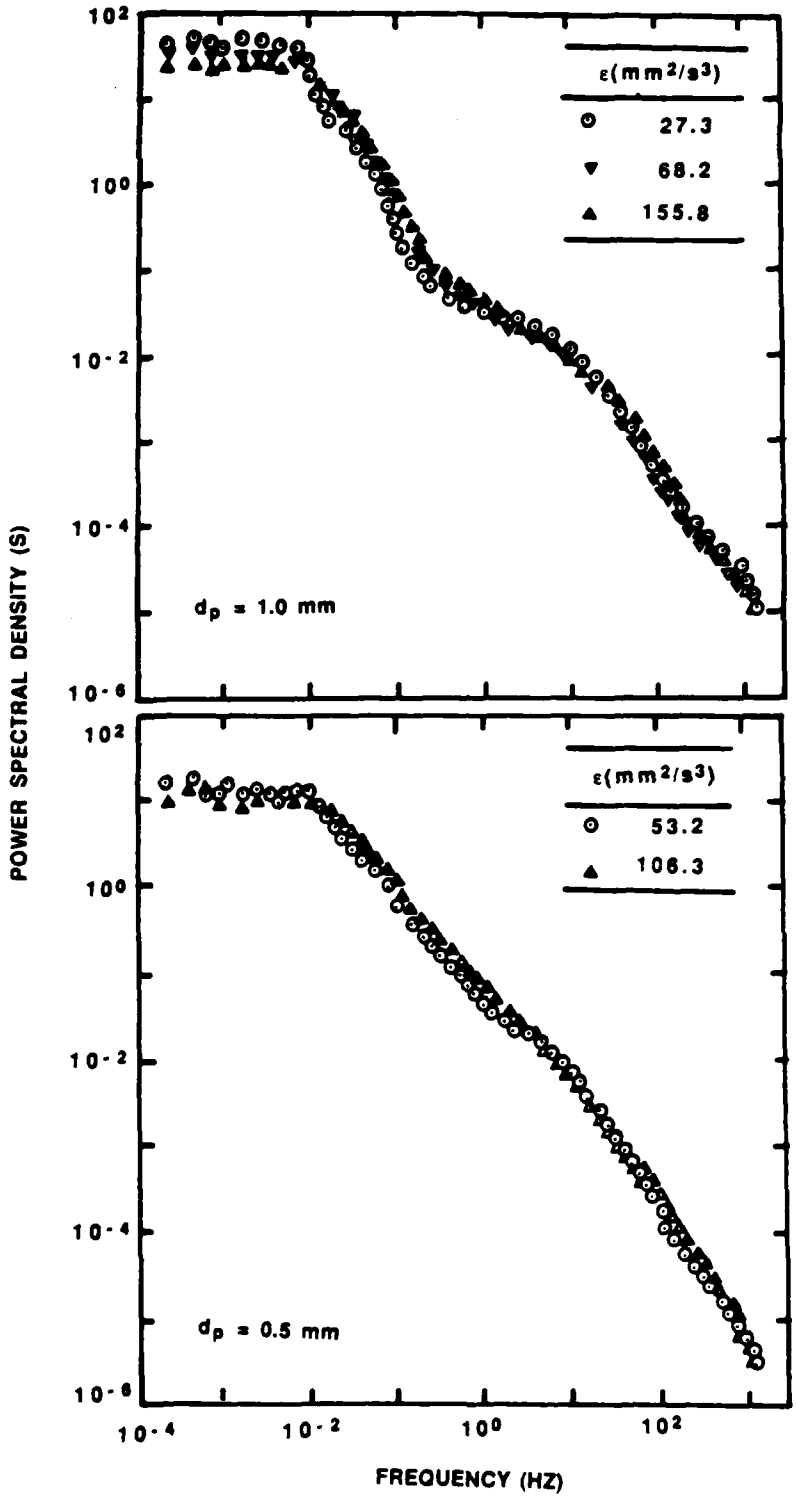

Figure 19 Power spectral densities of crosstream velocity fluctuations (d_p = 0.5 and 1.0 mm).

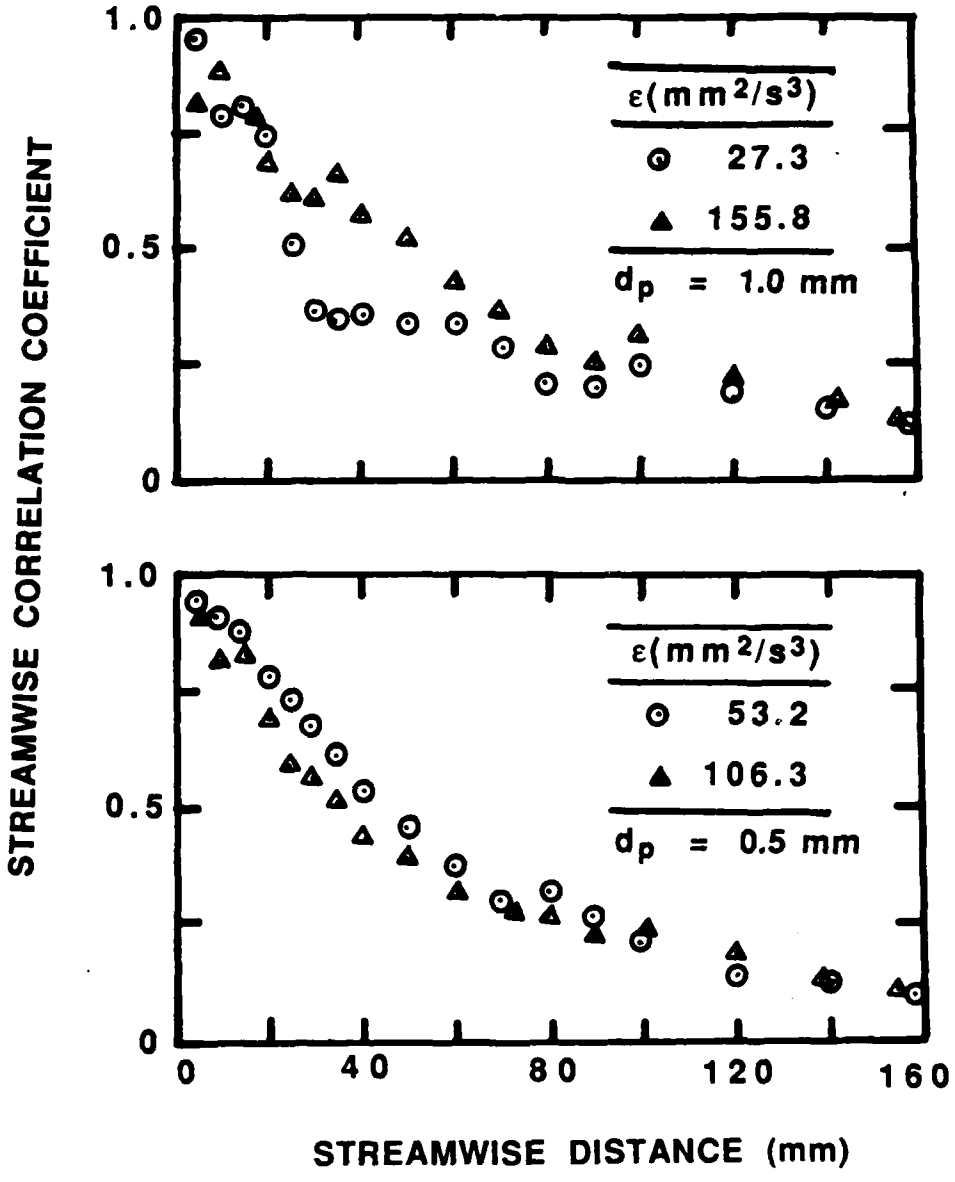

Figure 20 Spatial correlations of streamwise velocity fluctuations in the streamwise direction (d_p = 0.5 and 1.0 mm).

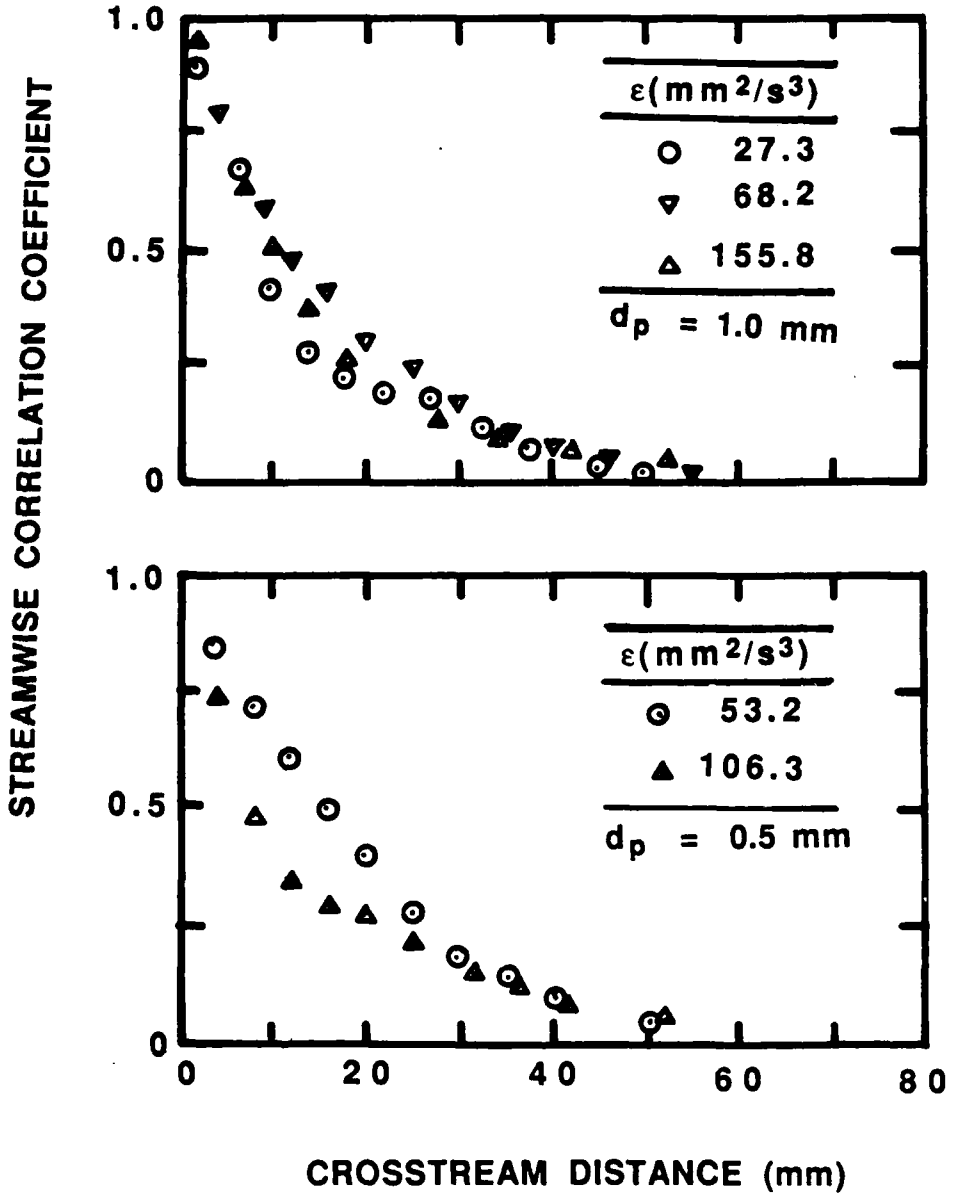

Figure 21 Spatial correlations of streamwise velocity fluctuations in the lateral direction (d_p = 0.5 and 1.0 mm).

direction. Changes in the particle loading do not cause significant changes in the correlations, within experimental uncertainties, in agreement with the findings of the stochastic analysis. Changes in particle size do not influence the correlations to a significant degree as well. However, decay of the correlations in the streamwise direction is much slower than in the crosstream direction, e.g., integral scales in the streamwise direction are on the order to 60-80 mm in comparison to integral scales in the crosstream direction on the order of 20-30 mm. However, this behavior is consistent with the anisotropy of other turbulence properties measured in these flows. Finally, anisotropic length scales are also consistent with the boundary layer properties of canonical wakes, where variations of flow properties in the crosstream direction are much more rapid than in the streamwise direction.

2.5 Summary

Development of the test arrangement for homogeneous particle-laden flows has been completed. The arrangement consists of a uniform flux of glass spheres (d_p = 0.5, 1.0 and 2.0 mm) falling in a stagnant water bath. Measurements are made of mean and fluctuating phase velocities and temporal and spatial correlations and power spectral densities of continuous-phase velocities, using a two-point phase-discriminating laser Doppler anemometer; and particle number fluxes, using a Mie scattering system. Preliminary tests have established that the flow near the center of the water bath (the central 75 percent) is homogeneous; and that the flow is relatively independent of disturbances at the liquid surface, disturbances of particle fluxes, and the volume of the liquid bath. Measurements have been completed for d_p = 0.5 and 1.0 mm and are currently in progress for d_p = 2.0 mm.

The continuous-phase properties of the homogeneous particle-laden flows were analyzed using a stochastic approach. Major assumptions of the analysis are as follows: uniform mean particle flux and random particle arrival times (Poisson statistics); wake properties can be linearly superimposed to compute flow properties; and while mean velocities in turbulent particle wakes were considered, the direct contribution of wake turbulence was ignored. A stochastic analysis to predict particle trajectories in the turbulent field was also developed, based on statistical time series techniques. Computations have been completed for continuous-phase properties involving streamwise velocities for particle diameters of 0.5 and 1.0 mm.

This is a report of progress and findings are only tentative pending completion of both measurements and analysis. Results thus far show that particle-generated turbulence can cause significant levels of turbulent particle dispersion — particularly at high particle loadings. Continuous-phase velocity fluctuations are proportional to the square root of the dissipation rate of turbulence kinetic energy and are relatively independent of particle size, in accord with the stochastic predictions. Stochastic predictions of streamwise velocity fluctuations, temporal correlations and power spectral densities were also in reasonably good agreement with the measurements. This indicates that the innately random nature of particle flows must be considered at the outset and that the present stochastic analysis provides a promising approach for treating their properties.

Current work seeks to complete measurements for 2.0 mm diameter particles using the present test arrangement, and to complete analysis of flow properties using stochastic methods for both the dispersed and continuous phases. Subsequent experiments will consider particles falling in stagnant air, as opposed to water, in order to study effects of particle dynamics since virtual mass and Basset history forces are significant for particles moving in water but not for particles moving in air. Effects of the turbulence properties of

the continuous phase will also be examined by considering particle-laden flows in grid-generated turbulence. Finally, modification and extension of the stochastic analysis to treat the new experimental conditions will be undertaken as well.

3. DENSE-SPRAY STRUCTURE

3.1 Introduction

The investigation of dense-spray phenomena is considering the near-injector region of nonevaporating pressure-atomized sprays, e.g., round water jets injected into still air. Further definition of the flow requires consideration of breakup regimes. Ranz (1958) prescribed four regimes of liquid jet breakup (drip, Rayleigh, wind-induced and atomization), based on the liquid and gas Weber numbers of the flow, which are defined as follows:

$$We_{(f \text{ or } g)} = (\rho_f \text{ or } \rho_g)\, u_o^2\, d/\sigma \tag{30}$$

The properties of the four regimes, and their breakup criteria, are summarized in Table 3. Reitz (1978) further subdivides wind-induced breakup into first and second wind-induced breakup regimes, which are also noted in the table. The present investigation is limited to the wind-induced and atomization breakup regimes, since they are the most important regimes for practical application. In particular, the second wind-induced and atomization breakup regimes involve breakup near or at the injector exit, respectively, yielding drop diameters much smaller than the injector passage diameter — attributes that are needed for high-intensity combustion processes.

There are several flow regions within a spray when it is operating in the atomization regime, as illustrated in Fig. 22. Within the injector, and far downstream if the liquid is evaporating, we have single-phase flows. The dense-spray region is near the injector exit and involves a contiguous liquid core surrounded by a drop-containing mixing layer. The region of the mixing layer near the liquid core contains a complex flow configuration which results from removal of liquid from the core as part of the atomization process: globules of liquid, ligaments and drops. The outer edge of the shear layer, however, has characteristics similar to a dilute spray, consisting of rather widely spaced spherical drops with liquid volume fractions less than 1 percent. The boundary between the dense- and dilute-spray regions is not well defined, however, most studies of dilute sprays have been limited to the region downstream of the contiguous liquid core, as illustrated n Fig. 22. This region can be quite far from the injector, e.g., liquid cores can extend 200-400 injector diameters from the jet exit for injection into atmospheric pressure gases. Thus, although little is known about the dense spray region, processes in dense sprays have an important influence on the structure and mixing properties of sprays.

Past studies of dense sprays have recently been reviewed by Faeth (1987) and only the main features of earlier work will be considered here. Earlier work has been relatively limited due to the difficulties of making measurements in a multiphase flow where liquid volume fractions vary over a wide range. Phinney (1973), Hiroyasu et al. (1982) and Chehroudi et al. (1985) have attempted to measure the length of the all-liquid core, however, their results scatter widely and are not in good agreement.

Table 3 Round Liquid Jet Breakup Regimes

Breakup Regime	Properties		Breakup Criteria	
	Location	Drop Diameter	We_f	We_g
Drip	x = 0	> d	< 8	< 0.4
Rayleigh	x > 0	> d	> 8	< 0.4
Wind-Induced	x > 0		> 8	0.4-13[b]
First		0.1d-d		
Second		< d		
Atomization	x = 0	<< d	> 8	13[b] <

[a]Criteria due to Ranz (1958).
[b]Miesse (1955) recommends 40.3 instead of 13 for transition to atomization.

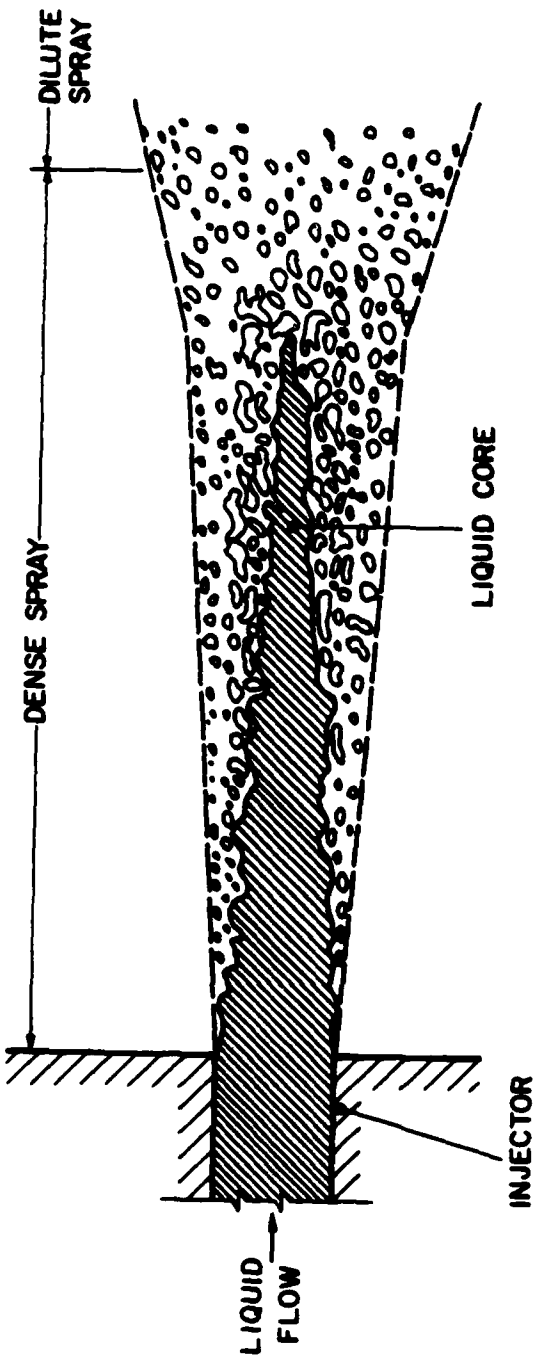

Figure 22 Sketch of the near-injector region of pressure atomized sprays.

In an attempt to circumvent the difficulties of dealing with a flow having widely varying phase topography and a variety of physical phenomena — collisions, breakup, interphase transport with closely-spaced dispersed-phase elements, etc. — use of the locally-homogeneous flow (LHF) approximation to analyze dense sprays has been studied by a number of workers. The LHF approximation implies that interphase transport rates are infinitely fast, so that relative velocities between the phases are small in comparison to flow velocities and local thermodynamic equilibrium is maintained, i.e., it is assumed that the development of a dense spray is controlled by turbulent mixing. The effectiveness of this approach, however, is controversial. Bracco (1983) and Wu et al. (1983, 1984) report measurements of spray angles and drop velocities in nonevaporating pressure-atomized sprays at high pressures, concluding that LHF analysis was effective for their test conditions. On the other hand, Faeth (1983, 1987), Mao et al. (1980, 1981), Shearer et al. (1979), Shuen et al. (1983, 1985, 1986), Solomon et al. (1985, 1985a, 1985b), Sun & Faeth (1986, 1986a), Sun et al. (1986) and Parthasarathy & Faeth (1987), all working in this laboratory, generally found that the LHF approach overestimates the rate of development of multiphase jets. Even findings in high-pressure sprays suggested problems with LHF analysis, since drop inertia is significant in the rapidly decelerating flow field of typical sprays (Mao et al., 1980, 1981). Experimental evidence on both sides of the controversy generally comes from dilute portions of the spray, however, and its relevance to dense-spray processes is questionable.

The present investigation was undertaken to help resolve controversies concerning the structure and extent of the dense spray region, and the effectiveness of LHF analysis for dense sprays. The findings of the first phase of the work have been reported by Ruff & Faeth (1987) and Ruff et al. (1987, 1988). The objectives were to complete nonintrusive measurements of spray structure near the injector exit in order to gain a better understanding of the breakup and mixing properties of the flow. The experiments involved nonevaporating water jets in still air at atmospheric pressure with the jets in the wind-induced and atomization breakup regimes. Measurements included: flow visualization using flash photography, liquid volume fractions using gamma-ray absorption, and air entrainment rates and mean and fluctuating liquid velocities at the jet exit using laser-Doppler anemometry (LDA). Measurements were compared with predictions based on the LHF approximation along the lines of Mao et al. (1980, 1981) with careful calibration of estimates of mixing rates from measurements in single-phase flows (Faeth, 1987).

The findings of Ruff & Faeth (1987) and Ruff et al. (1987, 1988) have helped to clarify some issues of dense sprays. Measured and predicted time-averaged liquid volume fractions along the axis of sprays having fully-developed and slug flow jet exit conditions are illustrated in Fig. 23. The measurements show that the rate of development of the flow and the extent of the liquid core (where $\alpha_f = 1$) are very dependent on the state of development of the flow at the jet exit and the breakup regime. Fully-developed flow and atomization breakup yield the fastest rates of flow development. The sensitivity of the flow to jet exit conditions probably accounts for past controversy concerning the length of the contiguous liquid core due to problems of providing well-defined jet exit conditions with small injector passages.

Predictions using the LHF approximation are reasonably good for atomization breakup in the dense-spray region near the jet exit, including correct predictions of the sensitivity of the flow to jet exit conditions, see Fig. 23. However, predictions begin to fail as the dilute spray region is entered ($\overline{\alpha_f} < 0.2$) and the theory provides no warning of vastly reduced mixing rates as the flow passes into the wind-induced breakup regime where drop sizes become larger. Difficulties with the LHF approximation in dilute sprays can

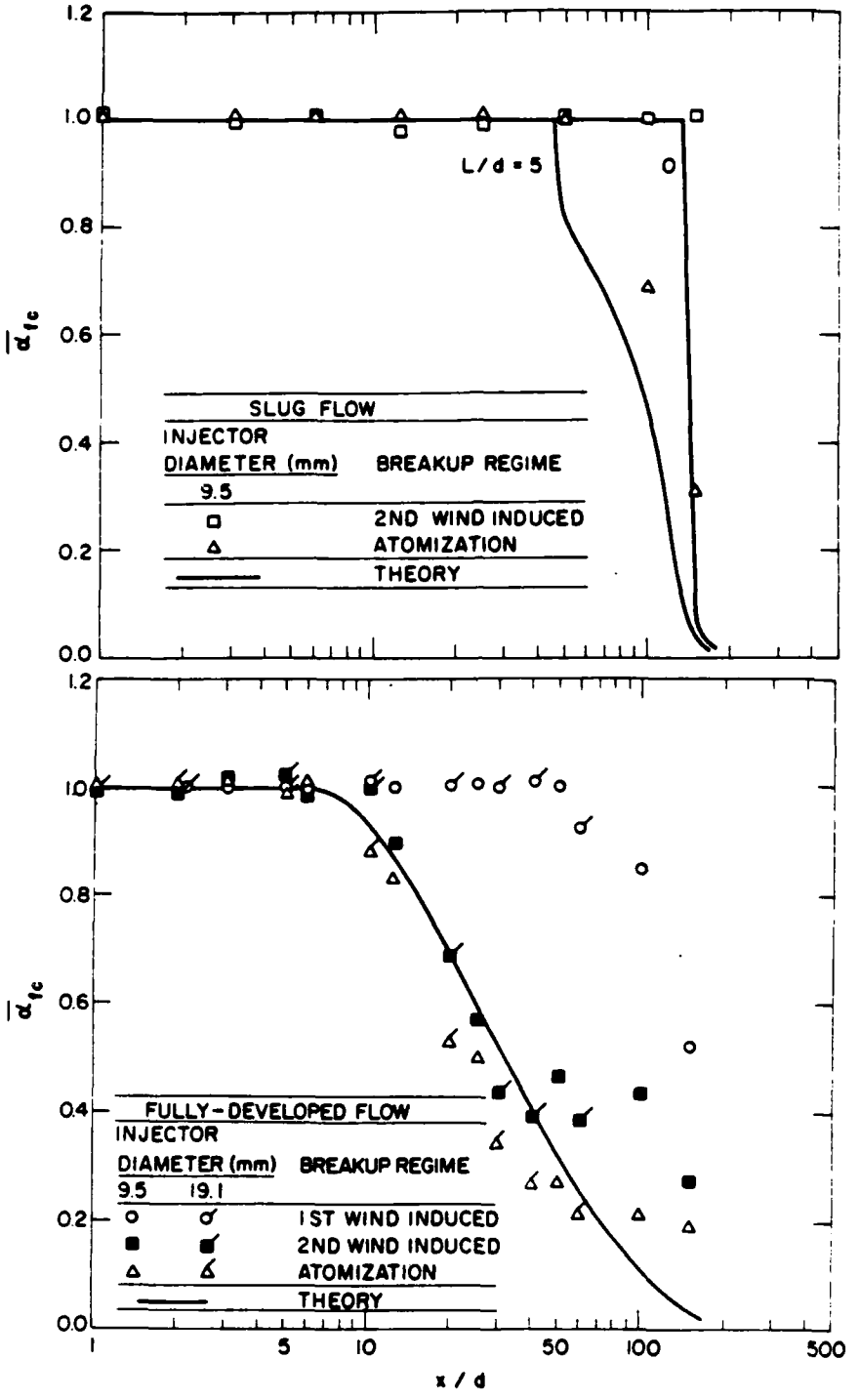

Figure 23 Time-averaged liquid volume fractions along axis for fully-developed and slug flow.

also be seen for the radial profiles of liquid volume fractions illustrated in Fig. 24. These test conditions involve fully-developed jet exit conditions and atomization breakup; thus, predictions are quite good in the dense-spray region. However, predictions using the LHF approximation clearly overestimate the rate of development of the flow far from the injector where the spray becomes dilute, which is consistent with earlier findings in this laboratory (Faeth, 1987).

Predicted and measured entrainment rates for fully-developed and slug flow jet exit conditions are illustrated in Fig. 25. Rates of entrainment increase as jet Reynolds numbers are increased — passing through the first wind-induced, second wind-induced, and atomization breakup regimes. This occurs since drop sizes become progressively smaller with increasing Reynolds number which improves mixing between the phases. The LHF predictions are approached as jet Reynolds numbers are increased but predictions clearly overestimate the measurements for present conditions. This behavior follows since entrainment is strongly influenced by properties near the edge of the flow where the spray is dilute and the LHF approximation is less satisfactory. This implies that the LHF approximation actually represents behavior at the limit of infinitely large jet Reynolds numbers where drops become infinitely small. Thus practical sprays invariably involve effects of separated flow — particularly in the dilute-spray regions of the flow.

The present phase of the investigation seeks to extend the results of Ruff & Faeth (1987) and Ruff et al. (1987, 1988). The objectives are to examine the effect of gas density on the effectiveness of the LHF approximation and to study separated-flow phenomena in the dense-spray region. Interest in higher gas densities follows since drop sizes become smaller for a given jet Reynolds number which should tend to improve the performance of LHF analysis (Bracco, 1983). However, higher gas densities reduce the density ratio of the flow which increases the rate of flow development and places greater stress on the LHF approximation (Mao et al., 1980, 1981). This issue can best be clarified by new measurements since current capabilities for computing spray breakup phenomena are very limited. Finally, measurements of the structure of dense sprays are clearly needed to sort out the topography and major structural features of the flow so that rational methods for treating separated-flow phenomena in dense sprays can be developed.

The study of effects of increased gas densities involves apparatus and measurements similar to the first phase of the study. This consists of a water jet injecting virtually downward in still air but within a pressure vessel to allow operation at varying ambient densities. Measurements include flow visualization using flash photography; and liquid volume fractions using gamma-ray absorption. Measurements are compared with analysis using the LHF approximation, similar to the first phase of the study.

The study of separated flow phenomena in dense sprays involves the use of the present atmospheric pressure apparatus. Measurements include liquid-phase topography and velocities using double-flash holography; and mean and fluctuating velocities in the gas phase and the all-liquid core using a phase-discriminating LDA.

This portion of the report begins with a description of experimental methods. Theoretical methods are then briefly described. This portion of the report concludes with a description of initial findings and a summary of the status of the work.

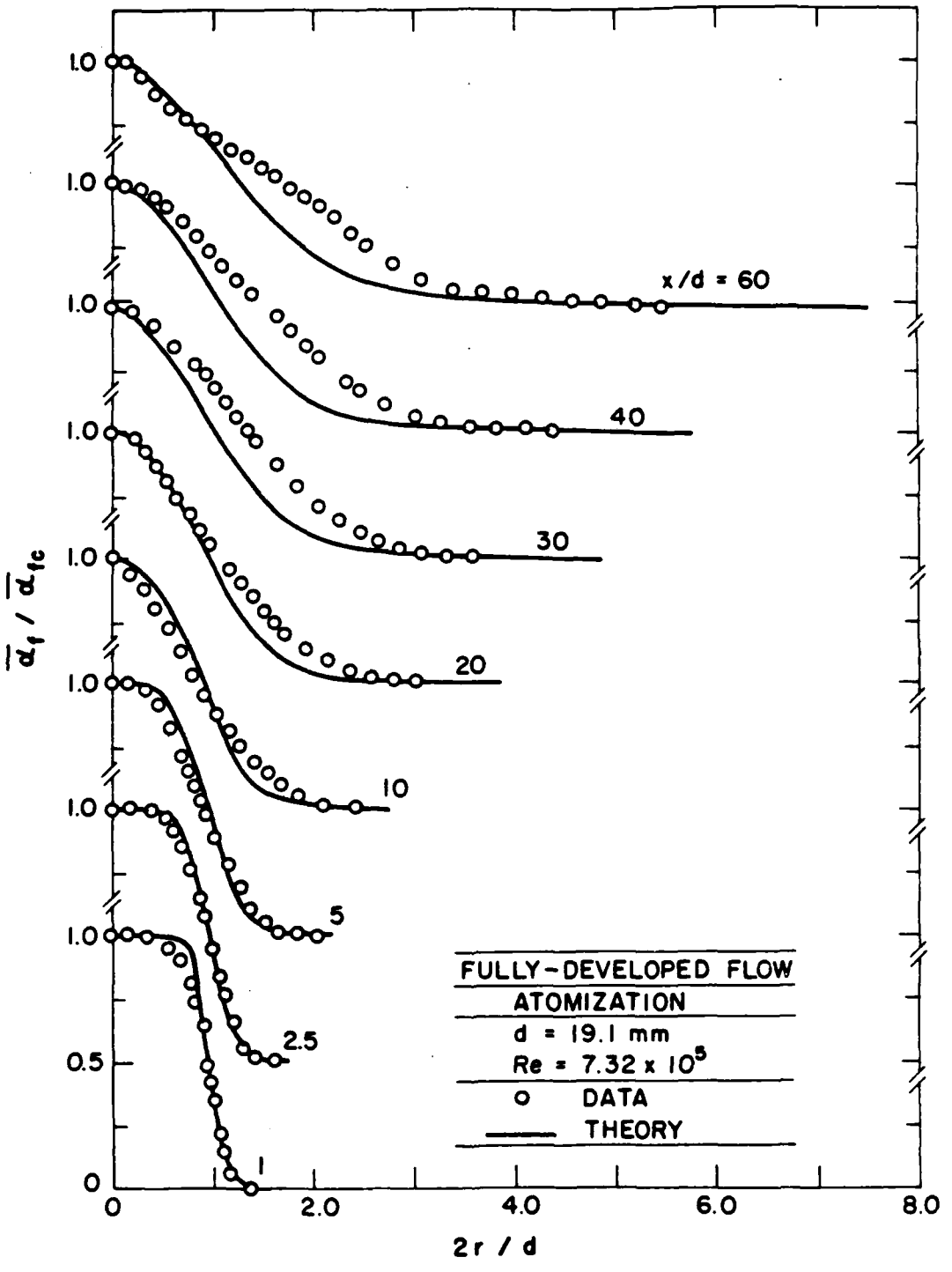

Figure 24 Time-averaged liquid volume fractions for atomization breakup and fully-developed flow.

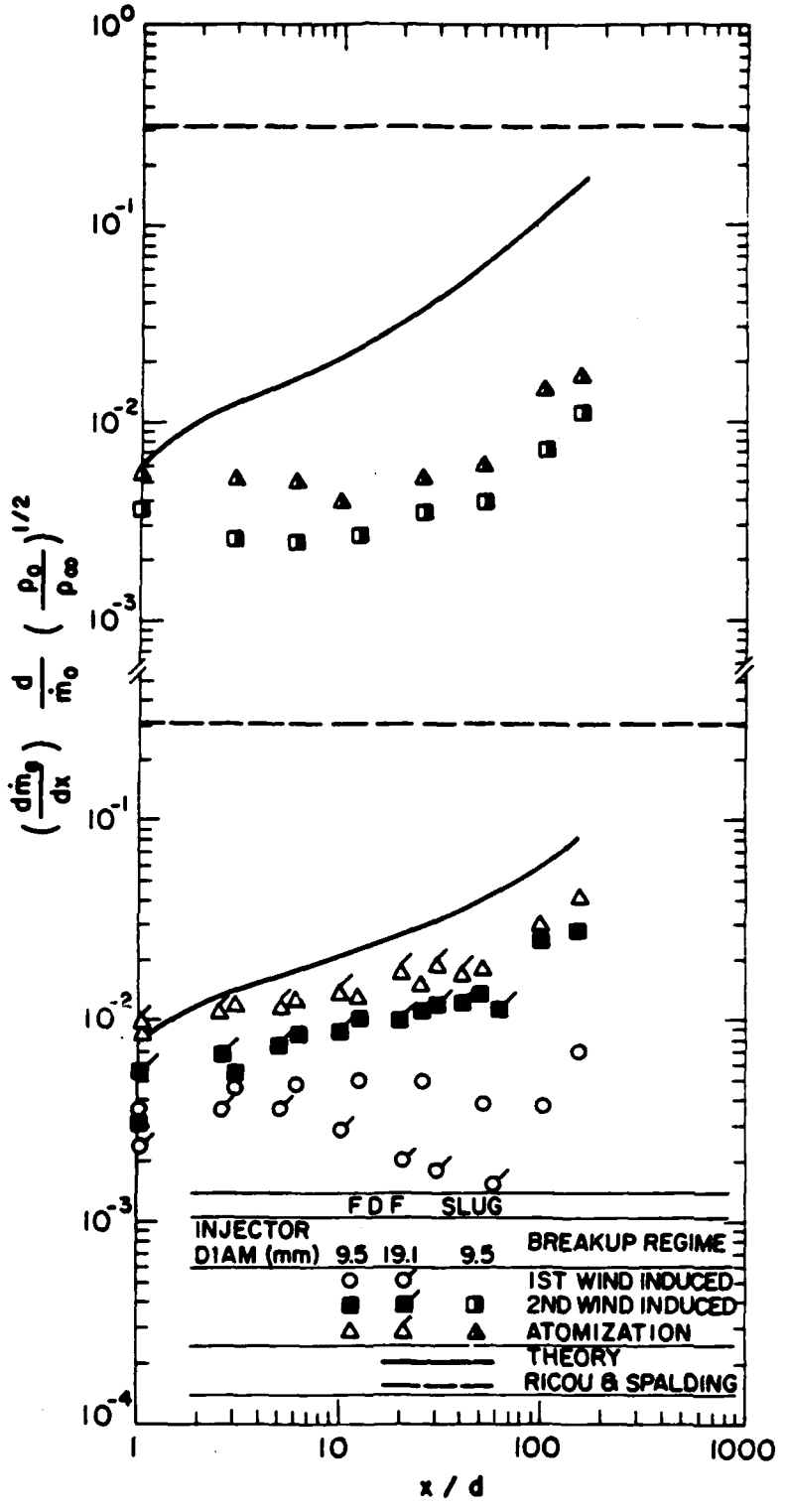

Figure 25 Entrainment rates along axis for fully-developed and slug flow.

3.2 Experimental Methods

3.2.1 Apparatus

Two test arrangements are being used for the dense-spray study: (1) an atmospheric-pressure apparatus used during the first phase of the study; and (2) a pressurized apparatus that is currently being developed. The current test arrangement is described in some detail by Ruff & Faeth (1987) and Ruff et al. (1987, 1988) and will be considered only briefly in the following.

Atmospheric Pressure Apparatus. Issues being studied relate to the dynamics of turbulent spray mixing processes, which are not thought to be strongly influenced by the injector diameter; therefore, large-scale (9.5 and 19.1 mm injector diameters) jets are used in order to get adequate spatial resolution for observations. The experimental arrangement is illustrated in Fig. 26. Water is used as the test liquid, injected vertically downward in still air. The water is collected in a tub at the downstream end of the spray and discharged to a drain. Baffles within the tube eliminate the splashing of liquid back up into the area where measurements are made. Water temperature is monitored with a submerged thermocouple.

City water is supplied to the injector using a centrifugal water pump (Pennsylvania Pump and Compressor Co., Type 2-1/2" 2-S OMSR). The rate of water flow is adjusted using a bypass system and measured with an Oilgear Co. PV meter (Type 15T TD2, Model PL15C-2A1S/UNO-25-0100-005-003) with a digital readout. The flow meter was calibrated by collecting water for timed intervals.

Instrumentation is mounted rigidly: therefore, the injector is traversed (1 m horizontally and 2 m vertically) to measure flow structure. The injector is mounted on a plate which traverses horizontally on a linear bearing assembly (25 mm diameter) whose position is adjusted by a Velmex, Inc. Unislide lead screw and stepping motor (Models B4036Q1J, M092-FD08 and 4-8311). The horizontal position is recorded using a Velmex, Inc. Digital Position Readout (4-8518), readable to 5 μm. The vertical traverse uses 25 mm diameter linear bearings as well, mounted on two I-beams which are attached at the ceiling and the floor. The vertical position is set with a cable and winch since only fixed axial stations are considered. The vertical position is measured with a ruler, accurate to 0.5 mm.

Three injectors are being used: a slug-flow injector having an exit diameter of 9.5 mm, and two fully-developed flow injectors having diameters of 9.5 and 19.1 mm. The slug-flow injector consists of a honeycomb flow straightener (1.6 mm cells, 25 mm long), two screens to calm the flow (0.018 mm diameter wire, 16 × 16 square mesh), followed by a smooth converging section from the 35 mm diameter water supply tube to the 9.5 mm exit diameter. The converging section provided a uniform exit flow, following a contour prescribed by Smith & Wang (1944). The fully-developed flow injectors have a flow straightener similar to the slug flow injector, followed by a simple circular converging section to a constant-area passage having a length of 41 passage diameters. Both arrangements provide no swirl at the jet exit, while minimizing problems of cavitation within the passage. Measurements at the injector exit showed that the designs provide the desired slug and fully-developed pipe flow exit conditions (Ruff et al., 1987, 1988).

Pressurized Apparatus. Figure 27 is a sketch of the pressurized liquid jet apparatus. The jet operates within a pressure vessel having a diameter of 1.5 m and a height of 4.5 m, capable of operation up to 10 atm. Similar to the atmospheric pressure

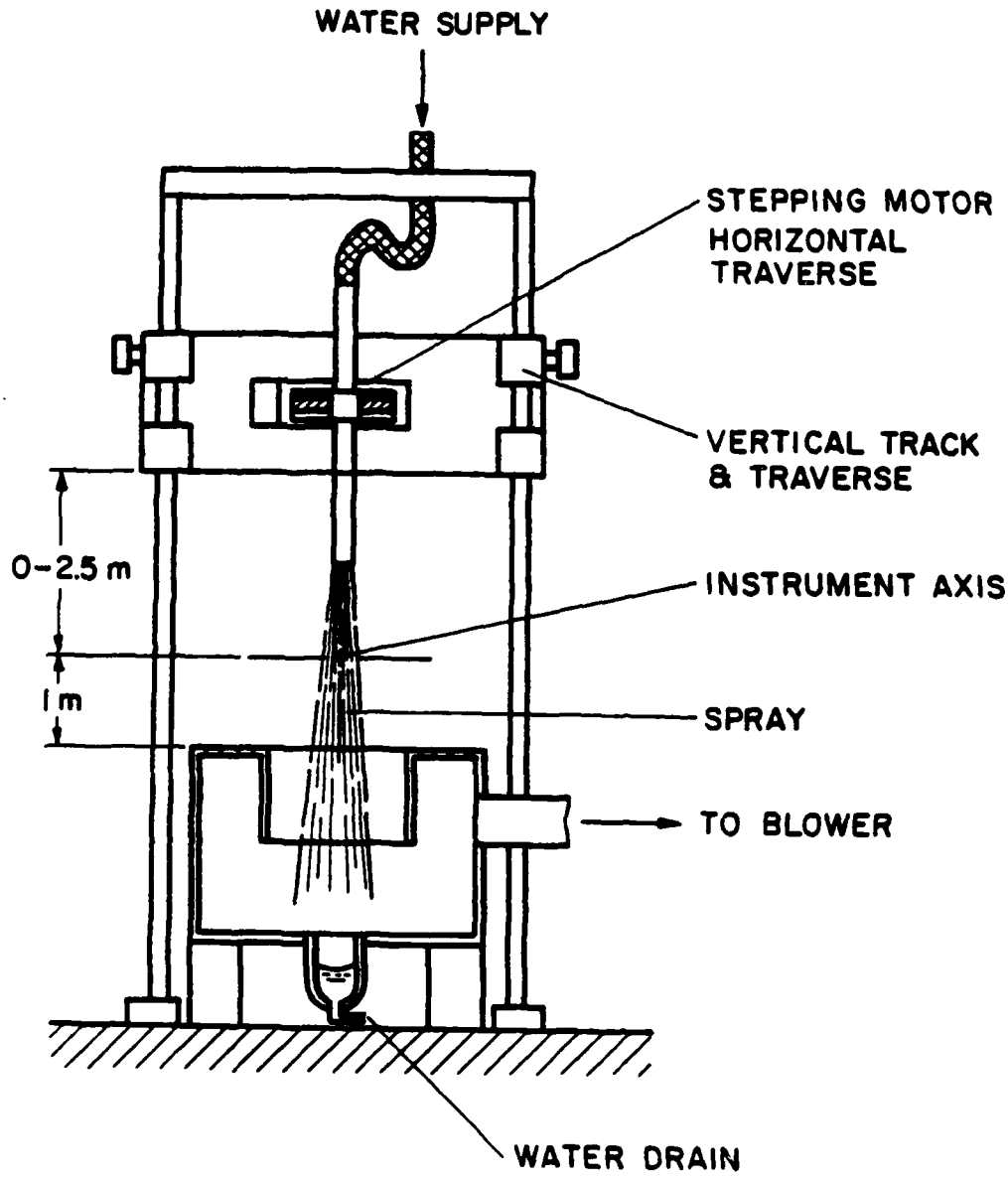

Figure 26 Sketch of the atmospheric-pressure test apparatus.

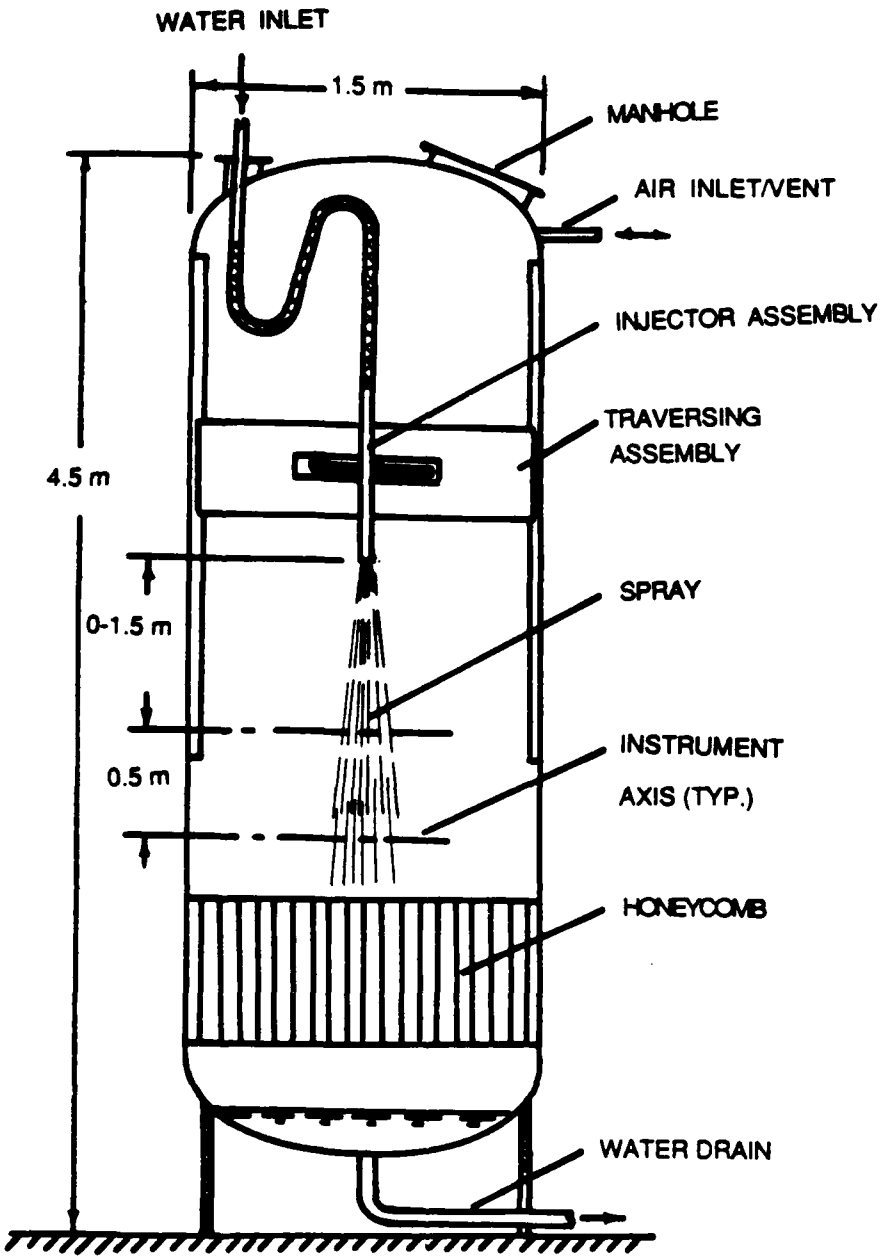

Figure 27 Sketch of the pressurized test apparatus.

arrangement, instrumentation is rigidly mounted, while the injector can be traversed vertically and horizontally to measure flow structure. The water jet is directed vertically downward using the same injectors as the atmospheric pressure investigation (since their flow properties have been characterized). Water is removed from a baffled region at the bottom of the tank and discarded. The present liquid pumping system is used for testing with both the atmospheric pressure and pressurized apparatus. The measuring plane of the apparatus is fitted with a number of instrumentation ports, while a manhole at the top provides access for assembling the injector and changing its axial position. Radial traversing, is stepping-motor driven, similar to the atmospheric pressure arrangement.

3.2.2 Instrumentation

Flow Visualization. Measurements include flow visualization, using flash photography; liquid volume fraction distributions, using gamma-ray absorption; liquid core velocities using an LDA; gas velocities in the drop-containing shear layer, using a phase-discriminating LDA; and liquid-phase topography and velocities in the drop-containing shear layer using double-flash holography.

Flash photography is based on a Xenon Corporation High-Intensity Micropulse System (Model 457A) which can provide a 10 J light pulse with a 1 μs duration. These photographs are obtained in a darkened room using an open camera shutter, with the flash lamp controlling the time of exposure. The photographs are taken with a 4 × 5 Speed Graphic camera using Polaroid Type 57, 3000 ASA black and white film. The camera is directed normal to the spray axis, from a position near the flash lamp. The jets are quite long; therefore, they are photographed in sections, each roughly 250 mm long, in order to adequately resolve the flow. The window arrangement in the pressurized apparatus facilitates flash photography in the same manner as the atmospheric-pressure apparatus.

Gamma-Ray Absorption. The general design of the gamma-ray absorption system follows Gomi and Hasegawa (1984), Ohba (1979) and Schrock (1969). An Iodine 125 isotope source (2 mCi, emitting primarily at 27.47 keV) provides a soft gamma-ray source yielding optimum absorption levels in order to minimize experimental uncertainties for the absorption measurements. The source is placed in a lead casket with a 1.6 mm diameter × 13 mm long collimating aperture. The front of the casket is fitted with a 12 mm thick removable lead shield to cover the source during periods when it is not in use. Gamma rays passing through the flow are detected and counted using a Bicron Model 1 × M.040/1.54 X-ray probe. A lead aperture (1.5-6 mm in diameter, depending on position, and 12 mm long) is placed in front of the detector to define the path observed through the flow. The detection system of the pressurized apparatus is at room conditions with the gamma-rays passing out of the chamber through a metal foil window. The data acquisition system uses an EG&G Ortec single-channel analyzer and counter/timer (Models 556, 590A, 970). The energy window of the analyzer is centered at 27.5 keV to minimize spurious counts due to background radiation and Compton scattering (the latter effect is not large, however, in the present energy range). Detector output is stored and processed using an IBM AT personal computer.

Absorption measurements are made for 30-60 parallel paths through the flow. These measurements are very symmetric; therefore, measurements on both sides of the axis are averaged and smoothed to provide a single set of absorption measurements for a given cross-section of the flow. The line-of-sight measurements are deconvoluted, following Santoro et al. (1981), to yield radial distributions of void fraction. Schrock (1969) and Gomi and Hasegawa (1984) point out that this method has a fundamental uncertainty

depending on whether parallel or normal liquid laminae are assumed. However, the narrow absorption paths used during the present experiments reduced this effect to less than 5 percent.

The gamma-ray absorption system is calibrated using water-filled cells to measure the linear absorption coefficient. Data involves 30-60 absorption measurements (varying with the width of the flow) and ca. 25,000 counts at each position. Richardson extrapolation of these results to their limits indicated experimental uncertainties of centerline void fraction less than 5 percent, with proportionately higher values elsewhere.

Laser-Doppler Anemometry. Gas-phase properties of the drop-containing shear layer are measured using a phase-discriminating LDA similar to the arrangement described in Section 2.2.2. With this method, proper LDA signals, from ca. 1 μm diameter seeding particles, are identified by their signal amplitude — rejecting large-amplitude signals from drops and other liquid elements. Grazing collisions of large liquid elements with the optical probe volume yield small amplitude signals which also can be mistaken for seeding particles and proper-sized drops; therefore, these signals are rejected using an outer measuring volume which detects all large amplitude signals from large drops and other large liquid elements in the vicinity of the optical measuring volume. Signal processing is similar to current work with homogeneous particle-laden flows, heavily seeding the air in the test cell with bay oil drops so that high signal rates can be obtained. This allows direct measurements of unbiased time averaged mean and fluctuating velocities, and other turbulence properties, without the use of questionable velocity bias corrections.

Turbulence properties of the all-liquid core are measured with the LDA using an on-axis forward-scatter arrangement with light guides to allow observations through the drop-containing shear layer. A 3.75 X-beam expander is used to minimize the size of the measuring volume and improve signal-to-noise ratios.

Holography. Since the topography of liquid elements in dense sprays is variable, direct photography provides the only reliable approach for measuring dispersed-phase properties. Combined requirements of high magnification, reasonable depth of field, and analysis of non-planar motion can best be satisfied by double-flash holography which is the approach being used during the present investigation.

The holocamera system is illustrated in Fig. 28. This is an off-axis holograph arrangement based on the Spectron Development Laboratories Model HTRC-5000 system but substantially modified to provide holographs of dense sprays. In particular, dense sprays require large light intensities, so that the flow can be penetrated, and high magnification, since small drops are of interest. This is accomplished by using a narrow-diameter high-intensity laser beam through the spray, which is subsequently expanded to the same size as the reference beam when these two optical signals are mixed to form the hologram. A ruby laser provides the light source, depositing 50 mJ in roughly 20 ns. The system can be double pulsed, yielding two holographs on the same film. This type of hologram can be reconstructed to show the object field at two instants of time, providing a means of measuring the velocities of objects.

The holograph carries light amplitude and phase information which yields a three-dimensional image of the object upon reconstruction. This image can be projected indefinitely; therefore, it can be scanned by any convenient technique to measure flow properties. The reconstruction system is illustrated in Fig. 29. The beam from a 15 mW cw HeNe laser is expanded and then passed through the developed holograph plate. The off-axis configuration shown in Fig. 28 provides a real magnified image of the spray in the

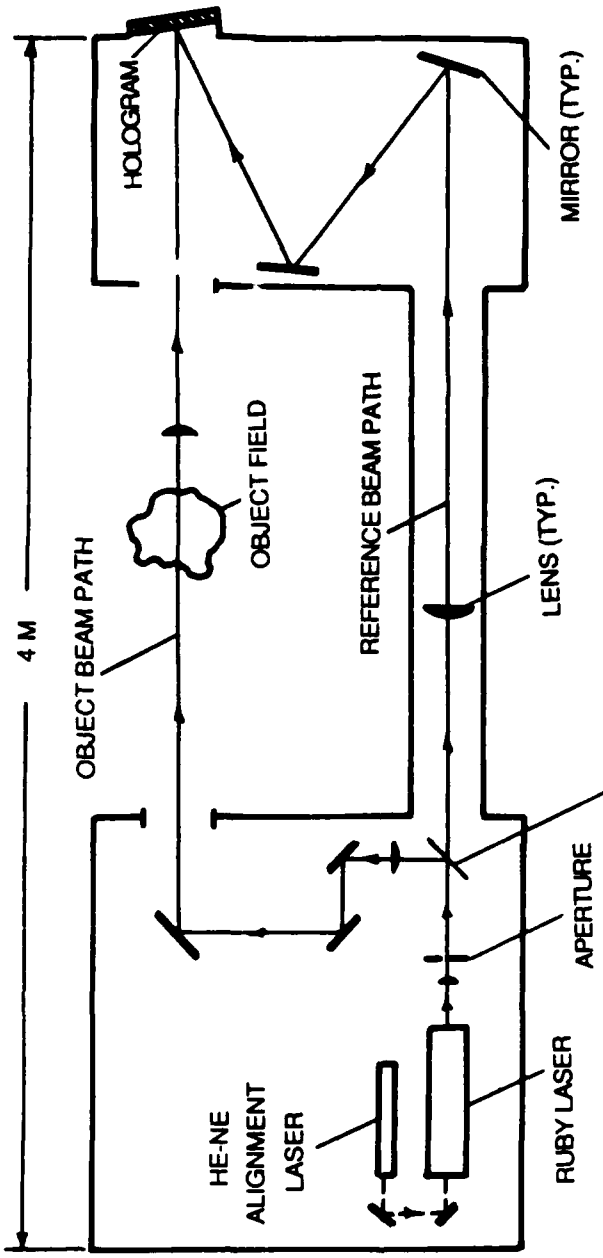

Figure 28 Sketch of the double-pulse holocamera system.

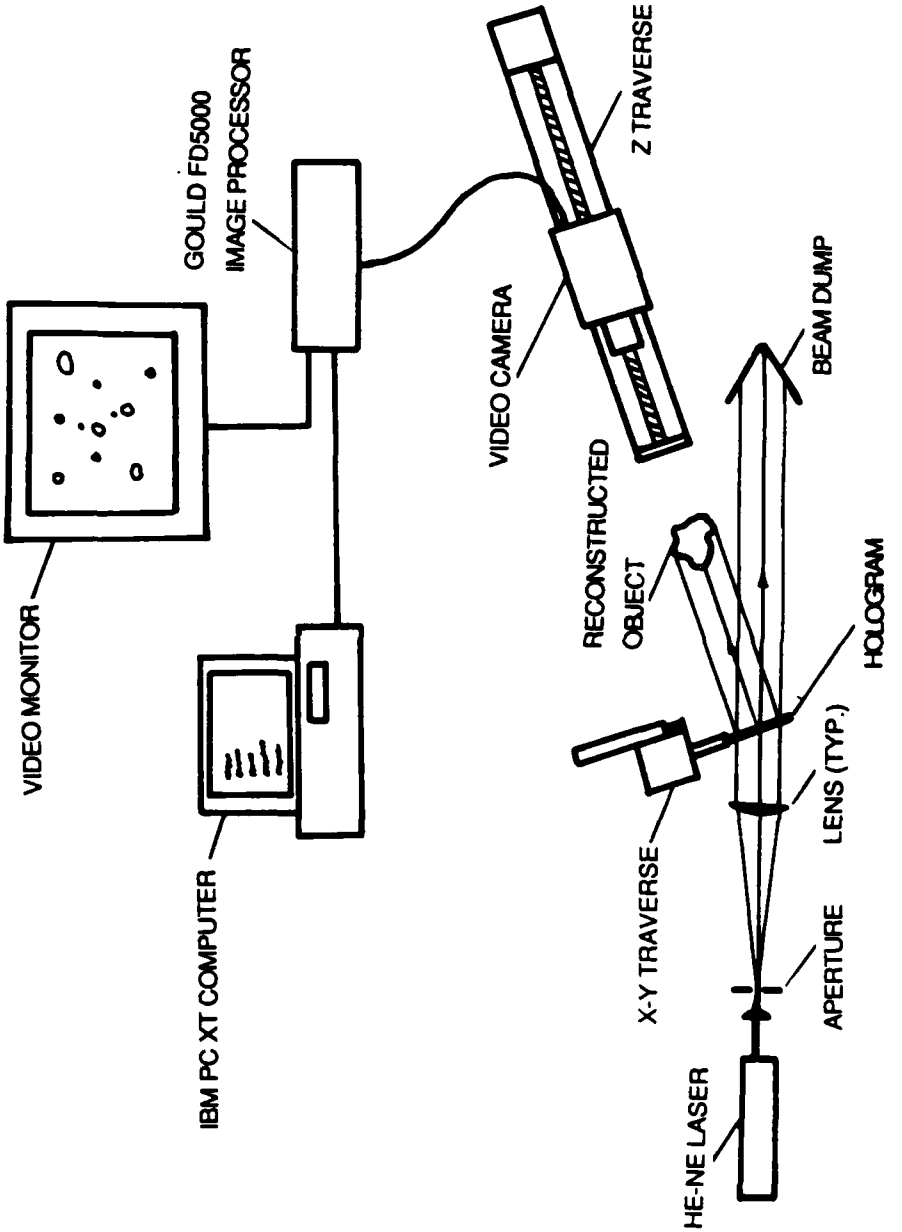

Figure 29 Sketch of the hologram reconstruction system.

region in front of the hologram. The properties of this region are measured with a video camera having a high magnification and a short depth of field, to reduce problems of optical noise due to out-of-focus drops. Computer-controlled x-y traversing of the holograph and z traversing of the video camera allow the region crossed by the object beam to be studied. Data is reduced using a Gould FD5000 Image Processing System. Operation of the image processing system is only semi-automated so that human interaction is required at present; nevertheless, ca. 100-200 objects can easily be analyzed in a hour, which is adequate for present purposes.

3.2.3 Test Conditions

Test conditions for the atmospheric pressure tests are the same as Ruff & Faeth (1987) and Ruff et al. (1987, 1988). These test conditions are summarized in Table 4. Three test conditions have been defined for each injector corresponding to first and second wind-induced breakup, and atomization breakup, according to criteria of Miesse (1955), Ranz (1958) and Reitz (1978).

Test conditions for the pressurized apparatus will involve the same liquid flow rates and injectors as those given in Table 4. Test chamber pressures will be in the range 0.1-1.0 MPa with a corresponding increase in gas density. These pressure increases will tend to move operating conditions toward, or farther into, the atomization breakup regime.

3.3 Theoretical Methods

Analysis of dense sprays is limited to the LHF approach, since applicability of LHF methods in this region is one of the main theoretical issues of the investigation. The main features of the LHF analysis are similar to past work on multiphase jets and sprays in this laboratory (Shuen et al., 1983, 1985, 1986; Solomon et al., 1985, 1985a, 1985b; Sun & Faeth, 1986, 1986a,; and Sun et al., 1986). The approach is fully described by Ruff & Faeth (1987) and Ruff et al. (1987, 1988) and will be only briefly discussed here.

The LHF approximation implies that both phases have the same velocity and are in thermodynamic equilibrium at each point of the flow. Thus, the flow corresponds to a variable-density single-phase flow, due to changes in the concentrations of the phases, even through the density of each phase is constant. The analysis is limited to a steady (in the mean), two-phase, round turbulent isothermal jet. Specific conditions involve the injection of pure water vertically downward into still air. Flow velocities are relatively small; therefore, kinetic energy and viscous dissipation of the mean flow were neglected with little error. Effects of buoyancy are considered in the governing equations for mean quantities, since the density of the flow varies (buoyancy forces become important near the edge of the flow and far from the injector, where flow velocities are small). Similar to past work, however, effects of buoyancy are not considered in the governing equations for turbulence quantities (Shuen et al., 1983, 1985, 1986; Solomon et al., 1985, 1985a, 1985b; Sun & Faeth, 1986, 1986a; and Sun et al., 1986). Since the present flows spread similar to single-phase jets, the boundary layer approximations are used. Following Lockwood & Naguib (1975) and Bilger (1976), among others, the exchange coefficients of both phases are assumed to be the same. This assumption can be problematical in regions where molecular transport is important, since molecular diffusion of finite-sized elements (bubbles, drops, etc.) is small (Faeth, 1977, 1983, 1987). However, laminar exchange is not important for the high Reynolds numbers of interest here, cf. Table 4; therefore, this approximation can also be adopted with little error.

Table 4 Summary of Liquid Jet Test Conditions at Atmospheric Pressure[a]

Exit Diameter (mm)	Inector Pressure Drop (kPa)	Flow Rate (kg/s)	Re_f × 10^{-5}	We_g	Oh × 10^4	Breakup Regime
	80	0.39	0.52	4.6	12.1	1st Wind-Induced
9.5[b]	420	1.55	2.07	72.9	12.1	2nd Wind-Induced
	2520	3.99	5.34	492.8	12.1	Atomization
	30	1.32	0.88	6.6	8.6	1st Wind-Induced
19.1[c]	360	4.50	3.00	76.7	8.6	2nd Wind-Induced
	2070	11.00	7.32	458.6	8.6	Atomization

[a]Pressure-atomized water injected vertically downward into still air at 98.8 kPa.
[b]Both slug flow and fully-developed pipe flow initial conditions.
[c]Only fully-developed pipe flow initial condition.

Under present assumptions, all scalar properties are only a function of mixture fraction, which is the fraction of mass at a point which originated from the injector. Thus, the conserved-scalar formalism can be used, similar to an early proposal by Lockwood & Naguib (1975), but modified to use mass-weighted or Favre-averaged quantities, following Bilger (1976). The governing equations involve conservation of mass, streamwise mean momentum, and mean mixture fraction; and modeled governing equations for turbulence kinetic energy, the rate of dissipation of turbulence kinetic energy, and mean-squared mixture-fraction fluctuations. Methods used follow the specific formulation and empirical constants of Jeng & Faeth (1984), which have been calibrated using a variety of constant- and variable-density single-phase round jets. The formulation and constants, however, are not very different from the early proposal of Lockwood & Naguib (1975). Scalar properties are only a function of mixture fraction called state relationships. State relationships can be found by straightforward thermodynamic equilibrium computations. The complete formulation, the state relationships, and the details of the numerical calculations are described by Ruff et al. (1987, 1988).

3.4 Results and Discussion

3.4.1 Flow Observations

Testing thus far has been limited to the atmospheric pressure apparatus. The primary objective has been to develop the holocamera and reconstruction systems and to develop methods for data analysis. This work has also provided useful information concerning the structure of dense sprays, however, which will be discussed in the following. Results are limited to fully-developed jet exit conditions in the atomization breakup regime using the 9.5 mm diameter injector.

Typical hologram reconstructions are illustrated in Figs. 30-35. These photographs were taken from the video monitor of the image analysis system. Figures 30-32 were obtained at $x/d = 12.5$ and $r/x = 0.075$, 0.10 and 0.15, while Figs. 33-35 were obtained at $x/d = 25$ and $r/x = 0.05$, 0.10 and 0.15. The radial positions correspond to points near the contiguous liquid core, near the middle of the drop-containing mixing layer, and near the outer edge of the drop-containing mixing layer. All photographs were obtained with the same magnification yielding a field of view of 1725×2250 μm, and are from single-pulse holograms. The present system can provide much higher levels of magnification so that 5 μm diameter drops can be resolved: these pictures were obtained with a relatively low magnification so that the character of the flow can be seen. Except near the liquid surface, usually only one drop or liquid element (or a portion of it) is in focus for any one screen image of the video monitor. Thus, the photographs have a mottled appearance due to out-of-focus drops. Furthermore, the images on the monitor are much easier to interpret — particularly since the focal plane can be easily moved to sharpen the focus on any one drop.

Conditions near the outer edge of the drop-containing mixing layer, Figs. 32 and 35, correspond to a dilute spray: the drops are generally relatively small and spherical and the liquid volume fraction is small so that the drops are spaced quite far from one another. Moving to the middle of the drop-containing mixing layer, Figs. 31 and 34, the flow largely remains a dilute spray although drop number densities and drop diameters are generally larger. In this region, however, some of the larger liquid elements are no longer spherical: this is most evident at $x/d = 12.5$, see Fig. 31. Finally, at the edge of the contiguous liquid core, Figs. 30 and 33, liquid elements become quite large and are very irregular in shape, consisting of oblong ellipsoids and ligaments surrounded by only a few spherical drops. On these figures, the lower right hand corners of the photographs actually

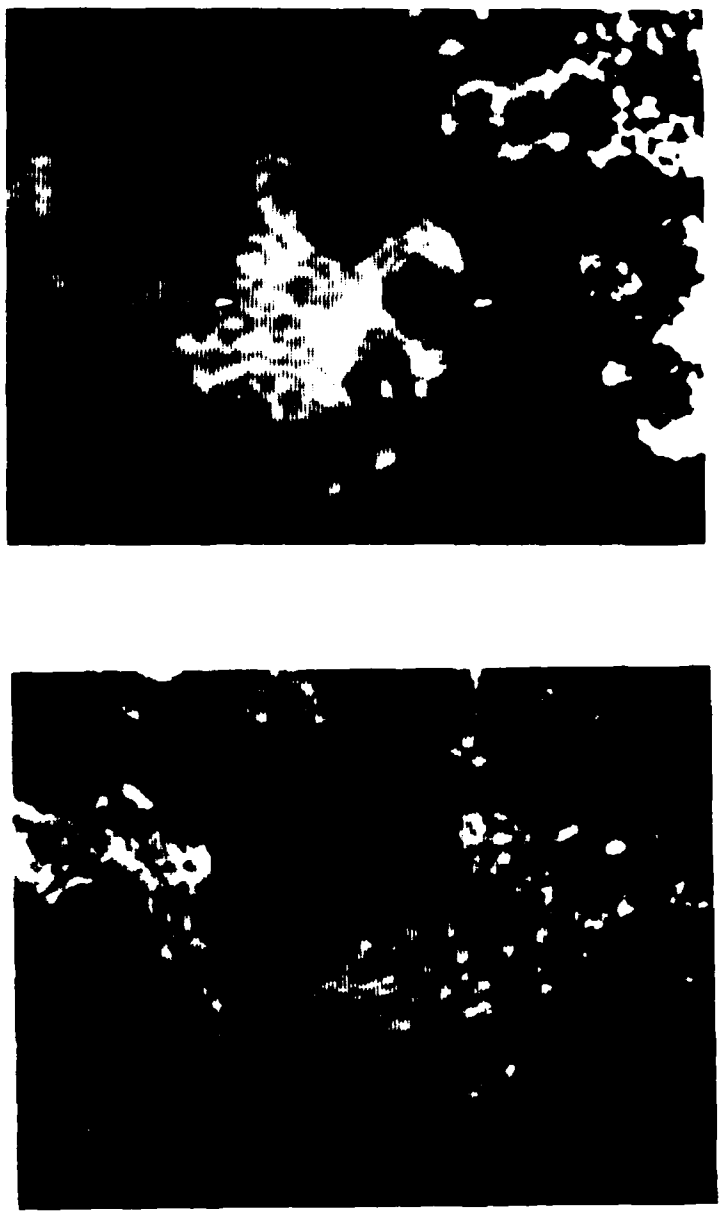

Figure 30 Typical hologram reconstruction in the dense-spray region ($x/d = 12.5$, $r/x \approx 0.075$).

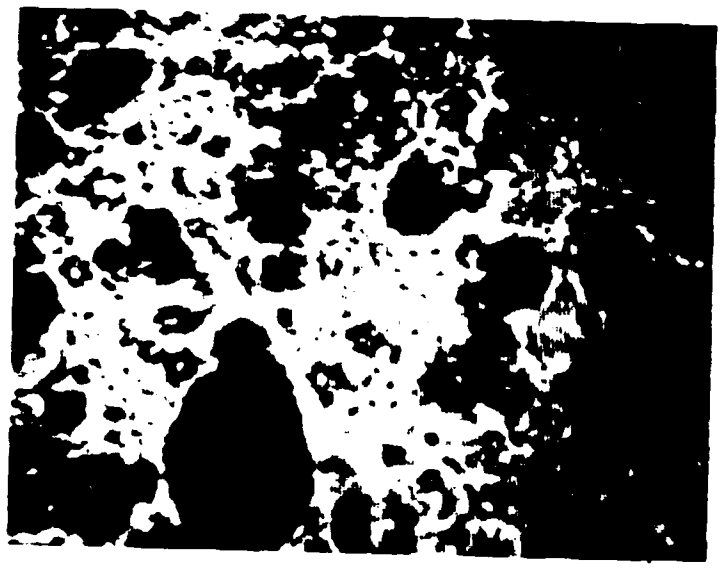

Figure 31 Typical hologram reconstruction in the dense-spray region ($x/d = 12.5$, $r/x = 0.10$).

Figure 32 Typical hologram reconstruction in the dense-spray region (x/d = 12.5, r/x = 0.15).

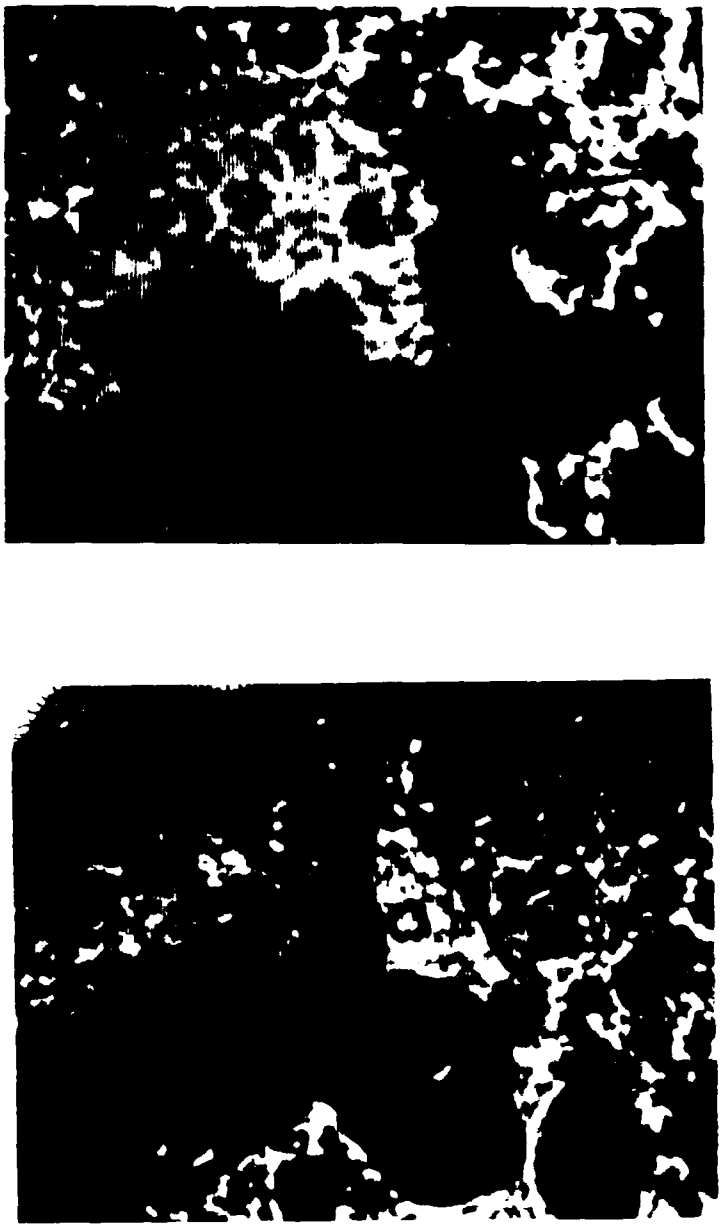

Figure 33 Typical hologram reconstructions in the dense-spray region ($x/d = 25$, $r/x = 0.05$).

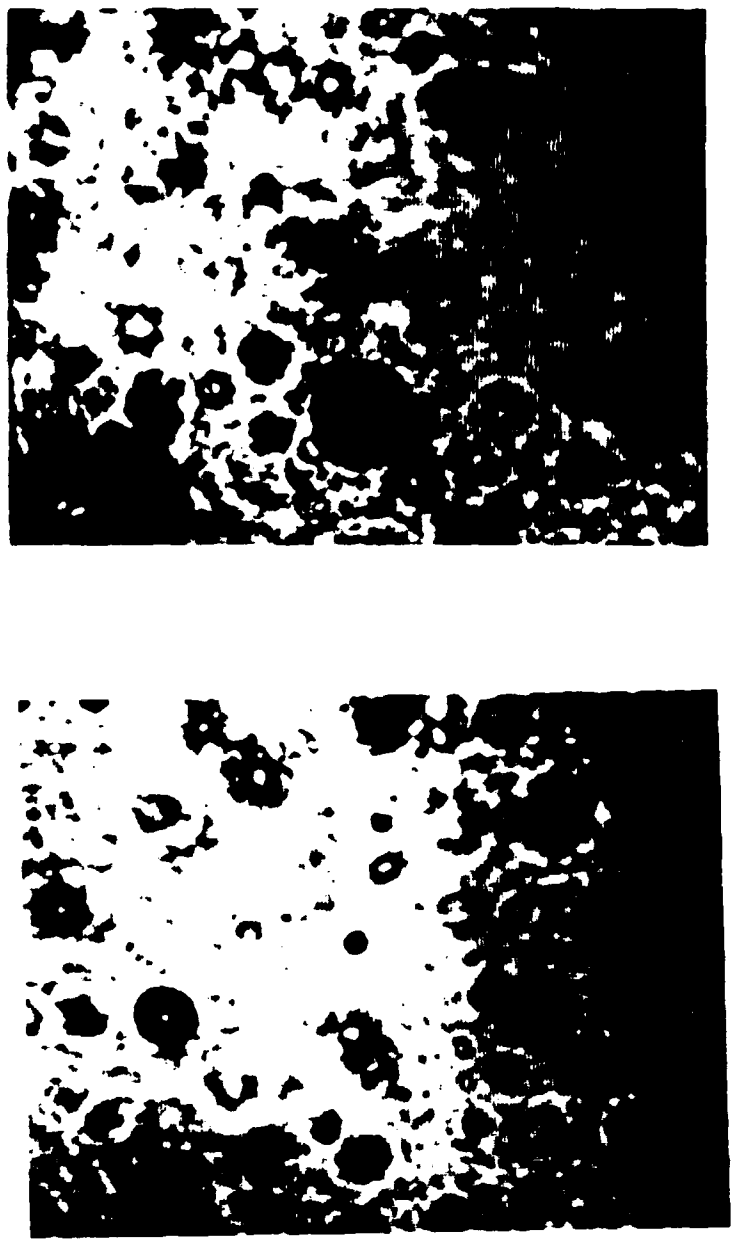

Figure 34 Typical hologram reconstructions in the dense-spray region (x/d = 25, r/x = 0.10).

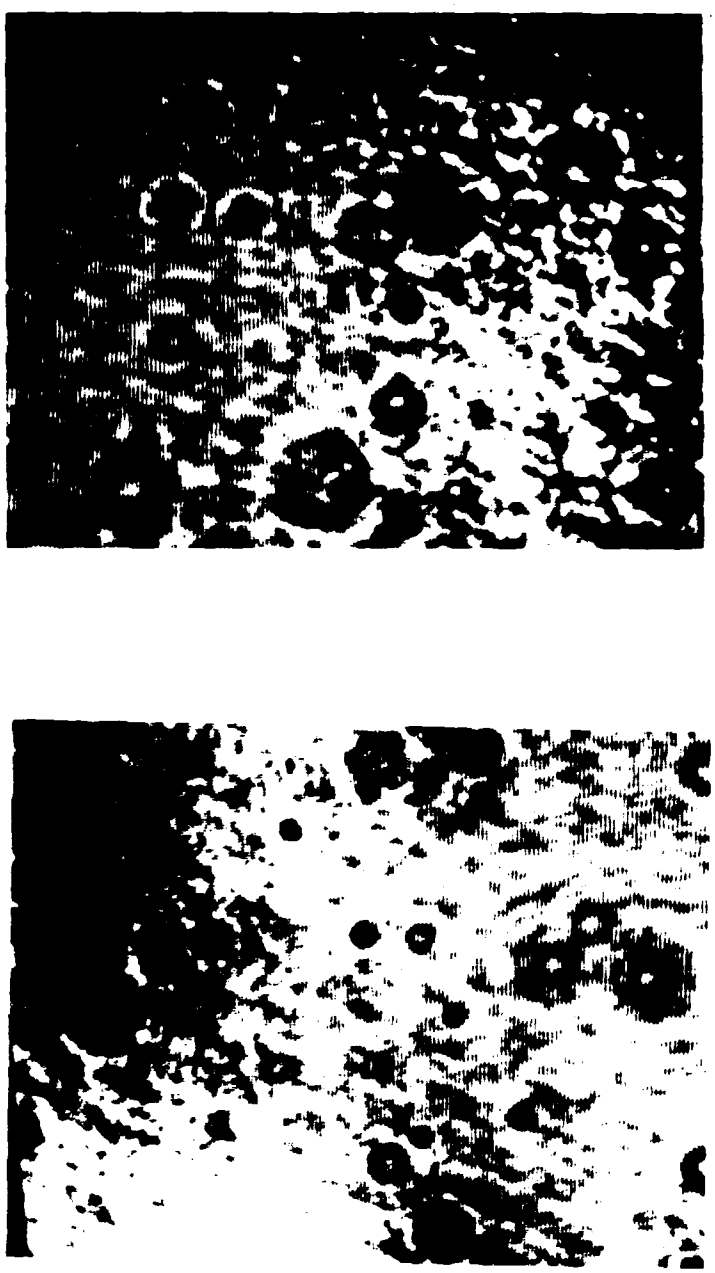

Figure 35 Typical hologram reconstructions in the dense-spray region ($x/d = 25$, $r/x = 0.15$).

correspond to a section of the surface of the continuous liquid core which corresponds to another type of liquid element present in the dense-spray region. A surprising feature of the region near the liquid core, however, is that the gas-containing portion is relatively dilute at each instant. Even high magnification reconstructions of this region did not reveal large numbers of small drops. Thus, the main difference between the dilute and dense regions of the spray is that the dense regions involve large and irregular liquid elements that cause the liquid volume fraction to be large even though the actual gas-containing region is relatively dilute.

The picture that emerges from the reconstructions illustrated in Figs. 30-35 is quite different from earlier hypotheses concerning dense spray structure that have appeared in the literature (Bracco, 1983; Reitz, 1978; Reitz & Bracco, 1982, 1984; Reitz & Diwakar, 1987). Earlier work postulated that very small drops were either formed at the jet exit or were stripped from the surface of the contiguous liquid core and formed larger drops within the drop-containing mixing layer by collisions and coalescence. Aside from the fact that this is a rather implausible way to form large drops from a single liquid element in a rapidly developing flow, it certainly does not conform with the observations of large irregular liquid elements near the liquid surface evolving to smaller round drops near the edge of the flow with a relatively dilute gas-containing flow field throughout.

A picture that is more consistent with the observations of Figs. 30-35 places greater emphasis on the mechanism of liquid element or drop shattering. The presence of a multiphase mixing layer tends to make velocities in the mixing layer more uniform than a single-phase mixing layer since momentum exchange between the phases is dispersed. This reduces velocity gradients near the surface, favoring the formation of relatively large liquid elements like ligaments. As the flow develops, the ligaments move into slower-moving gas nearer the edge of the flow and become unstable: breaking up into smaller liquid elements that have a more spherical shape due to greater effects of surface tension as the surface-to-volume ratio of the liquid elements increases. Larger drops subsequently become unstable as they pass through slower-moving gas near the edge of the flow and break up into smaller drops. The smaller drops adjust more rapidly to local gas velocities; the resulting reduced relative velocities and larger relative effects of surface tension finally end breakup processes. Thus, dense sprays do not correspond to nearly packed beds of closely spaced spherical elements dominated by collision processes and adjacent particles on interphase transport rates; instead, they correspond to a relatively dilute flow of irregularly shaped liquid elements dominated by breakup processes with adjacent particles having relatively little effect on interphase transport rates. Present work has also shown that the dense spray region is optically accessible with high resolution holography. Finally, although the edge region of the drop-containing mixing layer is dominated by spherical drops, most of the drop-containing mixing layer contains irregular liquid elements ranging from elongated ellipsoids to ligaments to the contiguous liquid core itself. In this circumstance, use of instruments like Fraunhofer diffraction for drop size distributions, and phase-Doppler anemometry for drop sizes and velocities, is inappropriate.

3.4.2 Flow Structure

At the present time, data accumulation is fragmentary since developing and checking methods of data processing from the holographic reconstructions have been emphasized. Preliminary information at x/d = 25 will be discussed in the following although additional measurements must be made to assess these results and to develop repeatable statistically-significant results.

A measure of the irregularity of the liquid elements in the drop-containing mixing layer at x/d = 25 is illustrated in Fig. 36. The ellipticity ratio, defined as the number-averaged ratio of the major to minor diameter of the liquid elements, is plotted as a function of r/x. The measurements extend from near the contiguous liquid core, r/x = 0.05, to near the edge of the drop-containing region, r/x = 0.15. The measurements are confined to dispersed liquid elements, i.e., the contiguous liquid core itself has not been considered.

Results near the liquid core in Fig. 36 indicate the large ellipticity of irregular liquid elements in this region, approaching 1.5. Interpretation of this number, however, is somewhat biased since a small round drop is given the same weight as a massive elongated liquid element: volume-averaged ellipticities, which would be more representative of the transport capacity of the liquid, are much larger. Moving away from the liquid surface, the ellipticity ratio decreases toward unity, reaching values near unity (on a number-averaged basis) about half-way across the layer. Values near the edge remain above unity but this is largely due to experimental errors. In the outer region, drops become generally quite small with many having diameters less than 20 μm. Under these circumstances, a difference of one pixel of the reconstruction camera becomes a greater percentage of the drop diameter yielding ellipticities greater than the actual value due to discretization errors. This effect will be corrected during subsequent work. Overall, however, the results of Fig. 36 help quantify effects of liquid element irregularity over at least the inner half of the drop-containing mixing layer.

The variation of Sauter mean diameter (SMD) in the drop-containing mixing layer at x/d = 20 is illustrated in Fig. 37. These data were obtained only considering discrete drops with ellipticities generally less than 1.5: this ignores elongated ligament structures that are prevalent near the surface at r/x = 0.05. For $r/x \geq 0.075$, where ligaments are only present to a modest degree the SMD decreases continuously with increasing radial distance. Two effects are probably responsible for this trend: the tendency of large drops to shatter as they encounter low velocity gas near the edge of the flow, and increased turbulent dispersion of small drops. The drops present near the liquid surface (r/x = 0.05) are relatively small and are probably present as remnants of ligament shattering processes and turbulent dispersion from regions farther out in the drop-containing mixing layer. If the SMD at this position included ligaments, however, it would be significantly greater than 300 μm.

Distributions of drop velocities at x/d = 25 are illustrated in Fig. 38. This information is based on relatively few data, 15-20 drops, due to problems of reliably locating drop pairs from double-flash holograms. Additional holograms will be required to obtain statistically-significant drop velocities. The largest drops tend to have velocities near the liquid injection velocity, ca. 60 m/s, and their velocities decrease with increasing distance from the surface. This is expected since large drops relax relatively slowly to local conditions while larger drops farther out in the mixing layer probably emanated from positions farther upstream so that drag has reduced their velocity to a greater extent. Due to their greater response, smaller drops accommodate to local gas velocities more readily and drop velocities progressively decrease with decreasing size. A surprising feature of the results in Fig. 38, however, is that velocities for each size class are relatively constant across the mixing layer (except for an outlying point for 50 μm diameter drops which may be the result of recently shattered large drops and limited velocity statistics). One would expect that gas velocities would increase as the surface is approached tending to cause the velocities of all drop sizes to increase as well — like the 150 μm diameter drops. It will be interesting to see if this trend holds as velocity statistics are improved by additional measurements.

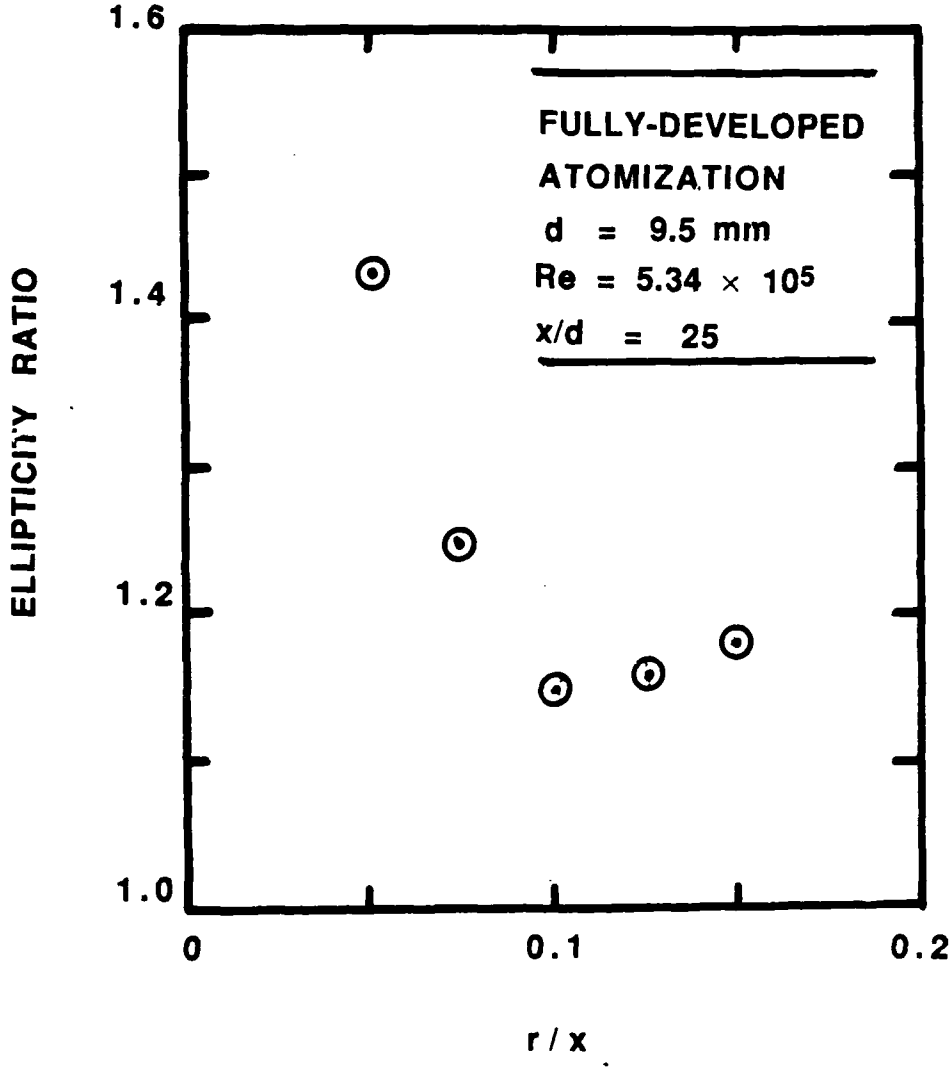

Figure 36 Radial variation of ellipticity ratio (x/d = 25).

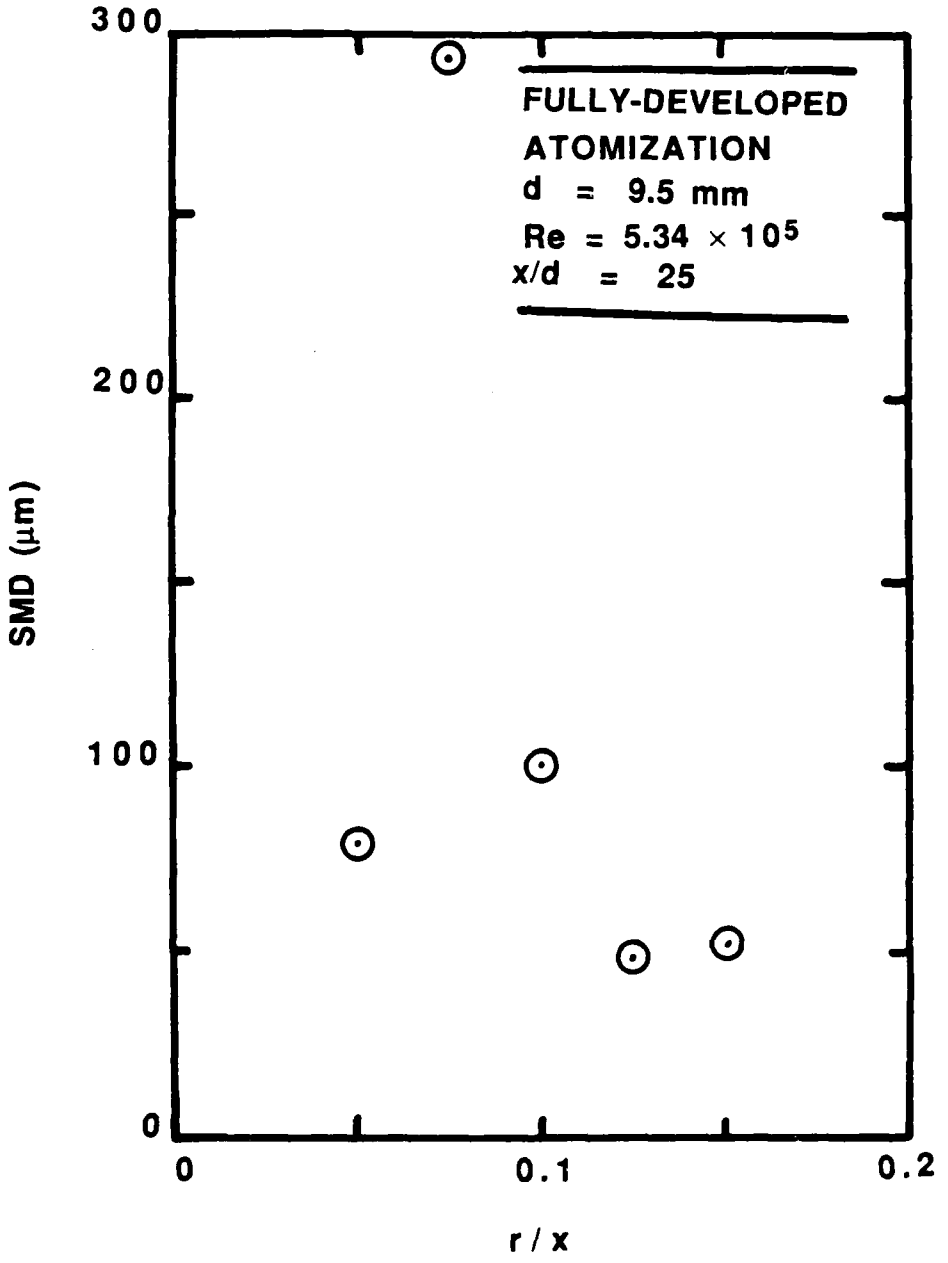

Figure 37 Radial variation of Sauter mean diameter (x/d = 25).

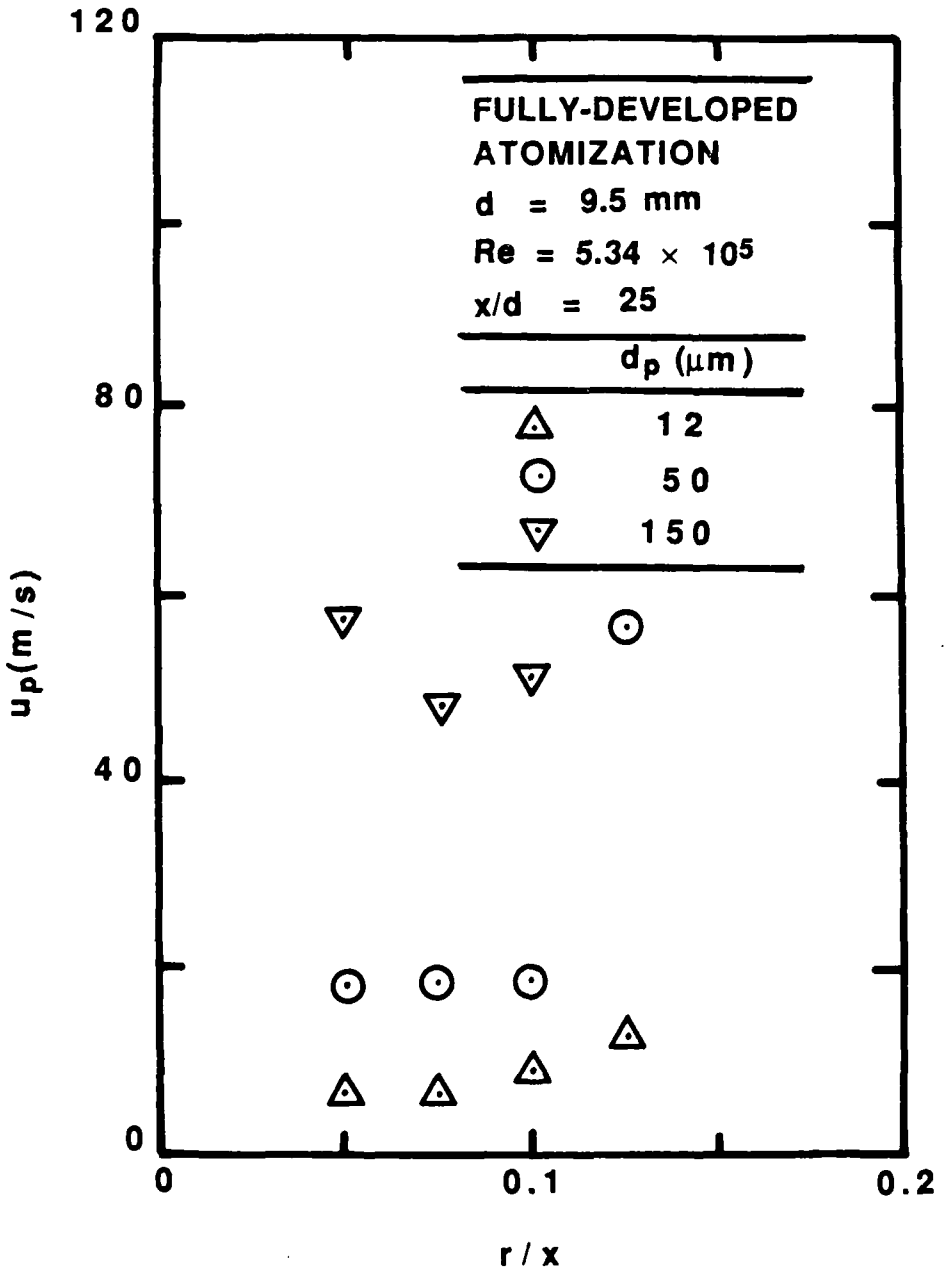

Figure 38 Radial variation of mean streamwise drop velocities (x/d = 25).

In spite of current limitations of velocity data, however, the results of Fig. 38 show that drops in the mixing layer are moving with vastly different velocities. This is unequivocal evidence of the importance of separated-flow effects. This suggests that the LHF approach is effective near the jet exit since the momentum defects of the gas phase and small drops are irrelevant, not that these defects are small! This argument is quite plausible. We have seen from results illustrated in Figs. 23 and 24 that the LHF approach is effective for atomization breakup if $\bar{\alpha}_f > 0.2$. Due to the large density ratio of the present flow (roughly 840), however, this region corresponds to mixture fractions greater than 0.99. Thus the contribution of the gas and smaller drops to the dynamics of the system is quite small in the region where use of the LHF approximation has been shown to be effective. In the dilute spray region, however, both phases contribute significantly to flow properties and the deficiencies of the LHF approximation become more apparent. Since practical sprays have much smaller injectors than the present flows, yielding higher rates of deceleration, separated-flow effects should be even more significant. Moving to higher Reynolds numbers and higher ambient densities, which tends to reduce stable drop sizes, should tend to improve predictions using the LHF approximation but the extent of the improvement must still be resolved.

3.5 Summary

Results from the first phase of this study have been reported by Ruff et al. (1987, 1988). This involved measurements of liquid volume fraction distributions and entrainment rates for pressure atomized water sprays injected vertically downward in still air at atmospheric pressure. Spray conditions included first wind-induced, second wind-induced, and atomization breakup with both fully-developed and slug flow conditions at the jet exit. The measurements were used to evaluate the effectiveness of the LHF approximation of multiphase flow theory.

The results of the first phase of the study showed that spray structure and mixing rates were sensitive to the breakup regime and the state of flow development at the jet exit. Atomization breakup and fully-developed flow yield the fastest rates of flow development. The LHF approximation was effective for estimating liquid volume fraction distributions for atomization breakup and $\overline{\alpha_f} > 0.2$, however, the predictions gave no warning of vastly reduced mixing rates as the wind-induced breakup regime was entered and was generally unsatisfactory in dilute portions of the flow ($\overline{\alpha_f} < 0.2$) where it overestimated the rate of development of the flow. Thus predictions of entrainment rates were generally unsatisfactory since entrainment is dominated by processes in dilute portions of the spray. These results suggest that separated-flow phenomena are important for most practical sprays.

The current phase of the investigation is examining the effect of gas density on the effectiveness of the LHF approximation and is studying separated flow phenomena in dense sprays at atmospheric pressure. An apparatus for testing dense sprays at elevated ambient pressures has been designed and is currently being assembled. This arrangement involves observation of sprays within a pressure vessel (1.5 m in diameter and 4.5 m high) at pressures up to 1 MPa. Measurements with this arrangement will include flow visualization, using flash photography, and liquid volume fraction distributions, using gamma-ray absorption. The measurements will be used to evaluate predictions based on the LHF approximation similar to the first phase of the study.

The study of separated-flow phenomena is using the same apparatus as the first phase of the study. New measurements include double-flash holography, to provide liquid element shapes, sizes and velocities; and phase-discriminating LDA to provide mean and fluctuating velocities of the gas phase. A high resolution holocamera and reconstruction system has been developed which has been able to penetrate the dense spray to the surface of the contiguous liquid core. The drop-containing mixing layer around the contiguous liquid core has large concentrations of irregular liquid elements (ligaments, oblong drops, etc.) up to about half the distance from the liquid core to the edge of the flow with relatively small spherical drops near the edge of the flow. Liquid volume fractions are relatively small throughout the gas-containing portion of the flow; thus dense sprays have large liquid fractions due to the presence of many large liquid elements and are primarily characterized by the presence of irregular liquid elements in addition to drops. The size of liquid elements and drops progressively decreases with increasing distance from the contiguous liquid core. Coupled with the low liquid volume fraction, this implies that breakup and turbulent dispersion of particles dominate processes in the drop-containing mixing layer — not processes of drop collisions and modifications of interphase transport rates by neighboring drops which have been proposed in the past. Drop velocities increase significantly with increasing drop size since large drops relax slowly to the local gas velocity. This observation provides unequivocal evidence for the importance of separated-flow effects in dense sprays. Thus, the success of the LHF approximation at high liquid fractions is largely caused by the fact that velocity defect of the gas and small drops is irrelevant, since their total momentum is small, in spite of the fact that they have significantly different velocities from the bulk of the liquid.

Current work is concentrating on completing assembly of the elevated pressure apparatus and initiating tests with this facility; and continuing measurements using the holocamera system for atmospheric pressure sprays. Subsequent work will involve analysis based on the LHF approximation of sprays in dense environments and measurements of gas-phase properties of atmospheric pressure sprays using the phase-discriminating LDA. It is anticipated that this work will be completed during the next report period.

4. SUMMARY OF INVESTIGATION

4.1 Articles and Papers

Bulzan, D. L., Shuen, J.-S. & Faeth, G. M. (1987) Particle-laden swirling free jets: measurements and predictions. AIAA Paper No. 87-0303.

Bulzan, D. L., Shuen, J.-S. & Faeth, G. M. (1988) Particle-laden weakly swirling free jets: measurements and predictions. AIAA Paper No. 88-3138.

Bulzan, D. L., Shuen, J.-S. & Faeth, G. M. (1988) Particle-laden weakly swirling free jets: measurements and predictions. Proceedings of the 1988 Spring Technical Meeting, Central States Section of the Combustion Institute, Pittsburgh, pp. 21-26.

Faeth, G. M. (1987) Mixing, transport and combustion in sprays. Prog. Energy. Combust. Sci. 13, 293-345.

Faeth, G. M. (1987) Structure of nonpremixed and premixed combusting pressure-atomized sprays. Proceedings of the Twentieth Fall Technical Meeting, Eastern Section of the Combustion Institute, Pittsburgh, pp. B.1-B.10.

Faeth, G. M. (1987) Turbulent multiphase flows. Proceedings of the U.S.-France Workshop on Turbulent Reactive Flows (S.N.B. Murthy and R. Borghi, eds.), Springer-Verlag, Berlin, in press.

Parthasarathy, R. N. & Faeth, G. M. (1987) Structure of particle-laden turbulent water jets in still water. Int. J. Multiphase Flow 13, 699-716.

Parthasarathy, R. N. & Faeth, G. M. (1987) Structure of turbulent particle-laden jets having comparable phase densities. Proceedings of the 1987 Spring Technical Meeting, Central States Section of the Combustion Institute, Pittsburgh, pp. 464-469.

Parthasarathy, R. N. & Faeth, G. M. (1988) Homogeneous turbulence in dilute particle-laden flows. 41st Annual Meeting: American Physical Society Division of Fluid Dynamics, Buffalo.

Ruff, G. A. Sagar, A. D. & Faeth, G. M. (1987) Structure of large-scale pressure-atomized sprays. First Annual Conference of ILASS-Americas, Madison, WI.

Ruff, G. A. Sagar, A. D. & Faeth, G. M. (1987) Structure and mixing properties of pressure-atomized sprays. AIAA Paper No. 88-0237; also AIAA J., in press.

Ruff, G. A. Bernal, L. P.. & Faeth, G. M. (1988) Structure of near-injector region of nonevaporating pressure-atomized sprays. AIAA 27th Aerospace Sciences Meeting, Reno.

4.2 Participants

G. M. Faeth, Principal Investigator; Professor, The University of Michigan.

R. N. Parthasarathy, Graduate Assistant, Doctoral Candidate, The University of Michigan.

G. A. Ruff, Graduate Assistant, Doctoral Candidate, The University of Michigan.

4.3 Oral Presentations

G. M. Faeth, "Turbulence/Drop Interactions in Sprays," Southwest Mechanics Seminar Series: Southwest Research Institute, San Antonio; University of Houston, Houston; and Shell Development Company, Houston, October 1986.

G. M. Faeth, "Turbulence/Particle Interactions in Dilute Particle-Laden Liquid Jets," Department of Mechanical Engineering, Carnegie-Mellon University, Pittsburgh, February 1987.

G. M. Faeth, "Particle-Laden Jets having Comparable Phase Densities," Chemical and Physical Sciences Laboratory Seminar Series, Ford Scientific Research Laboratories, Dearborn, MI, March 1987.

G. M. Faeth, "Turbulent Multiphase Flows," U.S.-France Workshop on Turbulent Reactive Flows, University of Rouen, France, July 1987

G. M. Faeth, "Structure of Nonpremixed and Premixed Combusting Pressure-Atomized Sprays," Fall Technical Meeting, Eastern Section of the Combustion Institute, Gaithersburg, MD, November 1987.

G. M. Faeth, "Structure and Mixing Properties of Pressure-Atomized Sprays," AIAA 26th Aerospace Sciences Meeting, Reno, NV, January 1988.

G. M. Faeth, "Dense Spray Structure and Phenomena," AFOSR Contractors' Meeting on Combustion, Pasadena, CA, June 1988.

G. M. Faeth, "Structure of Pressure-Atomized Sprays," Propulsion Seminar Series, University of Alabama, Huntsville, AL, September 1988.

R. N. Parthasarathy, "Structure of Turbulent Particle-Laden Jets having Comparable Phase Densities," Spring Technical Meeting, Central States Section of the Combustion Institute, Argonne, IL, May 1987.

R. N. Parthasarathy, "Structure of Turbulent Particle-Laden Water Jets in Still Water," Seminar, Department of Aerospace Engineering, The University of Michigan, Ann Arbor, MI, March 1987.

R. N. Parthasarathy, "Turbulence Properties in Homogeneous Particle-Laden Flows," Seminar, Department of Aerospace Engineering, The University of Michigan, Ann Arbor, MI, April 1988.

G. Ruff, "Structure of Large-Scale Pressure-Atomized Sprays," First Annual Conference of ILASS-Americas, Madison, WI, May 1987.

G. Ruff, "Structure of the Dense-Spray Region of pressure-atomized Sprays," Seminar, Department of Aerospace Engineering, The University of Michigan, Ann Arbor, MI, November 1987.

REFERENCES

Adrian, R. J. & Yao, C. S. (1987) Power spectra of fluid velocities measured by laser Doppler velocimetry. Expts. in Fluids 5, 17-28.

Al Taweel, A. M. & Landau, J. (1977) Turbulence modulation in two-phase jets. Int. J. Multiphase Flow 3, 341-351.

Batchelor, G. K. (1972) Sedimentation in a dilute dispersion of spheres. J. Fluid Mech. 52, 245-268.

Bilger, R. W. (1976) Turbulent jet diffusion flames. Prog. Energy Combust. Sci. 1, 87-109.

Box, G.E.P. & Jenkins, G. M. (1976) Time Series Analysis, Revised Edition, Holden-Day, San Francisco, 47-84.

Bracco, F. V. (1983) Structure of high-speed full-cone sprays. Recent Advances in Gas Dynamics (C. Casci, ed.), Plenum Publishing Corporation, New York

Chehroudi, B., Onuma, Y., Chen, S.-H. & Bracco, F. V. (1985) On the intact core of full-cone sprays. SAE Paper 850126.

Clift, R., Grace, J. R. & Weber, M. E. (1978) Bubbles, Drops and Particles. Academic Press, New York, 266-269; 296-302.

Faeth, G. M. (1977) Current status of droplet and liquid combustion. Prog. Energy Combust. Sci. 3, 191-224.

Faeth, G. M. (1983) The evaporation and combustion of sprays. Prog. Energy Combust. Sci. 9, 1-76.

Faeth, G. M. (1987) Mixing, transport and combustion in sprays. Prog. Energy Combust. Sci. 13, 293-345.

Gomi, H. & Hasegawa, K.-I. (1984) Measurements of the liquid phase mass in gas-liquid sprays by X-ray attenuation. Int. J. Multiphase Flow 10, 653-662.

Hinze, J. O. (1972) Turbulent fluid and particle interaction. Progress in Heat and Mass Transfer, Vol. 6, Pergamon Press, Oxford, 433-452.

Hiroyasu, H., Shimizu, M. & Arai, M. (1982) The breakup of a high speed jet in a high pressure gaseous atmosphere. Proceedings of the 2nd International Conference on Liquid Atomization and Spray Systems, Madison, Wisconsin.

Humphreys, W. J. (1964) Physics of the Air, Dover Publications, Inc., New York, 279-281.

Jeng, S.-M. & Faeth, G. M. (1984) Species concentrations and turbulence properties in buoyant methane diffusion flames. J. Heat Transfer 106, 721-727.

Kounalakis, M. E., Gore, J. P. & Faeth, G. M. (1988) Turbulence/radiation interactions in non-premixed hydrogen/air flames. Twenty-Second Symposium (International) on Combustion, The Combustion Institute, Pittsburgh, in press.

Kounalakis, M. E., Gore, J. P. & Faeth, G. M. (1988a) Mean and fluctuating radiation properties of turbulent nonpremixed carbon monoxide/air flames. J. Heat Transfer, submitted.

Kraichnan, R. K. (1970) Diffusion by a random velocity field. Phys. Fluids 13, 22-31.

Lance, M., Marie, J. L.. Charnay, G. & Bataille, J. (1980) Turbulence structure of a co-current air-water bubbly flow. NUREG/CP-0014, Vol. 2, Nuclear Regulatory Commission, Washington, 1363-1383.

Lance, M. & Bataille, J. (1982) Turbulence in the liquid phases of a bubbly air-water flow. Advances in Two-Phase Flow and Heat Transfer (S. Kakac and M. Ishii, ed.), Vol 1, Martinus Nijhof Publishers, The Hague, 403-427.

Lance, M., Marie, J. L., & Bataille, J. (1985) Homogeneous turbulence in bubbly flows. Publication FED-29, ASME, New York, 117-124.

Lockwood, F. C. & Naguib, A.S. (1975) The prediction of fluctuations in the properties of free, round-jet turbulent diffusion flames. Comb. Flame 24, 109-124.

Lopes, J. C. & Dukler, A. E. (1986) Droplet dynamics in vertical gas-liquid flow. A.I.Ch.E. J., submitted.

Mao, C.-P., Szekely, G. A., Jr. & Faeth, G. M. (1980) Evaluation of a locally homogeneous flow model of spray combustion. J. Energy 4, 78-87.

Mao, C.-P., Wakamatsu, Y. & Faeth, G. M. (1981) A simplified model of high pressure spray combustion. Eighteenth Symposium (International) on Combustion, The Combustion Institute, Pittsburgh, 337-347.

Miesse, C. C. (1955) Correlation of experimental data on disintegration of liquid jets. Ind. Engr. Chem. 470, 1690-1697.

Modarress, D., Tan, H. & Elghobashi, S. (1984) Two-component LDA measurements in a two-phase turbulent jet. AIAA J. 22, 624-630.

Odar, F. & Hamilton, W. S. (1964) Force on a sphere accelerating in a viscous fluid. J. Fluid Mech. 18, 302-314.

Ohba, K. (1979) Relationships between radiation transmissivity and void fraction in two-phase/dispersed flow. Technical Report 29, Osaka University, 245-254.

Parthasarathy, R. N., Sagar, A. D. & Faeth, G. M. (1986) Dense-spray structure and phenomena. Annual Report for Grant No. AFOSR-85-0244, Department of Aerospace Engineering, The University of Michigan, Ann Arbor.

Parthasarathy, R. N.& Faeth, G. M. (1987) Structure of particle-laden turbulent water jets in still water. Int. J. Multiphase Flow 13, 699-716.

Parthasarathy, R. N.& Faeth, G. M. (1987a) Structure of turbulent particle-laden jets having comparable phase densities. Proceedings of the 1987 Spring Technical Meeting, Central States Section of the Combustion Institute, Pittsburgh, 464-469.

Parthasarathy, R. N.& Faeth, G. M. (1987b) Dense-spray structure and phenomena: Part I - Turbulence/dispersed-phase interactions. Annual Report for Grant No. AFOSR-85-0244, Department of Aerospace Engineering, The University of Michigan, Ann Arbor.

Parthasarathy, R. N. & Faeth, G. M. (1988) Homogeneous turbulence in dilute particle-laden flows. 41st Annual Meeting: American Physical Society Division of Fluid Dynamics, Buffalo.

Phinney, R. E. (1973) The breakup of a turbulent liquid jet in a gaseous atmosphere. J. Fluid Mech. 63, 689-701.

Ranz, W. E. (1958) Some experiments on orifice sprays. Can. J. Chem. Engr. 36, 175-181.

Reitz, R. D. (1978) Atomization and other breakup regimes of a liquid jet. Ph.D. Dissertation No. 1375-T, Princeton University.

Reitz, R. D. & Bracco, F. V. (1982) Mechanism of atomization of a liquid jet. Phys. Fluids 25, 1730-1742.

Reitz, R. D. & Bracco, F. V. (1984) Mechanisms of breakup of round liquid jets. Encyclopedia of Fluid Mechanics (N. P. Cheremisinoff, ed.), Vol. III, Chap. 11.

Reitz, R. D. & Diwakar, R. (1987) Structure of high-pressure fuel sprays. SAE Paper No. 870598.

Rice, S. O. (1954) Mathematical analysis of random noise. Noise and Stochastic Processes (N. Wax, ed.), Dover Publications Inc., New York, 133-294.

Ruff, G. A. & Faeth, G. M. (1987) Dense-spray structure and phenomena: Part II - Pressure-atomized sprays. Interim Report for Grant No. AFOSR-85-0244, Department of Aerospace Engineering, The University of Michigan, Ann Arbor.

Ruff, G. A., Sagar, A. D. & Faeth, G. M. (1987) Structure of large-scale pressure-atomized sprays. First Annual Conference of ILASS-Americas, Madison.

Ruff, G. A., Sagar, A. D. & Faeth, G. M. (1988) Structure and mixing properties of pressure-atomized sprays. AIAA Paper No. 88-0237; also AIAA J., in press.

Santoro, R. J., Semerjian, J. H., Emmerman, P. J. & Goulard, R. (1981) Optical tomography for flow field diagnostics. Int. J. Heat Mass Trans. 24, 1139-1150.

Schlichting, H. (1979) Boundary Layer Theory, seventh edition, McGraw-Hill, New York, 234-235; 599.

Schrock, V. E. (1969) Two-Phase Flow Instrumentation. ASME, New York, 24-35.

Serizawa, A., Kataoka, I. & Mishigoshi, I. (1975) Turbulence structure of air-water bubbly flow. Int. J. Multiphase Flow 2, 221-225.

Shearer, A. J., Tamura, H. & Faeth, G. M. (1979) Evaluation of a locally homogeneous flow model of spray evaporation. J. Energy 3, 271-278.

Shuen, J.-S., Chen, L.-D. & Faeth, G. M. (1983) Evaluation of a stochastic model of particle dispersion in a turbulent round jet. A.I.Ch.E. J. 29, 167-170.

Shuen, J.-S., Chen, L.-D. & Faeth, G. M. (1983a) Predictions of the structure of turbulent, particle-laden, round jets. AIAA J. 21, 1480-1483.

Shuen, J.-S., Solomon, A.S.P., Zhang, Q.-F. & Faeth, G. M. (1985) Structure of particle-laden jets: Measurements and predictions. AIAA J. 23, 396-404.

Shuen, J.-S., Solomon, A.S.P.& Faeth, G. M. (1986) Drop-turbulence interactions in a diffusion flame. AIAA J. 24, 101-108.

Smith, R. H. & Wang, C.-T. (1944) Contracting cones giving uniform throat speeds. J. Aero. Sci. 11, 356-360.

Solomon, A.S.P., Shuen, J.-S., Zhang, Q.-F. & Faeth, G. M. (1985) Structure of nonevaporating sprays: I. Near-injector conditions and mean properties. AIAA J. 23, 1548-1555. *Ibid.* II. Drop and turbulence properties. AIAA J. 23, 1724-1730.

Solomon, A.S.P., Shuen, J.-S., Zhang, Q.-F. & Faeth, G. M. (1985a) Measurements and predictions of the structure of evaporating sprays. J. Heat Transfer 107, 679-686.

Solomon, A.S.P., Shuen, J.-S., Zhang, Q.-F. & Faeth, G. M. (1985b) Measurements and predictions of the structure of evaporating sprays. J. of Heat Transfer 107, 679-686.

Sun, T.-Y. & Faeth, G. M. (1986) Structure of turbulent bubbly jets. -- I. Methods and centerline properties. Int. J. Multiphase Flow 12, 99-114.

Sun, T.-Y. & Faeth, G. M. (1986a) Structure of turbulent bubbly jets. -- II. Phase property profiles. Int. J. Multiphase Flow 12, 115-124.

Sun, T. Y., Parthasarathy, R. N. & Faeth, G. M. (1986) Structure of bubbly round condensing jets. J. of Heat Transfer, 108, 951-959.

Tennekes, H. & Lumley, J. L. (1972) A First Course in Turbulence, The MIT Press, Cambridge, 113-124.

Uberoi, M. S. & Freymuth, P. (1970) Turbulent energy balance and spectra of the axisymmetric wake. Phys. Fluids 13, 2205-2210.

Wu, K.-J., Su, C.-C., Steinberger, R. L., Santavicca, D. A. & Bracco, F. V. (1983) Measurements of the spray angle of atomizing jets. J. Fluids Engr. 105, 406-415.

Wu, K.-J., Coghe, A., Santavicca, D. A. & Bracco, F. V. (1984) LDV measurements of drop velocity in diesel-type sprays. AIAA J. 22, 1263-1270.